TU Delft

Delft University of Technology

Document Version
Final published version

Citation (APA)
Waas, C. (2026). *The Tin-Vacancy Center in Diamond as a Quantum Network Node*. [Dissertation (TU Delft), Delft University of Technology]. https://doi.org/10.4233/uuid:612309cf-e7e0-416b-a8aa-a04f8b0be0b7

Important note
To cite this publication, please use the final published version (if applicable).
Please check the document version above.

Copyright
In case the licence states “Dutch Copyright Act (Article 25fa)”, this publication was made available Green Open Access via the TU Delft Institutional Repository pursuant to Dutch Copyright Act (Article 25fa, the Taverne amendment). This provision does not affect copyright ownership.
Unless copyright is transferred by contract or statute, it remains with the copyright holder.

Sharing and reuse
Other than for strictly personal use, it is not permitted to download, forward or distribute the text or part of it, without the consent of the author(s) and/or copyright holder(s), unless the work is under an open content license such as Creative Commons.

Takedown policy
Please contact us and provide details if you believe this document breaches copyrights.
We will remove access to the work immediately and investigate your claim.

*This work is downloaded from Delft University of Technology.*

# The Tin-Vacancy Center in Diamond as a Quantum Network Node

Christopher Waas

# THE TIN-VACANCY CENTER IN DIAMOND AS A QUANTUM NETWORK NODE

## Dissertation

for the purpose of obtaining the degree of doctor
at Delft University of Technology,
by the authority of the Rector Magnificus, Prof.dr.ir. H. Bijl,
chair of the Board for Doctorates,
to be defended publicly on
Monday, March 2nd 2026 at 10:00

by

**Christopher WAAS**

This dissertation has been approved by the promotors.

Composition of the doctoral committee:

| | |
|---|---|
| Rector Magnificus | chairperson |
| Prof.dr.ir. R. Hanson | Delft University of Technology, promotor |
| Dr.ir. T.H. Taminiau | Delft University of Technology, copromotor |
| | |
| *Independent members:* | |
| Prof.dr. S.D.C. Wehner | Delft University of Technology |
| Dr. F. Leal Machado | Delft University of Technology |
| Prof.dr. D. Lucas | University of Oxford, United Kingdom |
| Prof.dr.rer.nat.habil. A.A. Reiserer | Technical University of Munich, Germany |
| Prof.dr.ir. T. van der Sar | Delft University of Technology, reserve member |

Copyright © 2025 Christopher Waas

Cover design: Christopher Waas, Adobe Firefly

ISBN 978-94-6518-253-7

Printed by: Proefschriftspecialist.nl

An electronic version of this dissertation is available at
`http://repository.tudelft.nl/`.

# CONTENTS

**Summary** v

**Samenvatting** vii

**Zusammenfassung** ix

**1 Introduction** 1
References . . . 4

**2 Methods** 7
2.1 The tin-vacancy center in diamond . . . 8
2.1.1 Electronic Structure . . . 8
2.1.2 Optical properties . . . 11
2.1.3 Qubit initialization and readout . . . 13
2.1.4 Spin coherence and qubit control . . . 13
2.2 Tin-vacancy center devices . . . 14
2.3 Setup . . . 15
2.4 Two-photon quantum interference of tin-vacancy centers . . . 19
2.4.1 Time-resolved two-photon quantum interference . . . 19
2.4.2 Model for imperfect visibility . . . 20
2.5 The Barrett-Kok Protocol . . . 22
References . . . 24

**3 Control of solid-state nuclear spin qubits using an electron spin-1/2** 27
3.1 Introduction . . . 28
3.2 Electron spin control . . . 29
3.3 Dynamical Decoupling control . . . 31
3.4 Dynamically Decoupled Radio Frequency control . . . 34
3.5 Electron-nuclear entanglement . . . 37
3.6 Comparison control methods . . . 39
3.7 Hyperfine coupling with the excited state . . . 40
3.8 Discussion and outlook . . . 42
3.9 Supplementary information . . . 43
3.9.1 Experimental setup . . . 43
3.9.2 Magnetic field sweep . . . 44
3.9.3 Electron coherence . . . 45
3.9.4 Magnetic field strength changes . . . 47
3.9.5 Simulations . . . 48
3.9.6 Bell state . . . 49
3.9.7 DDRF using UDD . . . 51

3.9.8 Nuclear spin NMR and Rabi . . . 52
3.9.9 Hyperfine coupling excited state . . . 52
References . . . 54

**4 Two-photon Quantum Interference 59**
4.1 Generation of single photons . . . 60
4.1.1 Setup. . . . 60
4.1.2 Measurements . . . 61
4.2 Off-resonant and double excitation . . . 62
4.3 Cross-polarization in nanophotonic devices . . . 64
4.4 Matchmaking . . . 65
4.5 Two-photon Quantum Interference . . . 67
4.5.1 TPQI with shared pulse . . . 67
4.5.2 TPQI with frequency shifting. . . . 69
4.5.3 TPQI with magnetic field tuning . . . 71
4.5.4 Discussion of TPQI. . . . 72
References . . . 74

**5 Heralded Entanglement Generation between Tin-Vacancy Centers in Diamond Waveguides 77**
5.1 Step-by-step derivation of the Barrett-Kok model including errors . . . 78
5.1.1 Qubit initialization and preparation of superposition . . . 79
5.1.2 Early timebin - Optical pulse. . . . 79
5.1.3 Early timebin - Photon Interference . . . 80
5.1.4 Early timebin - heralding. . . . 81
5.1.5 Time bin pulse on the qubits. . . . 82
5.1.6 Late timebin and total result . . . 82
5.1.7 Evaluation of the protocol . . . 83
5.2 Spin-Photon Correlations . . . 84
5.3 Heralded Entanglement of two tin-vacancy centers . . . 85
5.4 Discussion . . . 88
References . . . 90

**6 Conclusion and Outlook 91**
6.1 Conclusion . . . 91
6.2 Advancing Quantum Networks with the Tin-Vacancy Center . . . 92
6.2.1 Near-term improvements . . . 92
6.2.2 Future improvements . . . 94
6.3 Epilogue . . . 96
References . . . 97

**Acknowledgments 99**

**List of Publications 105**

**Curriculum Vitea 107**

# SUMMARY

Quantum technologies have the potential to revolutionize the way we interact with nature and with one another. In the realm of quantum communication, the goal is to enable provably safe communication between remote parties, enhance quantum sensors, and give access to distributed quantum computation. All these applications require the distribution of high-quality entanglement over long distances in a network. The generation of entangled links poses a major challenge in the current development of quantum networks and has spurred research into various platforms aimed at mitigating the challenges of scaling this technology.

In this thesis, we build and characterize a quantum network node based on the tin-vacancy center in diamond. Its electronic spin fulfills the function of a stationary qubit, which can be addressed optically. We explore its electronic and optical properties through measurements in the various chapters of this thesis, assessing the suitability of the tin-vacancy center for tasks required of a quantum network node. We provide an overview of the theoretical model describing the properties of the tin-vacancy center and the control over it in Chapter 2.

Next to the optically addressable qubit used for communication in a quantum network, long-lived memory qubits are essential building blocks to store entanglement or process quantum information. Diamond naturally hosts a candidate for such memory qubits in the form of surrounding $^{13}$C nuclear spins. We investigate the control of these memory qubits with the tin-vacancy center mediated by the hyperfine coupling using different control methods in Chapter 3. We show the generation of an entangled state between the tin-vacancy center and a $^{13}$C qubit and discuss challenges and opportunities for future use of this system.

Generating remote entangled links between tin-vacancy centers requires information transfer via optical photons. The quality of an entangled link is limited by the visibility of these photons when they interfere with each other. In Chapter 4, we measure the visibility of photons emitted by tin-vacancy centers in a two-photon quantum interference experiment. We probe multiple pairs of tin-vacancy centers in different configurations and observe visibilities comparable to those of other solid-state quantum network platforms.

Having studied the control over the spin functioning as a qubit as well as the optical interface of the tin-vacancy center, we combine both in Chapter 5 to create spin-photon and ultimately heralded spin-spin entangled states. We introduce an analytical error model that captures the relevant error sources to predict achievable entanglement rates and fidelities. We prepare spin-photon correlated states on two tin-vacancy centers, respectively, and use them as a resource to entangle the two spins. With these experiments, we demonstrate all relevant capabilities that are required for using the tin=vacancy center as a quantum network node.

# SAMENVATTING

Kwantumtechnologieën hebben de potentie om onze interactie met de natuur en met elkaar te revolutioneren. Op het gebied van quantumcommunicatie is het doel om aantoonbaar veilige communicatie tussen partijen op afstand mogelijk te maken, kwantum sensoren te verbeteren en gedistribueerde kwantumcomputers te faciliteren. Deze toepassingen vereisen de distributie van hoogwaardige verstrengeling over lange afstanden in een netwerk. Het genereren van verstrengelde verbindingen vormt een grote uitdaging in de huidige ontwikkeling van kwantumnetwerken en heeft geleid tot onderzoek naar verschillende platformen die de moeilijkheid van het opschalen van deze technologie willen verminderen.

In dit proefschrift bouwen en karakteriseren we een kwantumnetwerkknooppunt op basis van het tin-holtecentrum in diamant. De elektronische spin van dit tin-holtecentrum vervult de functie van een stationaire qubit, die optisch kan worden aangestuurd. We onderzoeken de elektronische en optische eigenschappen ervan door middel van metingen in de verschillende hoofdstukken van dit proefschrift, waarbij we onderzoek doen naar de geschiktheid van het tin-holtecentrum voor verschillende essentiele taken voor een kwantumnetwerkknooppunt. In hoofdstuk 2 geven we een overzicht van het theoretische model dat de eigenschappen van het tin-holtecentrum en de controle daarover beschrijft.

Naast de optisch adresseerbare qubit die wordt gebruikt voor communicatie in een kwantumnetwerk, zijn langlevende geheugenqubits essentiële bouwstenen voor het opslaan van verstrengeling of het verwerken van kwantuminformatie. Diamant bevat van nature een kandidaat voor dergelijke geheugenqubits in de vorm van $^{13}$C kernspins. In hoofdstuk 3 onderzoeken we de besturing van deze geheugenqubits met het tin-holtecentrum, gemedieerd door de hyperfijne koppeling, met behulp van verschillende besturingsmethoden. We tonen de generatie van een verstrengelde toestand tussen het tin-holtecentrum en een $^{13}$C qubit en bespreken de uitdagingen en mogelijkheden voor toekomstig gebruik van dit systeem.

Het genereren van verstrengelde verbindingen op afstand tussen tin-holtecentra vereist informatieoverdracht via optische fotonen. De kwaliteit van een verstrengelde verbinding wordt beperkt door de zichtbaarheid van deze fotonen wanneer ze met elkaar interfereren. In hoofdstuk 4 meten we de zichtbaarheid van fotonen die worden uitgezonden door tin-holtecentra in een twee-foton kwantuminterferentie-experiment. We onderzoeken meerdere paren tin-holtecentra in verschillende configuraties en observeren zichtbaarheden die vergelijkbaar zijn met die van andere vaste-stof kwantumnetwerkplatforms.

Na onderzoek gedaan te hebben naar de controle over de spin die functioneert als een qubit en naar de optische interface van het tin-holtecentrum, combineren we beide in hoofdstuk 5 om spin-foton- en uiteindelijk aangekondigde spin-spin-verstrengelde toestanden te creëren. We introduceren een analytisch model dat de relevante bron-

nen van experimentele onjuistheden vastlegt om haalbare verstrengelingssnelheden en fideliteiten te voorspellen. We bereiden spin-foton gecorreleerde toestanden voor op respectievelijk twee tin-holtecentra en gebruiken deze als bronnen om de twee spins te verstrengelen. Met deze experimenten demonstreren we alle relevante capaciteiten die nodig zijn om het tin-holtecentrum te gebruiken als een kwantumnetwerkknooppunt.

# ZUSAMMENFASSUNG

Quantentechnologien haben das Potenzial, die Art und Weise, wie wir mit der Natur und miteinander interagieren, zu revolutionieren. Im Bereich der Quantenkommunikation besteht das Ziel darin, eine nachweislich sichere Kommunikation zwischen entfernten Parteien zu ermöglichen, Quantensensoren zu verbessern und Zugang zu verteilter Quantenberechnung zu gewähren. All diese Anwendungen erfordern die Verteilung von hochwertiger Verschränkung über große Entfernungen in einem Netzwerk. Die Erzeugung verschränkter Verbindungen stellt eine große Herausforderung für die aktuelle Entwicklung von Quantennetzwerken dar und hat die Forschung zu verschiedenen Plattformen veranlasst, die darauf abzielen, die Schwierigkeiten bei der Skalierung dieser Technologie zu verringern.

In dieser Arbeit bauen und charakterisieren wir einen Quantennetzwerkknotenpunkt auf Basis des Zinn-Fehlstellenzentrums in Diamant. Sein elektronischer Spin erfüllt die Funktion eines stationären Qubits, das optisch adressiert werden kann. Wir untersuchen seine elektronischen und optischen Eigenschaften mittels Messungen in den verschiedenen Kapiteln dieser Arbeit und bewerten die Eignung des Zinn-Fehlstellenzentrums für Aufgaben, die von einem Quantennetzwerkknotenpunkt verlangt werden. In Kapitel 2 geben wir einen Überblick über das theoretische Modell, das die Eigenschaften des Zinn-Fehlstellenzentrums sowie dessen Steuerung beschreibt.

Neben dem optisch adressierbaren Qubit, das für die Kommunikation in einem Quantennetzwerk verwendet wird, sind langlebige Speicherqubits wesentliche Bausteine, um Verschränkungen zu speichern oder Quanteninformationen zu verarbeiten. Diamant beherbergt von Natur aus einen Kandidaten für solche Speicherqubits in Form von $^{13}$C-Kernspins. Wir untersuchen die Steuerung dieser Speicherqubits mit dem Zinn-Fehlstellenzentrum, mittels Hyperfeinkopplung, unter Verwendung verschiedener Steuerungsmethoden in Kapitel 3. Wir zeigen die Erzeugung eines verschränkten Zustands zwischen dem Zinn-Fehlstellenzentrum und einem $^{13}$C-Qubit und diskutieren Herausforderungen sowie Möglichkeiten für die zukünftige Nutzung dieses Systems.

Die Erzeugung von entfernten verschränkten Verbindungen zwischen Zinn-Fehlstellenzentren erfordert die Übertragung von Informationen über optische Photonen. Die Qualität einer verschränkten Verbindung wird durch die Sichtbarkeit dieser Photonen begrenzt, wenn sie miteinander interferieren. In Kapitel 4 messen wir die Sichtbarkeit von Photonen, die von Zinn-Fehlstellenzentren in einem Zwei-Photonen-Quanteninterferenzexperiment emittiert werden. Wir untersuchen mehrere Paare von Zinn-Fehlstellenzentren in verschiedenen Konfigurationen und beobachten Sichtbarkeiten, die mit denen anderer Festkörper-Quanten-Netzwerkplattformen vergleichbar sind.

Nachdem wir die Steuerung des als Qubit fungierenden Spins sowie die optische Schnittstelle des Zinn-Fehlstellenzentrums untersucht haben, kombinieren wir beide in Kapitel 5, um Spin-Photon- und letztlich angekündigte Spin-Spin-verschränkte Zustän-

de zu erzeugen. Wir führen ein analytisches Fehlermodell ein, das die relevanten Fehlerquellen erfasst, um erreichbare Verschränkungsraten und -treue vorherzusagen. Wir bereiten Spin-Photon-korrelierte Zustände auf zwei Zinn-Fehlstellenzentren vor und verwenden sie als Ressource, um die beiden Spins zu verschränken. Mit diesen Experimenten demonstrieren wir alle relevanten Fähigkeiten, die für die Nutzung des Zinn-Fehlstellenzentrums als Quantennetzwerkknotenpunkt erforderlich sind.

# 1

# INTRODUCTION

# 1

Throughout the ages, many key milestones in human development were centered around communication. The development of tools like chisels or markers in the stone age allowed humans to document stories and tales in graphical form. Later, Mesopotamian and Egyptian cultures developed abstract symbols to represent words in order to precisely spread information. Alphabets were developed to arbitrarily construct new words and increase the amount of information being expressible. With the spread of literacy and the notation of information, tools for writing like papyrus and paper were developed, and Gutenberg's first printing press in the 15th century facilitated the widespread of written information. In the past 200 years, technologies like telegraphs and telephones started the era of long-distance communications. Broadcasts over radio and television spread information to basically everyone on earth, and even beyond. New technologies like mobile telephones and the internet made communication possible from anywhere to anyone, introducing the sentence "Where are you?" to humans.

It is hard to imagine what the future holds for new communication technologies. *Quantum communication* describes a new form of interconnectivity, harnessing the unique properties of quantum mechanics to make communication provably secure. Like for many new technologies, there are multiple paths explored simultaneously during the development. Quantum key distribution already allows for cryptographically safe communication and has been implemented in real life settings [1,2]. On the other hand, *quantum networks* based on interconnected quantum nodes with the possibility to process quantum information have been the focus of research for the last decades as well [3,4]. This technology, once fully developed, will change the way we communicate yet again - and more. In a quantum network, quantum nodes are interconnected via long-lived entangled states [5]. These entangled states become the resource for a variety of applications, from secure quantum communication via quantum state teleportation [6], over enhanced sensing of signals from the universe [7] to distributed quantum computation [8]. The latter aspect might become a key motivation for rudimentary quantum networks, as building large scale quantum computers might benefit from the possibility to interconnect many smaller scale quantum processors.

Among the candidates for this technology are platforms like trapped ions [9–12], neutral atoms [13,14], and solid-state photon emitters like rare-earth ions [15] and color centers. All these platforms realize the conceptual idea of hosting stationary, long-lived* coherent qubits, often realized by an effective spin, that have an optically addressable interface and can generate qubit-photon entangled states. Routing the photon through the network and combining it with photons from other nodes or directly sending it to other nodes can be leveraged to generated qubit-qubit entanglement.

Diamond has been established as a prominent host for color centers, and has been at the forefront of solid-state emitter research for the past decades. Color centers in diamond are usually formed by an impurity atom replacing a carbon atom of the diamond lattice, combined with a neighboring vacant lattice site. With the nitrogen-vacancy center in diamond, important milestones like heralded remote entanglement [16], deterministic entanglement delivery [17] and the creation of a multi-node quantum network [18] as well as the teleportation of information across it [6] have been achieved.

*"Long" is a relative expression here, for human purposes, the timescales involved are incredibly short, but compared to the communication or computation times, they are long.

While the nitrogen-vacancy center fulfills all requirements for a rudimentary quantum network, its scalability is limited due to its high sensitivity to electric fields, making it practically impossible to integrate it into scalable photonic interfaces like nanophotonic structures or photonic integrated circuits. One of the color centers that promises to solve this challenge is the tin-vacancy center in diamond. It is more resilient to electric fields and can hence be integrated into scalable photonic platforms [19,20]. In this thesis, we build a quantum network node based on the tin-vacancy center in diamond and investigate various properties that are required for its full functionality.

In **Chapter 2**, I explain the theoretical framework of the tin-vacancy center required for understanding this thesis and describe the setup used to control it. In **Chapter 3**, we show control over the electron spin of the tin-vacancy center and nuclear spins in its surrounding. This research is vital for enabling the use of multiple qubits per node and shows important differences to the nitrogen-vacancy center in diamond.

In **Chapter 4**, we demonstrated the creation of indistinguishable single photons from tin-vacancy centers, a crucial component to enable the generation of remote entanglement. With a two-photon quantum interference experiment, the quality of the photons in terms of their indistinguishability is determined.

In **Chapter 5**, we combine the generation of single photons with the control over the electron spin and create spin-photon correlated states. We implement the control on two separate centers and generate heralded entanglement between two tin-vacancy centers.

In **Chapter 6**, I summarize the outcomes of this thesis and give an outlook into near- and mid-term developments for building a quantum network with color centers.

1

# REFERENCES


[1] Y.-A. Chen *et al.*, *An integrated space-to-ground quantum communication network over 4,600 kilometres,* Nature **589**, 214 (2021).

[2] R. C. Berrevoets *et al.*, *Deployed measurement-device independent quantum key distribution and Bell-state measurements coexisting with standard internet data and networking equipment,* Communications Physics **5**, 186 (2022).

[3] H. J. Kimble, *The quantum internet,* Nature **453**, 1023 (2008).

[4] S. Wehner, D. Elkouss and R. Hanson, *Quantum internet: A vision for the road ahead,* Science **362** (2018), 10.1126/science.aam9288.

[5] M. Ruf, N. H. Wan, H. Choi, D. Englund and R. Hanson, *Quantum networks based on color centers in diamond,* Journal of Applied Physics **130**, 070901 (2021).

[6] S. L. N. Hermans *et al.*, *Qubit teleportation between non-neighbouring nodes in a quantum network,* Nature **605**, 663 (2022).

[7] P.-J. Stas *et al.*, *Entanglement Assisted Non-local Optical Interferometry in a Quantum Network,* (2025), arXiv:2509.09464 [quant-ph] .

[8] P. Drmota *et al.*, *Verifiable Blind Quantum Computing with Trapped Ions and Single Photons,* Physical Review Letters **132**, 150604 (2024).

[9] L. J. Stephenson *et al.*, *High-Rate, High-Fidelity Entanglement of Qubits Across an Elementary Quantum Network,* Physical Review Letters **124**, 110501 (2020).

[10] D. P. Nadlinger *et al.*, *Experimental quantum key distribution certified by Bell's theorem,* Nature **607**, 682 (2022).

[11] V. Krutyanskiy *et al.*, *Entanglement of Trapped-Ion Qubits Separated by 230 Meters,* Physical Review Letters **130**, 050803 (2023).

[12] S. Saha *et al.*, *High-fidelity remote entanglement of trapped atoms mediated by time-bin photons,* Nature Communications **16**, 2533 (2025).

[13] S. Ritter *et al.*, *An elementary quantum network of single atoms in optical cavities,* Nature **484**, 195 (2012).

[14] T. van Leent *et al.*, *Entangling single atoms over 33 km telecom fibre,* Nature **607**, 69 (2022).

[15] A. Ruskuc *et al.*, *Multiplexed entanglement of multi-emitter quantum network nodes,* Nature (2025), 10.1038/s41586-024-08537-z.

[16] H. Bernien *et al.*, *Heralded entanglement between solid-state qubits separated by three metres,* Nature **497**, 86 (2013).

[17] P. C. Humphreys *et al.*, *Deterministic delivery of remote entanglement on a quantum network,* Nature **558**, 268 (2018).

[18] M. Pompili *et al.*, *Realization of a multinode quantum network of remote solid-state qubits,* Science **372**, 259 (2021).

[19] A. E. Rugar *et al.*, *Narrow-Linewidth Tin-Vacancy Centers in a Diamond Waveguide,* ACS Photonics **7**, 2356 (2020).

[20] M. Pasini *et al.*, *Nonlinear Quantum Photonics with a Tin-Vacancy Center Coupled to a One-Dimensional Diamond Waveguide,* Physical Review Letters **133**, 023603 (2024).

# 2

# METHODS

*In this chapter, I describe the theoretical and experimental background that is relevant for this thesis. I introduce the tin-vacancy center in diamond and describe the Hamiltonian used to derive the electronic structure, and discuss the optical and spin properties of the tin-vacancy center. I present the setup that was built in the scope of this work to control tin-vacancy centers in diamond. Lastly, I describe the theoretical background for two-photon quantum interference experiments and the Barrett-Kok entanglement protocol.*

## 2.1. THE TIN-VACANCY CENTER IN DIAMOND



The tin-vacancy center (SnV) in diamond is a color defect center, formed by an interstitial tin atom replacing two carbon atoms in the diamond lattice and the remaining vacancy, which takes a split-vacancy form. It is part of the family of group-IV vacancy centers alongside the silicon-, germanium-, and lead-vacancy center (SiV, GeV, PbV). These defects are usually studied in their negatively charged state, as is the case in this thesis. We will use the words "emitter" and "tin-vacancy center" as well as the abbreviation "SnV" to describe the negatively charged state of the tin-vacancy center throughout this thesis.

The impurity atom for all group-IV vacancy centers resides at the interstitial position, schematically shown in Fig. 2.1(a), which leads to similar properties. In their undisturbed state, the group-IV vacancy centers are members of the $D_{3d}$ symmetry group, which includes a point-inversion symmetry at the location of the impurity atom. This symmetry has been predicted by group theory[1], its electronic structure calculated *ab initio*[2], and verified experimentally[3]. Inversion symmetry leads to a vanishing permanent electric dipole moment despite the defect center's negative charge state, thereby reducing sensitivity to electric fields to second order.

As a consequence, group-IV defects can be integrated into nanophotonic structures like waveguides and photonic crystal cavities without losing their optical properties due to the electric field noise of fabrication-induced charge traps[4–6]. For scaling optical defect-center-based quantum technologies, integration into nanophotonic structures and subsequently into integrated photonic circuits is widely regarded as crucial. Hence, the reduced sensitivity to electric fields is a substantial advantage over defect centers without point-inversion symmetry like the nitrogen-vacancy center in diamond, whose susceptibility to charge noise destabilizes its optical transitions in nanophotonic structures.

Out of the group-IV vacancy centers, the silicon-vacancy center has been studied as the first and hence also the most, with remarkable successes including an efficient spin-photon interface in a nanophotonic cavity[7] and a metropolitan-distance entanglement link[8].

The tin-vacancy center was first reported in 2017 in Ref.[9]. Since then, the interest in this color center has grown rapidly, as it promises better properties in some regards than the silicon-, and germanium-vacancy. The heavier impurity atom leads to a larger spin-orbit coupling, which increases the operational temperature (see sec. 2.1.4 for details), potentially enabling operation at 4 K[10]. Additionally, the emission of photons into the zero-phonon line, important for quantum networks, has a higher probability than for the reported group-IV defects (see Sec. 2.1.2). These properties make the tin-vacancy center in diamond a promising candidate for a solid-state quantum network node compatible with integrated photonics.

### 2.1.1. ELECTRONIC STRUCTURE

As illustrated in Fig. 2.1(b), the group-IV vacancy centers are made up of six orbital states hybridized from the dangling carbon bonds with the impurity atomic orbitals[12], each able to host two electrons with opposite spin. The negatively charged centers have

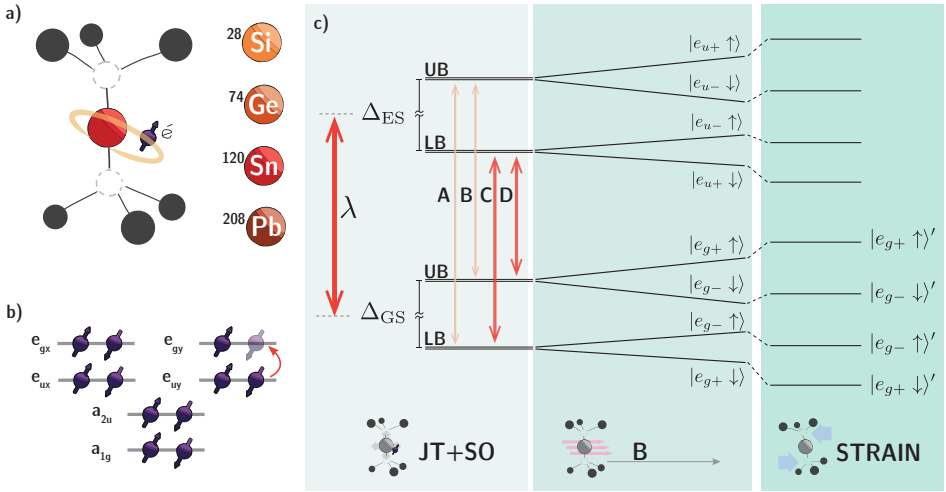


Figure 2.1: **Group-IV vacancy centers in diamond.** (a) Schematic configuration of the defect. An impurity atom replaces two adjacent carbon atoms in the diamond crystal structure by taking an interstitial position to form a group-IV vacancy center. (b) The filling of the electronic levels. The group-IV vacancy centers are made up of six hybridized orbitals from the dangling bonds of surrounding carbon atoms and the impurity atom's orbitals. The surrounding carbon atoms contribute six electrons, the impurity atom four, and an additional electron is captured from the environment. This leaves one electron state empty, effectively creating a spin-1/2 system with this hole. The center can be excited by promoting the electron from the lower energy level to the vacant state in the higher energy level. (c) The electronic level structure of group-IV vacancy centers. The Jahn-Teller effect (JT) and spin-orbit coupling (SO) create a lower (LB) and upper (UB) branch in the ground and excited state. An external magnetic field (B)causes the doublets to split via the Zeeman effect. Additional transversal strain mixes the orbital basis states, leading to further splitting between the branches. Adapted from Pasini [11].

eleven of these twelve electron states filled, leaving one electron hole, which can be treated as an effective spin-1/2.

A series of different physical effects is at play to create the level structure typically observed in experiments. Here, we describe the most relevant ones, whose impact is visualized schematically in Fig. 2.1(c). The Hamiltonian describing the electronic structure of the group-IV vacancy centers is the same in the ground and excited manifolds. The degeneracy between the four states in each manifold is lifted via the Jahn-Teller effect and spin-orbit coupling (SOC) into a double-degenerate lower and upper branch (LB/UB). Upon the introduction of these effects, we transform the basis of the orbital states from $e_x/e_y$ to $e_+/e_-$, in which the spin-orbit interaction Hamiltonian is diagonal [1]. In this basis, the Hamiltonian takes the form

$$\hat{H}_{\mathrm{SOC}} = -\lambda \vec{L}\cdot\vec{S} = -\frac{\lambda}{2}\hat{\sigma}_z^{\mathrm{orbit}}\hat{\sigma}_z^{\mathrm{spin}}, \tag{2.1}$$

where $\lambda$ is the effective strength of the SOC, $\vec{S} = (\hat{S}_x, \hat{S}_y, \hat{S}_z)$ is the spin-1/2 and $\vec{L} = (\hat{L}_x, \hat{L}_y, \hat{L}_z)$ is the orbital angular momentum. From group theoretical calculations, it can be derived that $\hat{L}_x$ and $\hat{L}_y$ vanish in the $|e_\pm\rangle$ basis [1], leaving only a contribution of $\hat{L}_z$. $\sigma_z$ is the Pauli $z$-operator.

The Jahn-Teller effect describes the spontaneous symmetry breaking of spatially degenerate electronic ground states, thereby lifting the degeneracy. There are two forms of Jahn-Teller effect at play. The dynamic Jahn-Teller effect causes an effective reduction of the spin-orbit coupling strength via the Ham reduction factor. It adds an energy splitting along the spin-orbit coupling due to vibronic zero-point energy differences of the originally degenerate states [2], which is already taken into account in our definition of $\lambda$. An additional static Jahn-Teller effect displaces the impurity atom, which has the same effect as external strain. Therefore, we do not treat it separately in our description.

The application of a magnetic field causes a splitting of the electronic states via the Zeeman effect. The effect can be viewed in two parts: its orbital and spin contributions. The orbital Zeeman effect has the form

$$\hat{H}_{\mathrm{B,L}} = \gamma_L \vec{L}\cdot\vec{B} = f\mu_B \hat{L}_z B_z, \tag{2.2}$$

where the orbital gyromagnetic ratio $\gamma_L$ is the Bohr magneton $\mu_B$ reduced by a quenching factor $f$ due to the Jahn-Teller and Steven's effect, $\vec{B}$ is the magnetic field, and $\hat{L}_z$ is the only non-zero angular momentum operator, like for the SOC.

The Zeeman effect for the electron hole spin is*

$$\hat{H}_{\mathrm{B,S}} = \gamma_e \vec{S}\cdot\vec{B}, \tag{2.3}$$

where $\gamma_e = 28.025\,\mathrm{GHz/T}$ is the gyromagnetic ratio of a free electron spin.

Strain in the diamond acts on the orbital part of the electronic wavefunctions [13]. Axial strain, which is strain along the high-symmetry axis of the defect center, only shifts the optical frequency; it is a common shift for all states in the ground and excited states, but with different magnitudes for the two manifolds due to different strain susceptibilities. Transversal strain, orthogonal to the high-symmetry axis, shifts the energy levels within

*We neglect any small anisotropies here.

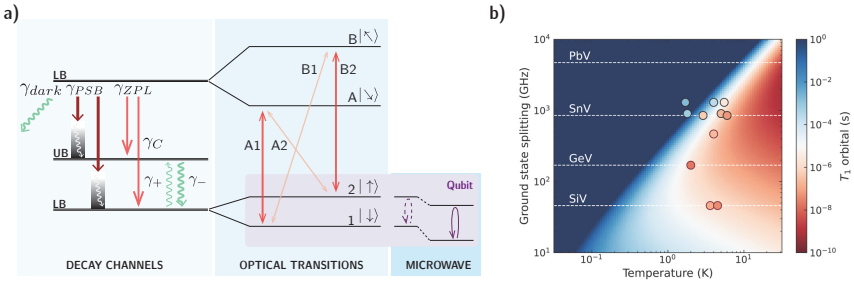


Figure 2.2: **Spin and optical transitions.** (a) Relevant transitions of group-IV defect centers. Phonons can transfer population between the LB and UB of each manifold. Between the manifolds, four distinct optical transitions are relevant for controlling the group-IV color center. The qubit defined in the LB of the ground state manifold cannot be controlled directly with microwaves; only the addition of strain and subsequent mixing of the orbital states enables direct qubit control via MW. (b) Optical decay channels from the excited state to the ground state. The excited state can decay directly via the emission of a single photon (zero-phonon line, ZPL), via emission of a photon and phonons (phonon sideband, PSB), or via non-radiative decay channels. (c) Orbital lifetime of the ground state LB as a function of temperature and ground state splitting. The colormap presents simulated values using $\chi\rho = 4.6 \times 10^{-9}\,\mathrm{GHz}^{-2}$, which was measured in our lab [15]. Experimentally determined lifetimes of the silicon-vacancy (SiV) [16–18], germanium-vacancy (GeV) [19], and tin-vacancy (SnV) [10,20,21] centers are represented via circles. The $T_1^{\mathrm{orbit}}$ is estimated from the $T_1^{\mathrm{spin}}$ and $T_2^{*,\mathrm{spin}}$ values via the spin transition cyclicity. The experimental values can be reduced compared to the simulations as other noise sources can limit the coherence as well. Adapted from Pasini [11].

the manifolds and leads to an increase in the splitting between the LB and UB. Additionally, it mixes the $e_+ / e_-$ states into $e'_+ / e'_-$. This effect is crucial for allowing qubit control via microwaves, which will be discussed in Sec. 2.1.4. The Hamiltonian for transversal strain can be written as

$$\hat{H}_{\mathrm{strain}} = \epsilon \hat{o}_x^{\mathrm{orbit}}, \tag{2.4}$$

where $\epsilon$ is the strength of the transversal strain in a coordinate system that is transformed to only require a single parameter and $\sigma_x$ is the Pauli $x$-operator in that coordinate system [14].

In total, the Hamiltonian describing the ground and excited manifold of the group-IV vacancy centers is the sum of all discussed effects

$$\hat{H} = \hat{H}_{\mathrm{SOC}} + \hat{H}_{\mathrm{B,L}} + \hat{H}_{\mathrm{B,S}} + \hat{H}_{\mathrm{strain}}. \tag{2.5}$$

A crucial value coming out of the diagonalization of this Hamiltonian is the energy splitting between the LB and UB in the manifolds given by

$$\Delta = \sqrt{\lambda^2 + 4\epsilon^2}, \tag{2.6}$$

where $\lambda$ and $\epsilon$ are the respective SOC strength and strain.

### 2.1.2. OPTICAL PROPERTIES

In both the ground and excited state manifold, the LB and UB are coupled via phononic transitions as illustrated in Fig. 2.2(a). At cryogenic temperatures, depending on the exact splitting between the LB and UB, the phonon population at the energy gap between

| Center | $\lambda_{ZPL}$ [nm] | $\tau_{bulk}$ [ns] | $\Delta_{GS}$ [GHz] | $QE \times DW$ |
|---|---|---|---|---|
| SiV | 737[24] | 1.8[25] | 50[1] | $(0.1-0.3)\times 0.7$[25,26] |
| GeV | 602[27] | 6[5] | 170[19] | $0.2\times 0.6$[28] |
| SnV | 619[20] | 4.5-8[29] | 822[30] | $0.8\times 0.57$[9,29] |
| PbV | 550[31] | 4.4[31] | 3870[31] | ? |

Table 2.1: Properties group-IV vacancy centers. Adapted from Refs.[11,32].

the branches is small enough to suppress $\gamma_+$ almost completely. Hence, the relevant subspace for experiments is typically limited to the LB because of fast ($\mathcal{O}$(ps – ns)[16,22] phonon decay rates $\gamma_-$.

At finite magnetic field, the LBs of the group-IV vacancy centers split up in two non-degenerate states, giving rise to four optical transitions. Any small misalignment of the magnetic field compared to the SOC along the symmetry axis of the defect result in slightly tilted spin-quantization axes due the different magnitudes of the SOC in the ground and excited states. In this scenario, which is the case for all experiments in this thesis, the optical transitions can be classified in spin-conserving and spin-flipping. Spin-conserving transitions (A1, B2 in Fig. 2.2(a)) have a high cyclicity and are typically used to read out the spin-state whereas spin-flipping transitions (A2, B1) are used to initialize the spin state as detailed in Sec. 2.1.3.

When the defect center is in the excited state, it will decay spontaneously into the ground state. There are multiple channels along which this decay can happen. The decay can be via a single photon in the zero-phonon line (ZPL), assisted via phonons in the phonon sideband (PSB) or via non-radiative channels. The ZPL consists of two lines consisting of the decay from the excited state LB to the ground state LB or UB. The latter will decay subsequently quickly via phonons. We label it ZPL anyway because of the well-defined energy of the photon compared to the broad spectrum in the PSB. For quantum networking applications, the ZPL going from LB to LB is the most relevant as it is the only transition that entangles the photon with the spin state[†]. The fraction of decays into this channel is hence a relevant figure to assess the quality of a defect center as a good spin-photon interface. It can be written as[23]

$$\zeta = QE * DW * BR, \tag{2.7}$$

where $QE$ is the quantum efficiency describing the fraction of radiative decays, $DW$ is the Debye-Waller factor describing the ratio of ZPL decays to all radiative decays, and $BR$ is the branching ratio, capturing the LB-LB transitions compared to all ZPL transitions.

Table 2.1 shows the optical properties for the different group-IV vacancy centers alongside the wavelength $\lambda_{ZPL}$ of the transition from the excited state LB to the ground state LB with their corresponding exponential decay constant in bulk diamond $\tau_{bulk}$.

[†]Technically, also the transition form LB to UB creates a spin-photon entangled state, however the fast decay of the spin from the ground state UB to LB decoheres the state on timescales too fast to use the entangled state effectively.

### 2.1.3. QUBIT INITIALIZATION AND READOUT

At finite magnetic field, a qubit can be defined using the two states of the LB in the ground state manifold. The qubit can be initialized into $|\uparrow\rangle$ by driving the A1 transition (see Fig. 2.2) until the $|\downarrow\rangle$ state is fully depleted: due to different spin-orbit coupling strengths in the ground and excited state, any small misalignment of the magnetic field with respect to the symmetry axis of the defect causes a slightly different orientation of the spin-quantization axes in both manifolds. Therefore, the decay from the excited state has a non-zero chance to flip the spin state. When driving one of the spin-conserving transitions, an exponential decay of the brightness can be observed due to this probabilistic spin-flipping. The decay constant of this process is called „cyclicity“.

As the Hamiltonian is symmetric upon exchange of $|\uparrow\rangle$ and $|\downarrow\rangle$, the opposite state can be initialized by driving the B2 transition. We do not distinguish between those two cases and label the state into which we initialize as the computational state $|0\rangle$ for the rest of the thesis. Similarly to the initialization, the qubit can be read out by driving the spin-conserving transition connected to $|0\rangle$ for a calibrated duration. Upon detection of a photon emitted by the defect center, we assign the qubit to be in state $|0\rangle$, otherwise in state $|1\rangle$. Here, an optimum readout time has to be calibrated, as the total amount of emitted photons from the emitter is limited by its cyclicity. Once the emitter does not contribute photons anymore, dark-counts of the detectors or stray light distort the readout signal. Hence, we perform a readout calibration to choose the optimum readout time.

To compensate for imperfect readout (e.g. due to limited photon collection, causing an underestimation of the population in $|0\rangle$), we perform a single shot readout correction for many experiments as detailed in Ref. [33], Appendix A.

### 2.1.4. SPIN COHERENCE AND QUBIT CONTROL

The control the initialized qubit is done using microwave (MW) pulses. When on resonance, the magnetic field component of MWs can coherently rotate the spin of the qubit states. However, the qubit states also contain an orbital component, which is not driven by the MW. For unstrained emitters, this forbids direct MW control. Upon the addition of strain to the system, the orbital states mix (see Eq. 2.4), resulting in a non-zero overlap. This allows for direct MW driving with a reduced effective $g$-factor

$$g_{\text{eff}} = 2\frac{\epsilon_{\text{GS}}}{\Delta_{\text{GS}}} g_{\text{electron}}, \tag{2.8}$$

where $\Delta_{\text{GS}}$ is the ground state splitting between the LB and UB defined in Eq. 2.6.

During the experiments the qubit state should remain unchanged without control pulses being played. The relevant timescales for which the qubit is preserved are referred to as $T_1^{\text{spin}}$ for the qubit eigenstates and $T_2^{*,\text{spin}}$ for superposition states. By performing a Hahn-Echo to cancel out quasi-static noise, the coherence of a superposition can be extended to $T_2^{\text{spin, Echo}}$. Applying more control pulses via a method called dynamical decoupling (DD) [34] to repeatedly rephase the qubit, the coherence time can be prolonged even more to $T_2^{\text{spin, DD}}$. In the tin-vacancy center, $T_1^{\text{spin}}$ is typically much longer than $T_2^{\text{spin, DD}}$, which makes the latter the relevant metric for quantum information storage.

Similarly to the qubit, an optical lifetime $T_1^{\text{opt}}$ and $T_2^{*,\text{opt}}$ can be defined.

The decoherence of the qubit and optical transitions is strongly dependent on the temperature of the host diamond as phonons in the crystal can cause transitions between the LB and UB in the ground and excited manifold. The transition rates $\gamma_+$ ($\gamma_-$) from the LB to UB (UB to LB) are given by[35].

$$\gamma_+ = 2\pi\chi\rho\Delta_{\text{GS}}^3 n(\Delta_{\text{GS}}, T), \tag{2.9}$$

$$\gamma_- = 2\pi\chi\rho\Delta_{\text{GS}}^3 [n(\Delta_{\text{GS}}, T) + 1], \tag{2.10}$$

where $\chi$ is the phonon-electron interaction frequency and $\rho$ the phononic densities of state. The Bose-Einstein distribution $n(\Delta_{\text{GS}}, T)$ as a function of temperature $T$ and energy splitting $\Delta_{\text{GS}}$ is given by

$$n(\Delta_{\text{GS}}, T) = \frac{1}{e^{\Delta_{\text{GS}}/k_B T} - 1}, \tag{2.11}$$

where $k_B$ is the Boltzmann constant. The major operating temperature restriction is imposed by requiring $\gamma_+$ to be negligible compared to desirable $T_2$ times of the qubit, as the excitation to the UB of the ground state manifold already causes dephasing of the qubit due to a slightly different $g$-factor. The orbital lifetime of the LB $T_1^{\text{orbit}} = 1/\gamma_+$ hence can be viewed as an upper bound for the spin coherence $T_2$. Due to the strong dependence of $T_1^{\text{orbit}}$ on $\Delta_{\text{GS}}$, a larger ground state splitting is beneficial for higher operating temperatures. Fig. 2.2(c) depicts the orbital lifetime as a function of temperature ground state splitting. The impact of $T_1^{\text{orbit}}$ on $T_1^{\text{spin}}$ is suppressed by the cyclicity of the orbital transitions. At aligned magnetic field, this cyclicity has been measured to $\approx 1200$[10].

For coherence of the optical transitions, $\gamma_+$ should be negligible compared to the optical lifetime of the emitter. In principle, also a phononic transition in the excited state via $\gamma_{+,\text{ES}}$ could dephase the transition, the larger SOC in the excited state and hence larger $\Delta_{\text{ES}}$ diminishes the contribution of this transition. With the parameters in Tab. 2.1, this is the case around 10 K.

For the tin-vacancy center, temperatures below 2 K are required to extend $T_1^{\text{orbit}}$ on the order of a second.

At these temperatures, the coherence of the spin will be limited by other external influences. The most prominent dephasing mechanism in diamond is the coupling to the nuclear spin bath consisting of $^{13}$C atoms, which have a natural abundance of around 1.1 %. Via DD techniques $T_2^{\text{DD}}$ has been extended to 10 ms[30], which is not yet limited by $T_1^{\text{orbit}}$ at the operating temperature of 50 mK. Further improvements in pulse fidelities and less heating from the control pulses combined with higher operating temperatures for experimental ease might create a scenario where the impact of $T_1^{\text{orbit}}$ has to be considered for applications.

## 2.2. TIN-VACANCY CENTER DEVICES

For the purpose of the experiments in this thesis, the tin-vacancy centers are created via high-energy implantation of tin ions into bulk diamond substrates. Other methods like shallow implantation and overgrowth will not be discussed. Extensive details on the fabrication process for our devices can be found in Reference[36].

The tin ions are implanted with an energy of 350 keV under an angle of 7 deg that results in an average depth of around 80 nm below the crystal surface. This step creates substantial damage in the crystal structure, especially along the path of the ions. A subsequent annealing step at 1100 °C under vacuum heals this damage and mobilizes vacancies in the lattice that combine with the tin ions to form tin-vacancy centers. Lastly, a multi-step cleaning procedure including a tri-acid solution is used to remove any remaining graphite or other contamination from the surface. The results in chapter 3 are obtained with a device prepared in this fashion.

For the results in chapters 4 and 5, suspended nanophotonic waveguides have been fabricated after creation of the tin-vacancy centers. The main challenge for the fabrication is the absence of a wet etchant for diamond. A special method called "quasi-isotropic undercut" has been developed in Ref.[37] to undercut diamond devices by utilizing an oxygen-ion plasma etch with zero forward-bias, effectively removing the diamond along its crystallographic axes. By protecting the waveguide structure with a mask before, suspended structures can be created.

To deliver MW control pulses, a bondwire is routed above the diamond in close vicinity without physical contact. This avoids excessive heating of the device during experiments and protects from decoherence of the qubit due to phonons as discussed in Sec. 2.1.4. Lately, on-diamond MW lines made of superconducting materials have shown promising results to a more scalable and deterministic delivery of MW signals[30].

## 2.3. SETUP

The setup to perform experiments with the tin-vacancy center in diamond throughout this thesis is schematically shown in Fig. 2.3. This state configuration of the setup is used for the experiments reported in Chapters 4 and 5. For the confocal measurements in Chapter 3, the setup is detailed in Section 3.9.1.

At the heart of the setup, a cryostat (Bluefors LD250He) cools a diamond with nanophotonic waveguides and SnVs to a base temperature of 450 mK. A *4f*-lens system (not shown) allows for optical imaging. Two tapered optical fibers (Thorlabs S600-HP, taper angle ≈ 3°) on nanopositioning stages (Attocube, ANPx101 and ANPz102) function as interface to the nanophotonic waveguides. While the fibers and waveguides are optimized for in-contact coupling, we use them in a lensed-fiber configuration for experimental ease. The devices and fibers sit in the center of a (3D)-vector magnet (AMI), able to create arbitrarily oriented magnetic fields up to 1 T.

In the following description, we will refer to each of the fibers as a *subsetup*.

In order to address the SnVs optically, two separate lasers are used per subsetup. A green 515 nm laser (Hübner Photonics, Cobolt 06-03-MLD515) is used to initialize the charge environment around the SnV during a charge-resonance check that proceeds most of our measurements[38]. Laser light resonant with the relevant optical transitions of the SnV is provided by an orange 619 nm laser (Toptica Photonics AG, (DL Pro SHG)). Its output light is split into four separate paths, three of which are depicted in Fig. 2.3.

A portion of the laser light passes through two acousto-optic modulators (AOM, Gooch & Housego, Fiber-Q 637nm) used to shape pulses on the order of µs from the

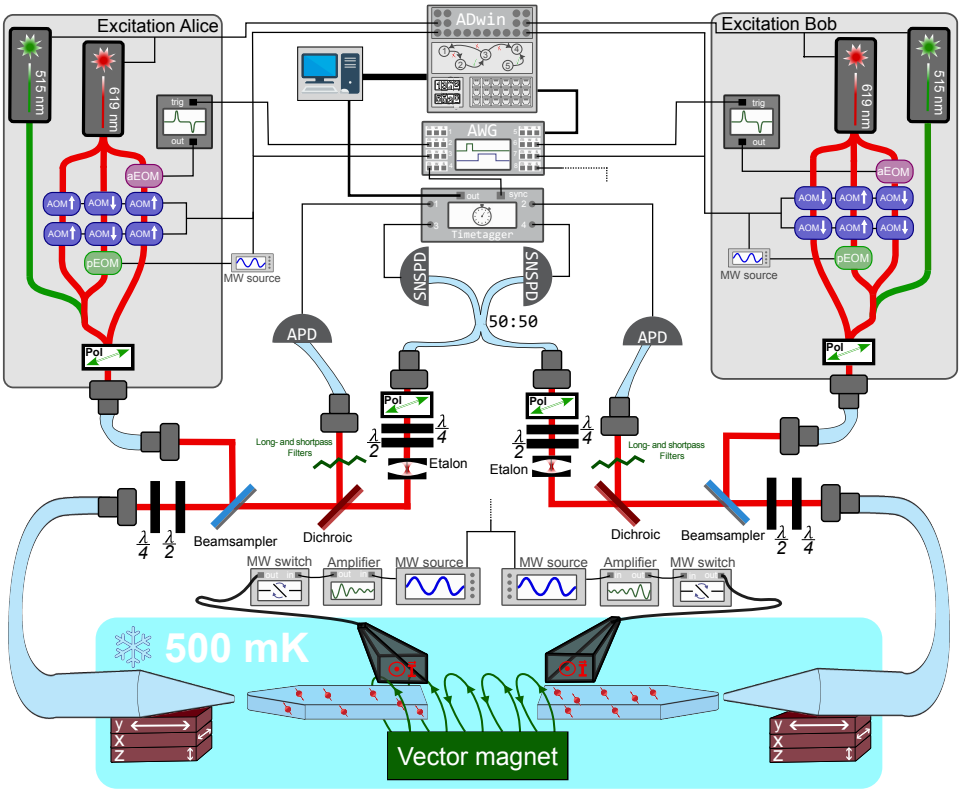


Figure 2.3: **Setup for measurements in this thesis.** A detailed description of all elements is provided in the main text.

continuous-wave laser. A side-effect of these AOMs is a constant 200 MHz frequency shift of the laser light per AOM. The direction of the shift can be chosen by selecting different Bragg modes of the diffraction pattern created by the AOM and is indicated by the arrows. The second path additionally passes a phase electro-optic modulator (pEOM, Jenoptik, PM635) which is driven by a microwave (MW) source (Rohde & Schwarz, SMBV100A). We call these two paths the *readout* and *spinpump* path. The readout path is used to readout the qubit state of the SnV. For this, it needs to be tuned onto resonance with one of the spin-conserving transitions (*A1* or *B2* in Fig. 2.2). To this end, we tune emission frequency of the seed laser.

Before most experimental sequences, we perform a charge-resonance check. At non-zero magnetic field and finite cyclicity of the optical transitions, this sequence requires both spin-conserving transitions to be addressed. As the frequency difference between the two transitions heavily depends on the magnetic field strength, angle as well as the strain environment of the SnV, independent tuning of the laser frequency addressing the second spin-conserving transition is required. This is achieved with the spinpump path. Here, the two AOMs are set up to shift the frequency of the laser light opposite to the readout path, creating a constant 800 MHz frequency difference between the readout and spinpump path. We select the direction of the shifts such that the frequency of the spinpump path is actually tuned *away* from the optical transition it needs to address[‡]. Subsequently, sidebands are modulated onto the laser light with the pEOM. The driving power supplied by the MW source is chosen to maximize the population in the first-order sidebands, and the driving frequency is selected to set one first-order sideband onto resonance with the optical transition it needs to address. The benefit of this approach is that the other sidebands are far detuned from the spin-conserving transitions and should add minimal background noise.

The third optical path functions to create short optical pulses. To this end, we use a combination of acousto- and amplitude electro-optical modulators (AOM/aEOM). While AOMs allow for strong suppression ($\approx 100$ dB in double-pass configuration), their switching times on the scale of 10 ns are not fast enough compared to the lifetime of around 7 ns for SnV centers in nanophotonic waveguides. EOMs have a worse on-off ratio at around 30 dB which is not sufficient to avoid decoherence of the spin via interaction with leakage photons over the course of an entanglement attempt, but their rise-times on the order of 200 ps allow for the generation of short optical pulses. Combined, the AOM suppresses the laser light sufficiently when spin-operations are performed and is only opened briefly before the optical excitation is required which is shaped by the aEOM.

In this work, we use a fiber-coupled aEOM (Jenoptik, AM635). The device relies on constructive (destructive) interference in a Mach-Zehnder interferometer to enable (disable) light transmission. In the idling state, a PID loop monitors the light transmission through the device and minimizes it by applying a voltage to the non-linear optical material in the arms of the interferometer. To generate the optical pulse, a short voltage

[‡]As an example, in the depiction of "Excitation Alice", the readout path addresses the lower frequency transition, and the spinpump path is shifted down compared to the readout path by 800 MHz. If the frequency difference between the optical transitions is e.g. 600 MHz, the spinpump path is now 1.4 GHz detuned from the transition it needs to address.

pulse created by a home-built pulse generator briefly changes the interference condition and enables light transmission. An inverted copy of pulse, played after the AOM is already in its off-state, prevents charging of the EOM and makes the device more stable for long experimental runs. The AOM (Crystal Technologies Inc.) is set up in a free-space double-pass configuration. The total transmission efficiency is around 50 %. We select the constant frequency shift to be the same as for the readout path, such that these two optical paths create laser pulses with the same frequency.

In order to stabilize the laser frequency, a fourth path (not shown) routes laser light to a wavemeter (HighFinesse, WS-8). The frequency reading of the wavemeter is used in a computer-controlled proportional feedback loop that acts on the seed laser. Typical frequency stabilities achieved in this configuration are on the order of 300 kHz, which is sufficient compared to the spectral width of the SnV on the order of 20 MHz.

All laser paths are combined via dichroic mirrors and beamsplitters and routed via the optical fiber into the cryostat and to the SnVs. A set of quarter- and half-waveplates (Thorlabs, WPQ05M-633/WPH05M-633) in motorized rotation mounts (Thorlabs, K10CR1) set the polarization of the laser light. The choice of waveplate settings is discussed in Sec. 4.3.

The light emitted by the SnVs is collected via the same optical fiber and routed outside of the cryostat. A beamsampler (Thorlabs, BSF10-A) marks the separation of the excitation and collection path and transmits at least 90 % of the incident photons. A long-pass filter (Thorlabs, FELH0600) filters reflections of the green laser light to avoid blinding of the single photon detectors. Subsequently, the emitted light is separated into PSB and ZPL via a dichroic mirror (Semrock, FF625-SDi01).

The PSB photons are spectrally filtered further via a tunable long-pass filter (Semrock, TLP-01-628) to remove reflections of the resonant laser light and a short-pass filter at 700 nm (Thorlabs, FESH0700) to filter auto-fluorescence of the optical fiber. The photons are coupled into a multi-mode fiber (Thorlabs, FG050LGA) and routed to an avalanche photon detector (LaserComponents, COUNT-R).

The ZPL photons are filtered by an etalon with a full-width at half maximum of around 40 GHz and a suppression of around −30 dB at 620 nm to remove the remaining photons from decay channel $\gamma_{\mathrm{D}}$ (see Fig. 2.2(a)). Another set of waveplates and a polarizer are used to remove reflected laser light as discussed in Sec. 4.3. The ZPL photons are then coupled into a polarization maintaining fiber connected to a balanced beamsplitter (Evanescent Optics, custom device). This beamsplitter is used for Hong-Ou-Mandel interference in Chap. 4. The two output ports are routed to superconducting nanowire single photon detectors (PhotonSpot, custom device).

The electronic output signal of the photon detectors is recorded by a timetagger (PicoQuant, HydraHarp400) and later retrieved by a measurement computer. Additionally, the signal is routed to a counter module in the microcontroller (description below), enabling real-time processing of photon events required for our charge-resonance checks.

Apart from optical access, the SnVs are addressed by microwave fields in order to control the qubit state coherently. A source (Rohde & Schwarz, SGS100A) generates the

signal, which is amplified (Amplifier Research, 40S1G4 / MiniCircuits, ZHL-50W–52-S+) and routed to the cryostat. To avoid decoherence of the qubit by the noise of the amplifiers, a homebuilt microwave switch disconnects the transmission into the cryostat whenever no signal needs to be supplied. Inside the cryostat, the signal is routed via coaxial cables to a printed circuit board enclosing the diamond. A suspended bondwire, distanced approximately 100 µm above the devices, delivers the signal to the SnVs. The microwave signal is then routed out of the cryostat, attenuated and terminated.

All control signals required to shape the laser and microwave pulses are supplied by a combination of a micro-controller (Jäger Messtechnik, ADwin Pro II) and arbitrary waveform generator (Zurich Instruments, HDAWG). The ADwin performs all laser control sequences required for charge-resonant checks, qubit initialization and readout. We operate the ADwin with a logical clock cycle of 1 µs, suffienct for the mentioned tasks. When required, it triggers the HDAWG which shapes the microwave pulses by modulating the MW sources and the short optical pulse by triggering the pulse generator box. The HDAWG operates with a 2.4 GHz clock rate which allows precise control of the microwave and optical pulses on the sub-ns-scale.

The experiments are prepared in a homebuilt software framework which supplies the required logical sequences to the ADwin and HDAWG and retrieves measured data from the ADwin counters as well as the timetagger. All interfaces to hardware components are established via the quantum measurement infrastructue QMI[39].

## 2.4. TWO-PHOTON QUANTUM INTERFERENCE OF TIN-VACANCY CENTERS

A key requirement for creating entanglement between quantum network nodes via spontaneously emitted photons is their indistinguishability. This metric can be experimentally determined by performing a two-photon quantum interference experiment. In this section, we introduce the theoretical background of this experiment.

### 2.4.1. TIME-RESOLVED TWO-PHOTON QUANTUM INTERFERENCE

The two-photon quantum interference experiment is realized by having two different photons with a temporal shape $\zeta_{1/2}(t)$ impinge on the inputs of a balanced beamsplitter. If these wavefunctions were exactly identical, the Hong-Ou-Mandel effect[40] predicts a vanishing probability to measure a coincidence at the output ports of the beamsplitter. In other words, the photons always leave the beamsplitter through the same port. Deviations between the waveforms lead to a non-zero probability of measuring a coincidence with probability[41]

$$P_{\text{coinc}}(t, t+\Delta t) = \frac{1}{4}|\zeta_1(t)\zeta_2(t+\Delta t) - \zeta_2(t)\zeta_1(t+\Delta t)|^2, \tag{2.12}$$

where $t$ is the detection time of the photon in the first output port of the beamsplitter and $t+\Delta t$ the detection time of the photon in the second output port. As $\Delta t$ can also take negative values, this definition does not assume any order of the photon arrival.

In analogy to classical light interference, a visibility of the interference can be defined by integrating over all possible coincidence events $t$ and $t+\Delta\tau$ as[§]

$$V = 1 - \frac{P_{\text{coinc}}^{\text{indist.}}}{P_{\text{coinc}}^{\text{dist.}}}, \tag{2.13}$$

where the superscripts describe the coincidence probabilities of configurations of the experiment where the photons were prepared to be indistinguishable or distinguishable (e.g. by shifting the temporal profile). The visibility captures the actual indistinguishability of the photons as well as any other noise sources that can lead to coincidences like dark counts or imperfect single-photon emission. The quantity sets a limit to the achievable entanglement fidelity, for the Barrett-Kok protocol[42], this is

$$F \leq \frac{1}{2} + \frac{V}{2}. \tag{2.14}$$

### 2.4.2. MODEL FOR IMPERFECT VISIBILITY

By investigating the photon arrival time difference $\Delta t$-dependence of the visibility, we can gain information on the combined spectral diffusion and pure dephasing of the involved emitters. To this end, we model the photon probability to be composed of two modes: an ideal single photon emitted by the tin-vacancy center $p_{\text{s}}$ and some background noise source $p_{\text{n}}$, e.g. laser photons or photons of other emitters. The probability of a photon arriving from emitter $A$ at the central beamsplitter at time $t$ is hence simply

$$p_{\text{A}}(t) = p_{\text{s}}^{A}(t) + p_{\text{n}}^{A}(t). \tag{2.15}$$

The probability distribution for the single photon can be written as

$$p_{\text{s}}^{A}(t) = N_{\text{A}} e^{-\frac{t}{\tau_{\text{A}}}}\, \Theta(t)\Theta(T_{\text{det}} - t), \tag{2.16}$$

with $N_{\text{A}} = \frac{\eta_{\text{A}}}{\tau_{\text{A}}\left(1-e^{-T_{\text{det}}/\tau_{\text{A}}}\right)}$ as a normalization factor to ensure the total probability of detecting a photon in the detection window $T_{\text{det}}$ is $\eta_{\text{A}}$, $\tau_{\text{A}}$ being the emitter lifetime, and $\Theta$ being the heaviside function.

#### DISTINGUISHABLE SCENARIO

In the distinguishable setting of a TPQI experiment, no interference occurs between the photons. We can hence express the probability of a coincidence in the output ports $C$ and $D$ of the beamsplitter with reflectivity and transmittivity parameters $R$ and $T$ as

$$p_{\text{coinc}}^{\text{dist}}(t,\Delta t) = g_{\text{CD}}(t, t+\Delta t) = \sum_{i,j,L,M} K_{ij}\, g_{ij}^{LM}(t, t+\Delta t), \tag{2.17}$$

[§]In many situations, it is desirable to keep the detection time difference $\Delta\tau$ as a parameter of the visibility $V(\Delta\tau)$ and only integrating over all possible common time shifts of the coincidence $t$. Keeping this dependence allows for the study of the effects of spectral diffusion and pure dephasing.

where $t$ is the detection time of the first photon, $K_{ij} \in \{R^2, RT, T^2\}$ is a prefactor to select the right paths for modes $i$ and $j$, and $g_{ij}(t, t+\Delta t)$ describes the correlation function between photon mode $i$ and mode $j$

$$g_{ij}^{LM}(t, t+\Delta t) = \langle p_i^L(t) p_j^M(t+\Delta t)\rangle. \tag{2.18}$$



As an example, $g_{\mathrm{ss}}^{AB}(t, t+\Delta t)$ is the correlation function for two ideal single photons from emitters $A$ and $B$ arriving at detector $C$ and $D$ at time $t$ and $(t+\Delta t)$, respectively. The correct prefactor for this term is $T^2$ as both photons need to be transmitted through the beamsplitter for this scenario. Importantly, the auto-correlation $g_{\mathrm{ss}}^{AA}$ and $g_{\mathrm{ss}}^{BB}$ vanish as we model the photons as perfect single photons.

Assembling all non-vanishing correlation functions, and integrating over all possible detection times $t$ within the detection window, we find

$$\begin{aligned} p_{\mathrm{coinc}}^{\mathrm{dist}}(\Delta t) = {} & T^2\left(g_{\mathrm{ss}}^{AB}(\Delta t) + g_{\mathrm{sn}}^{AB}(\Delta t) + g_{\mathrm{ns}}^{AB}(\Delta t) + g_{\mathrm{nn}}^{AB}(\Delta t)\right) \\ & + R^2\left(g_{\mathrm{ss}}^{BA}(\Delta t) + g_{\mathrm{sn}}^{BA}(\Delta t) + g_{\mathrm{ns}}^{BA}(\Delta t) + g_{\mathrm{nn}}^{BA}(\Delta t)\right) \\ & + RT\left(g_{\mathrm{sn}}^{AA}(\Delta t) + g_{\mathrm{ns}}^{AA}(\Delta t) + g_{\mathrm{nn}}^{AA}(\Delta t)\right) \\ & + RT\left(g_{\mathrm{sn}}^{BB}(\Delta t) + g_{\mathrm{ns}}^{BB}(\Delta t) + g_{\mathrm{nn}}^{BB}(\Delta t)\right). \end{aligned} \tag{2.19}$$

The correlation functions can be calculated independently. In the distinguishable scenario, $g_{\mathrm{ss}}^{AB}(\Delta t)$ can be easily determined by inserting the individual exponential probability distributions of the ideal single photons from eq. 2.16 into eq. 2.18 to

$$g_{\mathrm{ss}}^{AB}(\Delta t) = \frac{N_{\mathrm{A}} N_{\mathrm{B}}}{\alpha} e^{-\Delta t/\tau_{\mathrm{B}}}\left(e^{-\alpha a} - e^{-\alpha b}\right)\Theta\left(T_{\mathrm{det}} - |\Delta t|\right), \tag{2.20}$$

where $\alpha = \left(\tau_{\mathrm{A}}^{-1} + \tau_{\mathrm{B}}^{-1}\right)$, $a = \max(0, -\Delta t)$ and $b = \min(T_{\mathrm{det}}, T_{\mathrm{det}} - \Delta t)$.

For all terms involving noise contributions, an assumption about the noise has to be made to calculate its correlation with the signal photons as well as its autocorrelation. For the sake of simplicity, we limit ourselves to modeling the noise contribution as single photons (e.g. from another emitter that is similar in resonance). This leads to the same expression for $g_{\mathrm{sn}}^{AB}(\Delta t)$ as for $g_{\mathrm{ss}}^{AB}(\Delta t)$ in the distinguishable case and vanishing autocorrelations. This is of course not a general approach and a better way would be a general treatment of the noise contribution and its exact photon statistics. This would require precise knowledge about the noise, which is often not the case.

For the experiments in this thesis in Chapter 4, we will apply only single photon noise models and discuss their applicability in the specific cases.

#### INDISTINGUISHABLE SCENARIO

In the indistinguishable experiment setting, the single photons from $A$ and $B$ interfere, resulting in $g_{\mathrm{ss}}^{AB} = 0$. However, an imperfect beamsplitter, different emitter lifetimes, spectral diffusion and pure dephasing lead to non-vanishing correlations. The correlation function is derived in Ref. [43]. We add a limited detection time window to this model, which results in

$$g_{\mathrm{s\,s}}^{A\,B}(\Delta t) = \mathscr{G}_0^{(2)}(\Delta t) + \mathscr{G}_{\mathrm{int}}^{(2)}(\Delta t), \tag{2.21}$$

with

$$\mathscr{G}_0^{(2)}(\Delta t) = T^2 g_{\mathrm{s\,s}}^{A\,B}(\Delta t) + R^2 g_{\mathrm{s\,s}}^{B\,A}(\Delta t) \tag{2.22}$$

$$\mathscr{G}_{\mathrm{int}}^{(2)}(\Delta t) = \frac{-2RTe^{-\gamma|\Delta t| - 2\pi^2\Sigma^2\Delta t^2}}{(\tau_{\mathrm{A}} + \tau_{\mathrm{B}})\left(1 - e^{-\frac{T_{\mathrm{det}}}{\tau_{\mathrm{A}}}}\right)\left(1 - e^{-\frac{T_{\mathrm{det}}}{\tau_{\mathrm{B}}}}\right)} \left(1 - e^{-\alpha(T_{\mathrm{det}} - |\Delta t|)}\right) \cdot \begin{cases} 1 & \text{if } |\Delta t| \leq T_{\mathrm{det}}, \\ 0 & \text{else.} \end{cases} \tag{2.23}$$

Here, we define

$$\gamma = \Gamma_{\mathrm{A}}^* + \frac{1}{2\tau_{\mathrm{A}}} + \Gamma_{\mathrm{B}}^* + \frac{1}{2\tau_{\mathrm{B}}}, \tag{2.24}$$

$$\Sigma^2 = \sigma_{\mathrm{A}}^2 + \sigma_{\mathrm{B}}^2, \tag{2.25}$$

with $\Gamma_{\mathrm{A/B}}^*$ as the pure dephasing rate (in natural frequency) and $\sigma_{\mathrm{A/B}}$ the standard deviation of the Gaussian spectral diffusion profile (in natural frequency). From these definitions, it is clear that a measurement of $\mathscr{G}_{\mathrm{int}}^{(2)}(\Delta t)$ only allows the extraction of the combined pure dephasing and spectral diffusion magnitudes, not the individual ones.

With this modified expression for $g_{\mathrm{s\,s}}^{A\,B}$, $p_{\mathrm{coinc}}^{\mathrm{indist}}(\Delta t)$ takes the same form as Eq. 2.19. We then find the visibility for a maximum allowed detection time difference $\Delta t_{\mathrm{max}}$ as

$$V(\Delta t_{\mathrm{max}}) = 1 - \frac{\int_{-\Delta t_{\mathrm{max}}}^{\Delta t_{\mathrm{max}}} p_{\mathrm{coinc}}^{\mathrm{indist}}(\Delta t)\, d\Delta t}{\int_{-\Delta t_{\mathrm{max}}}^{\Delta t_{\mathrm{max}}} p_{\mathrm{coinc}}^{\mathrm{dist}}(\Delta t)\, d\Delta t}. \tag{2.26}$$

## 2.5. THE BARRETT-KOK PROTOCOL

The error-free Barrett-Kok protocol[42] starts with both qubits $A$ and $B$ in state $|0\rangle$, performing an $R_y(\pi/2)$ rotation, an optical $\pi$-pulse on the $|0\rangle$ state, followed by an $R_y(\pi)$ rotation and another optical pulse. For the perfect case, the optical pulse is modeled with the unitary

$$U_{\mathrm{pulse}} = \begin{cases} |0\rangle \rightarrow |0\rangle\ \hat{a}^\dagger \\ |1\rangle \rightarrow |1\rangle\,, \end{cases} \tag{2.27}$$

where $\hat{a}$ is the creation operator of the photonic mode in which the photon is emitted.

The early and late time bin are interfered respectively on a Hong-Ou-Mandel beamsplitter with $\hat{a}$ and $\hat{b}$ as inputs and $\hat{c}$ and $\hat{d}$ as outputs. The beamsplitter maps the photonic modes $\hat{a}$ ($\hat{b}$) from emitters $A$ ($B$) to

$$\hat{a} \rightarrow \frac{1}{\sqrt{2}}\left(\hat{c} + \hat{d}\right), \tag{2.28}$$

$$\hat{b} \rightarrow \frac{1}{\sqrt{2}}\left(\hat{c} - \hat{d}\right). \tag{2.29}$$

$$\tag{2.30}$$

Afterwards, the photons are detected on non-number resolving single-photon detectors. We model the heralding as a trace over all photon modes

$$\mathrm{Tr}_{\mathrm{ph}}(\rho) = \sum_{k\in\{c,d\}} \langle \mathrm{vac}|\, \hat{k}^{\dagger} \rho \hat{k}\, |\mathrm{vac}\rangle\,, \tag{2.31}$$

where $\langle \mathrm{vac}|$ is the photonic vacuum state in all modes.

Upon a detection event in both time bins *early* and *late* after the first and second optical excitation pulse, the heralded state is

$$\rho_{\mathrm{ideal}} = |\psi_{\pm}\rangle\langle\psi_{\pm}| = \frac{1}{2}\begin{pmatrix} 0 & 0 & 0 & 0 \\ 0 & 1 & \pm 1 & 0 \\ 0 & \pm 1 & 1 & 0 \\ 0 & 0 & 0 & 0 \end{pmatrix}, \tag{2.32}$$

where the + (−) sign is related to two detection events in the same (different) detectors. A detailed error model will be derived in Chapter 5.

## REFERENCES

[1] C. J. Hepp, *Electronic Structure of the Silicon Vacancy Center in Diamond*, Ph.D. thesis, Universität des Saarlandes, Saarbrücken (2014).

[2] G. Thiering and A. Gali, Ab Initio *Magneto-Optical Spectrum of Group-IV Vacancy Color Centers in Diamond,* Physical Review X **8**, 021063 (2018).

[3] U. Wahl *et al.*, *Direct Structural Identification and Quantification of the Split-Vacancy Configuration for Implanted Sn in Diamond,* Physical Review Letters **125**, 045301 (2020).

[4] R. E. Evans, A. Sipahigil, D. D. Sukachev, A. S. Zibrov and M. D. Lukin, *Narrow-Linewidth Homogeneous Optical Emitters in Diamond Nanostructures via Silicon Ion Implantation,* Physical Review Applied **5**, 044010 (2016).

[5] M. K. Bhaskar *et al.*, *Quantum Nonlinear Optics with a Germanium-Vacancy Color Center in a Nanoscale Diamond Waveguide,* Physical Review Letters **118**, 223603 (2017).

[6] A. E. Rugar *et al.*, *Narrow-Linewidth Tin-Vacancy Centers in a Diamond Waveguide,* ACS Photonics **7**, 2356 (2020).

[7] A. Sipahigil *et al.*, *An integrated diamond nanophotonics platform for quantum-optical networks,* Science **354**, 847 (2016).

[8] C. M. Knaut *et al.*, *Entanglement of nanophotonic quantum memory nodes in a telecom network,* Nature **629**, 573 (2024).

[9] T. Iwasaki *et al.*, *Tin-Vacancy Quantum Emitters in Diamond,* Physical Review Letters **119**, 253601 (2017).

[10] X. Guo *et al.*, *Microwave-Based Quantum Control and Coherence Protection of Tin-Vacancy Spin Qubits in a Strain-Tuned Diamond-Membrane Heterostructure,* Physical Review X **13**, 041037 (2023).

[11] M. Pasini, *Nanophotonics with Diamond Color Centers*, Ph.D. thesis, Delft University of Technology (2024).

[12] C. Hepp *et al.*, *Electronic Structure of the Silicon Vacancy Color Center in Diamond,* Physical Review Letters **112**, 036405 (2014).

[13] S. Meesala *et al.*, *Strain engineering of the silicon-vacancy center in diamond,* Physical Review B **97**, 205444 (2018).

[14] A. M. Stramma, *The Tin-Vacancy Centre in Diamond: A Coherent Spin-Photon Interface for Quantum Network Nodes*, Ph.D. thesis, University of Cambridge (2024).

[15] S. Niese, *Measuring Microwave Pulse Induced Heating Using Decoherence of the Tin-Vacancy Spin in Diamond*, MSc Thesis, Delft University of Technology (2022).

[16] L. J. Rogers *et al., All-Optical Initialization, Readout, and Coherent Preparation of Single Silicon-Vacancy Spins in Diamond,* Physical Review Letters **113**, 263602 (2014).

[17] B. Pingault *et al., Coherent control of the silicon-vacancy spin in diamond,* Nature Communications **8**, 15579 (2017).

[18] Y.-I. Sohn *et al., Controlling the coherence of a diamond spin qubit through its strain environment,* Nature Communications **9**, 2012 (2018).

[19] P. Siyushev *et al., Optical and microwave control of germanium-vacancy center spins in diamond,* Physical Review B **96**, 081201 (2017).

[20] M. E. Trusheim *et al., Transform-Limited Photons From a Coherent Tin-Vacancy Spin in Diamond,* Physical Review Letters **124**, 023602 (2020).

[21] E. I. Rosenthal *et al., Microwave Spin Control of a Tin-Vacancy Qubit in Diamond,* Physical Review X **13**, 031022 (2023).

[22] C. G. Torun *et al., Optical probing of phononic properties of a tin-vacancy color center in diamond,* (2023), arXiv:2312.05335 [quant-ph] .

[23] Y. Herrmann *et al., Coherent Coupling of a Diamond Tin-Vacancy Center to a Tunable Open Microcavity,* (2023), arXiv:2311.08456 [quant-ph] .

[24] E. Neu *et al., Low-temperature investigations of single silicon vacancy colour centres in diamond,* New Journal of Physics **15**, 043005 (2013).

[25] J. N. Becker and C. Becher, *Coherence properties and quantum control of silicon vacancy color centers in diamond,* physica status solidi (a) **214**, 1700586 (2017).

[26] E. Neu, M. Agio and C. Becher, *Photophysics of single silicon vacancy centers in diamond: Implications for single photon emission,* Optics Express **20**, 19956 (2012).

[27] T. Iwasaki *et al., Germanium-Vacancy Single Color Centers in Diamond,* Scientific Reports **5**, 12882 (2015).

[28] R. Høy Jensen *et al., Cavity-Enhanced Photon Emission from a Single Germanium-Vacancy Center in a Diamond Membrane,* Physical Review Applied **13**, 064016 (2020).

[29] J. Görlitz *et al., Spectroscopic investigations of negatively charged tin-vacancy centres in diamond,* New Journal of Physics **22**, 013048 (2020).

[30] I. Karapatzakis *et al., Microwave Control of the Tin-Vacancy Spin Qubit in Diamond with a Superconducting Waveguide,* Physical Review X **14**, 031036 (2024).

[31] P. Wang *et al., Transform-Limited Photon Emission from a Lead-Vacancy Center in Diamond above 10 K,* Physical Review Letters **132**, 073601 (2024).

[32] H. K. C. Beukers *et al.*, *Control of Solid-State Nuclear Spin Qubits Using an Electron Spin- 1 / 2,* Physical Review X **15**, 021011 (2025).

[33] M. Pompili, *Multi-Node Quantum Networks with Diamond Qubits*, Ph.D. thesis, Delft University of Technology (2021).



[34] M. H. Abobeih *et al.*, *One-second coherence for a single electron spin coupled to a multi-qubit nuclear-spin environment,* Nature Communications **9**, 2552 (2018).

[35] K. D. Jahnke *et al.*, *Electron–phonon processes of the silicon-vacancy centre in diamond,* New Journal of Physics **17**, 043011 (2015).

[36] N. Codreanu, *Diamond Nanophotonic Devices for Quantum Networks Experiments*, Ph.D. thesis, Delft University of Technology (2025).

[37] B. Khanaliloo, M. Mitchell, A. C. Hryciw and P. E. Barclay, *High-Q/V Monolithic Diamond Microdisks Fabricated with Quasi-isotropic Etching,* Nano Letters **15**, 5131 (2015).

[38] J. M. Brevoord *et al.*, *Heralded initialization of charge state and optical-transition frequency of diamond tin-vacancy centers,* Physical Review Applied **21**, 054047 (2024).

[39] I. T. Raa *et al.*, *QMI - Quantum Measurement Infrastructure, a Python 3 framework for controlling laboratory equipment,* 4TU.ResearchData (2023).

[40] C. K. Hong, Z. Y. Ou and L. Mandel, *Measurement of subpicosecond time intervals between two photons by interference,* Physical Review Letters **59**, 2044 (1987).

[41] T. Legero, T. Wilk, A. Kuhn and G. Rempe, *Time-resolved two-photon quantum interference,* Applied Physics B **77**, 797 (2003).

[42] S. D. Barrett and P. Kok, *Efficient high-fidelity quantum computation using matter qubits and linear optics,* Physical Review A **71**, 060310 (2005).

[43] B. Kambs and C. Becher, *Limitations on the indistinguishability of photons from remote solid state sources,* New Journal of Physics **20**, 115003 (2018).

# 3

# CONTROL OF SOLID-STATE NUCLEAR SPIN QUBITS USING AN ELECTRON SPIN-1/2

**H. K. C. Beukers*, C. Waas*, M. Pasini, H. B. van Ommen, Z. Ademi, M. Iuliano, N. Codreanu, J. M. Brevoord, T. Turan, T. H. Taminiau & R. Hanson**

*Solid-state quantum registers consisting of optically active electron spins with nearby nuclear spins are promising building blocks for future quantum technologies. For electron spin-1 registers, dynamical decoupling (DD) quantum gates have been developed that enable the precise control of multiple nuclear spin qubits. However, for the important class of electron spin-1/2 systems, this control method suffers from intrinsic selectivity limitations, resulting in reduced nuclear spin gate fidelities. Here we demonstrate improved control of single nuclear spins by an electron spin-1/2 using Dynamically Decoupled Radio Frequency (DDRF) gates. We make use of the electron spin-1/2 of a diamond tin-vacancy center, showing high-fidelity single-qubit gates, single-shot readout, and spin coherence beyond a millisecond. The DD control is used as a benchmark to observe and control a single $^{13}C$ nuclear spin. Using the DDRF control method, we demonstrate improved control on that spin. In addition, we find and control an additional nuclear spin that is insensitive to the DD control method. Using these DDRF gates, we show entanglement between the electron and the nuclear spin with* 72(3) *% state fidelity. Our extensive simulations indicate that DDRF gate fidelities well in excess are feasible. Finally, we employ time-resolved photon detection during readout to quantify the hyperfine coupling for the electron's optically excited state. Our work provides key insights into the challenges and opportunities for nuclear spin control in electron spin-1/2 systems, opening the door to multi-qubit experiments on these promising qubit platforms.*

The results of this chapter have been published in Physical Review X, **15**, 021011 (2025).
* Equally contributing authors

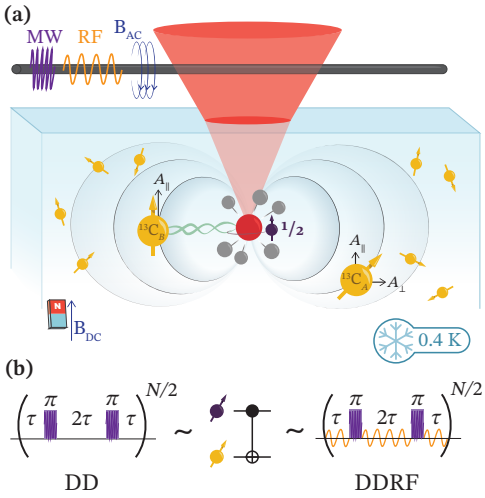


Figure 3.1: **Nuclear spin control with electron spin-1/2.** (a) The electron spin-1/2 of a negatively charged tin-vacancy center in a ⟨100⟩ surface-oriented diamond (purple spin) is initialized and read out by a red laser. The electron spin is controlled using the AC magnetic field of microwave (MW) radiation (purple sine) through a wire (gray line) spanned over the diamond. The surrounding nuclear spins (yellow spins) have a unique parallel and perpendicular hyperfine coupling ($A_\parallel$ and $A_\perp$) to the electron spin. This allows conditional control with the electron spin and generation of entanglement (green link). The nuclear spins can be directly driven using radiofrequency (RF) radiation (yellow sine). (b) Nuclear spin control is achieved by dynamical decoupling (DD) and dynamically decoupled radio frequency (DDRF) gates. For DD gates, interpulse delays $\tau$ resonant with the nuclear spin dynamics cause a rotation conditioned on the electron spin state. For DDRF gates, the interpulse delays do not need to follow the dynamics of the target nuclear spin: direct spin-state selective radio frequency driving with tailored phase updating enables a conditional rotation of the nuclear spin. Both techniques perform CNOT-equivalent gates.

## 3.1. INTRODUCTION

Optically interfaced electron spins in the solid state are promising platforms for quantum networking, computing, and sensing[1]. Prominent examples are color centers[2–7] and single rare-earth ions[8–11]. These electron spins offer fast control[12–14] and high-fidelity readout[15–17]. Moreover, their spin-photon interface enables remote entanglement generation[18], while their solid-state nature facilitates on-chip integration[19]. The use of surrounding nuclear spins as long-lived memory qubits further enhances the functionality of the electron spins. For example, these electron-nuclear registers have enabled recent demonstrations of fault-tolerant quantum computing[20], memory-assisted quantum communication[17] and a multi-node quantum network[21,22].

A key requirement for establishing coherent quantum gates between the electron and nuclear spins is the protection of the electron spin coherence during the gate[23]. For this, different control methods have been developed, such as dynamical decoupling (DD) control[24] and dynamically decoupled radio frequency (DDRF) control[25]. Nuclear spin control using the DD method has been shown in different platforms including color centers in diamond[26–28], silicon carbide[29] and single rare-earth ions[10]. In these

decoherence-protected control methods, the selectivity of the control critically depends on the electron spin magnitude. Notably, the important class of electron spin-1/2 systems, which includes the silicon T centers[30,31] and the diamond group-IV color centers[32–35], has an intrinsically reduced selectivity for the DD control method compared to spin systems with a higher magnitude[10,28,36,37]. It has been hypothesized that the DDRF control method improves the selectivity for these interesting electron spin-1/2 systems[25].

In this work, we experimentally explore and investigate the control of two nuclear spins with the electron spin-1/2 of the negatively charged tin-vacancy (SnV) center in diamond (Fig. 3.1(a)), using both the DD and DDRF control (Fig. 3.1(b)). The SnV center has recently emerged as a highly promising quantum system because of its excellent optical and spin properties, compatibility with nanophotonic integration and operating temperature of above one Kelvin[19,38–46]. We provide a detailed selectivity comparison of spin-1/2 and spin-1 systems in simulation. Furthermore, we investigate the nuclear spins' coupling to the SnV center's excited state during the optical readout of the electron spin.



## 3.2. ELECTRON SPIN CONTROL

Our experiments are performed on a chemical vapor deposition grown diamond that is implanted with $5 \times 10^{10}$ ions/cm$^2$ of spinless $^{120}$Sn at a target depth of 88 nm and subsequently annealed at 1100 °C[46]. The diamond contains the natural abundance of carbon isotopes, including 1.1 % $^{13}$C, which has a nuclear spin-1/2. A wire is spanned over the diamond sample to deliver the microwave and radio frequency signals. A $^3$He-cryostat with a confocal optical microscope cools the sample to 0.4 K. We align a bias magnetic field of 0.1 T with the symmetry axis of the SnV center, see Fig. 3.1(a).

We use the negatively charged tin-vacancy (SnV) center throughout this work. The electronic waveform of the SnV center is a spin and orbital doublet in the ground and excited state, as depicted in Fig. 3.2(a). The spin-orbit interaction and lattice strain lift this degeneracy. At temperatures below 1.5 K thermal occupation of the higher levels is negligible, resulting in an effective spin-1/2 system. The other levels are still observable in effects like an anisotropic g-factor, reduced microwave driving efficiency, and an optical cyclicity that depends on the magnetic field alignment[34].

The electron spin qubit is initialized and read out optically with a 619 nm laser. In Fig. 3.2(b), a photoluminescent excitation (PLE) measurement shows the two spin-conserving transitions split by 611(3) MHz due to a difference in the $g$-factors of the ground and excited states. The SnV center is initialized in the correct charge state and the optical lines are ensured to be on resonance with the laser by a charge-resonance check[47]. The single-shot readout is implemented by spin-selective optical excitation of the spin-down transition[48]. The bright $|0\rangle$ state is assigned in case at least one photon is recorded; otherwise the $|1\rangle$ state is assigned. A finite spin-flipping probability during optical cycling causes readout infidelity of the bright $|0\rangle$ state, whereas noise counts limit the readout fidelity of the dark $|1\rangle$ state. These two contributions are optimized in Fig. 3.2(c), resulting in an average readout fidelity of 77.7(3) %. Note that single-shot readout can be achieved in this setup despite a low collection efficiency of approximately

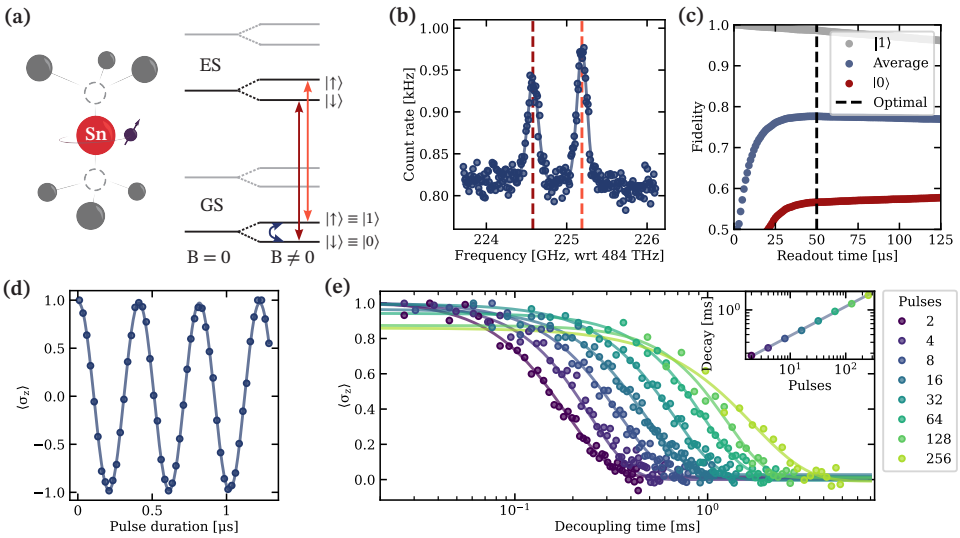


Figure 3.2: **Electronic qubit characterization.** (a) Schematic lattice and level structure of the SnV center. The negatively charged SnV center consists of an interstitial tin atom with two carbon vacancies and an additional electron. The ground and excited states behave as an effective spin-1/2 system at low temperatures. The lowest two levels of the ground state form a spin-1/2 qubit and are connected to the excited state via an optical transition at 619 nm. (b) Photoluminescence excitation measurement of the two spin-conserving transitions in (a). (c) Single-shot readout calibration curve. The splitting of the optical transitions allows for spin-selective readout via optical excitation. The qubit is initialized into an eigenstate. A single-shot readout result of 0(1) is assigned when detecting at least one photon (no photon) during the excitation of the spin-down transition. The best average fidelity determines the optimal readout time. (d) Microwave control of the SnV center electron spin qubit. The fit of this Rabi oscillation is used to determine the duration of $\pi/2$ and $\pi$ pulses. (e) Electron coherence measurement with dynamical decoupling. We employ XY8 sequences with a varying number of $\pi$ pulses. Increasing the number of decoupling pulses beyond 100 creates heating in this device, which shows up as a lowered contrast.

0.2 %, thanks to the high cyclicity of approximately 1200 of this SnV center.

Initialization of the qubit is achieved by spin pumping, where a laser, on resonance with the spin-up transition, excites the electron. The finite spin-flipping probability during optical decay causes initialization into the spin-down state. The initialization fidelity of 98.1(5) % is deduced from the residual fluorescence at the end of spin pumping for 300 µs and can be readily improved by implementing a longer spin pumping time or using a higher laser power.

The electron spin is controlled by microwave driving with a Rabi frequency of 2.46 MHz, as shown in Fig. 3.2(d). The average fidelity of the calibrated gates is measured using process tomography to be 98(2) %. The investigated SnV center has a spin dephasing time of $T_2^* = 2.42(4)$ µs, see Appendix 3.9.3. The coherence is extended by XY8 dynamical decoupling of the electron spin to $T_2^{\mathrm{DD}} = 1.7(5)$ ms using 256 $\pi$ pulses[49]. The observed scaling of the coherence during DD in Fig. 3.2(e) matches

$$T_2^{\mathrm{DD}} = T_2^{\mathrm{Echo}} N^{\chi}, \tag{3.1}$$

where $N$ is the number of decoupling pulses, $T_2^{\mathrm{Echo}} = 129(2)$ µs is the fitted constant equivalent to the single echo coherence, and $\chi = 0.47(1)$ is the scaling factor.

To investigate the limiting effect for the $T_2^{\mathrm{Echo}}$, we perform a double electron-electron resonance (DEER) measurement, see Appendix 3.9.3. In the DEER, we simultaneously apply an echo pulse on the SnV center electron spin and at the MW frequency of free electron spins with a $g$-factor of 2. This DEER shows a reduced coherence time for the SnV electron spin, which points to the presence of an electron spin bath as a noise source in this device. The found scaling factor $\chi$ is close to the one found in the recent experiments in samples with a comparable implantation dose of tin ions[34]. From simulations, they attribute the decoherence to the electron spin bath caused by implantation. Better coherence of the electron spin has been achieved in samples with a hundredfold lower implantation dose[50].

## 3.3. DYNAMICAL DECOUPLING CONTROL

The hyperfine coupling between the electron spin of the SnV center and the surrounding $^{13}$C spins is caused by the dipole-dipole interaction and the Fermi contact hyperfine interaction[51]. Therefore, the coupling is dependent on their relative distance and orientation. A single nuclear spin can be controlled by targeting its unique hyperfine coupling. Strongly coupled $^{13}$C can be observed directly in optically detected magnetic resonance (ODMR) of the electron spin[52,53]. However, more weakly coupled spins, where the coupling is smaller than $1/T_2^*$ of the electron spin, are not resolvable by ODMR. To observe and control them, one needs to extend the coherence of the electron spin at the same time. Dynamical decoupling of the electron spin brings the detection limit down to the inverse of the coherence time of the electron spin under dynamical decoupling $1/T_2^{\mathrm{DD}}$ [24,54,55].

The Hamiltonian of a single $^{13}$C spin, in the secular approximation, is

$$H_{\mathrm{hf}} = \omega_L I_z + A_{\parallel} S_z I_z + A_{\perp} S_z I_x, \tag{3.2}$$

where $S_i$ and $I_i$ are the spin operators for the electron and nucleus, respectively, and $\omega_L = \gamma_c B_z$ is the Larmor frequency of the $^{13}$C spin with $\gamma_c/2\pi = 10.71\,\mathrm{MHz\,T^{-1}}$. $A_{\parallel}$ and

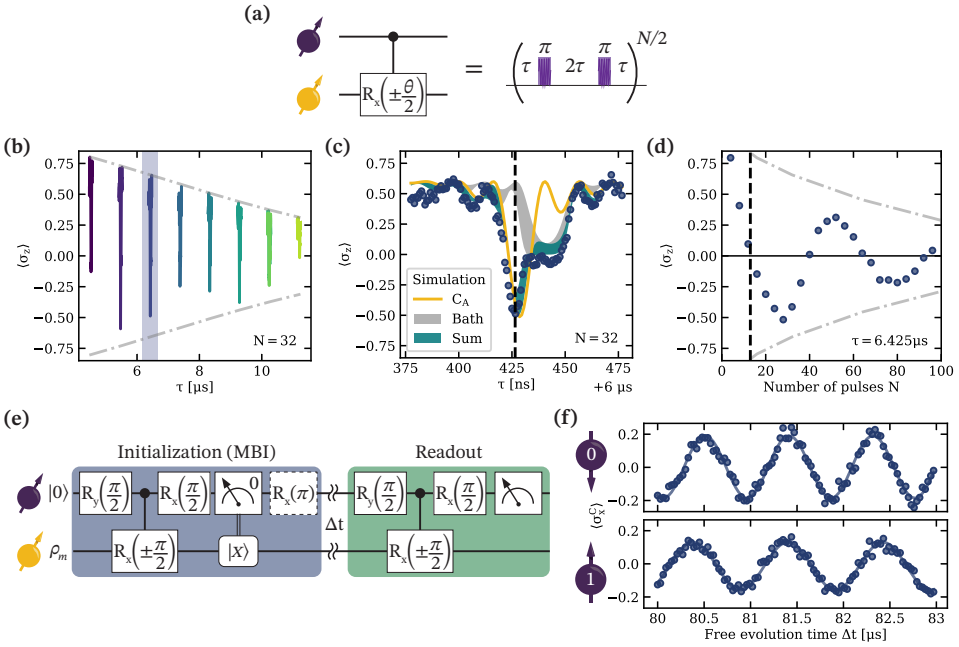


Figure 3.3: **Dynamical decoupling nuclear spin control.** (a) A dynamical decoupling sequence performs a conditional rotation if $\tau$ fulfills the resonance condition of the nuclear spin. (b) Dynamical decoupling sequence for varying interpulse delay $\tau$. The dips in the coherence indicate coupling to the nuclear spins around. The dashed line indicates the contrast limit due to the electron coherence. (c) Enlargement of the shaded region of $\tau$ in (b). The gray area shows the effect of the spin bath on the electron spin. The spread stems from simulating many different configurations of the spin bath. The narrow dip stems from an individual nuclear spin $C_A$, where the yellow line is the simulated response. The blue area is the simulated combined effect of the bath and the nuclear spin $C_A$. Appendix 3.9.5 describes the simulations. (d) Nuclear gate calibration. By fixing $\tau = 6.425\mu$s (dashed line in (b)) and varying the number of decoupling pulses $N$, coherent control of the nuclear spin can be observed by the oscillation of the electron coherence. The fully entangling gate is achieved when $\langle\sigma_z\rangle = 0$. The gray dashed line indicates the contrast limit due to the electron coherence. (e) Pulse sequence for nuclear Ramsey measurement. The nuclear spin is prepared via a measurement-based initialization (MBI). The controlled gate is achieved by the DD gate characterized in (c) and (d). A measurement of $|0\rangle$ of the electron at the end of the sequence projects the nuclear spin into $|x\rangle$. An optional $\pi$ pulse allows for measuring the evolution of the nuclear spin for both electron spin states. After a free evolution time $\Delta t$, the nuclear spin is measured in the $x$ basis through the electron spin. (f) Ramsey signal of the nuclear spin dependent on the electron spin state. The precession frequency of the nuclear spin changes depending on whether the electron is kept in $|0\rangle$ or flipped to $|1\rangle$ after the MBI. The measured frequencies are $\omega_0/2\pi = 1116.1(2)$ kHz and $\omega_1/2\pi = 985.4(3)$ kHz.

$A_\perp$ are the parallel and perpendicular hyperfine parameters, with respect to the external magnetic field, depicted in Fig. 3.1(a). As a result of this Hamiltonian, the precession axis of the nuclear spin depends on the state of the electron as

$$\vec{\omega}_i = (s_i A_\perp, 0, \omega_L + s_i A_\parallel), \tag{3.3}$$

where $s_i$ is the spin projection of the electron spin for qubit state $|i\rangle$ [36].

Nuclear spins can be detected and controlled using the dynamical decoupling sequence of the electron. The nuclear spin precesses around a different axis depending on the electron spin state. Periodically changing between these two rotation axes can give rise to a conditional rotation of the nuclear spin [24,54,55], as depicted in Fig. 3.3(a). To control a nuclear spin with DD, the $\pi$ pulses on the electron spin need to be applied in resonance with the dynamics of the nuclear spin. In the high magnetic field regime ($\omega_L \gg A_\parallel, A_\perp$), the resonant condition is met when the $\tau$ of the decoupling sequence is

$$\tau_p \approx \frac{(2p+1)\pi}{2\bar{\omega}}, \tag{3.4}$$

where $p$ is the order of the resonance and $\bar{\omega} = (\omega_0 + \omega_1)/2$ is the average nuclear precession frequency. To target a specific nuclear spin, a unique $\tau_p$ is required to avoid crosstalk with other spins. Therefore, the selectivity of the DD control method depends on a difference in the average nuclear precession frequency $\bar{\omega}$. Expanding it in hyperfine parameters gives [36]

$$\bar{\omega} = \omega_L \left[ 1 + \frac{s_0 + s_1}{2} \frac{A_\parallel}{\omega_L} + \frac{s_0^2 + s_1^2}{4} \left( \frac{A_\perp}{\omega_L} \right)^2 \right]. \tag{3.5}$$

The first-order term drops out of the expression if $s_0$ and $s_1$ have opposite signs and the same magnitude. In a spin-1/2 system, this is unavoidable, resulting in a second-order selectivity in $A_\perp$. In contrast, in systems with a larger spin magnitude, one can choose the spin projections to achieve a first-order sensitivity in $A_\parallel$.

Low magnetic fields will give a stronger influence of $A_\perp/\omega_L$, which benefits the nuclear spin selectivity in spin-1/2 systems. However, this usually results in a trade-off, as the magnetic field also influences other properties. For the SnV center, for example, a lower field comes at the cost of less separation between the optical transitions and, therefore, reduced optical initialization and readout fidelity for the electron spin qubit.

In Fig. 3.3(b), we first use the DD method to detect the nuclear spins around the SnV center by sweeping $\tau$ for 32 decoupling pulses. As this conditional interaction acts like $S_z I_x$, the electron spin can be used as a sensor by applying the conditional gate while the electron is in a superposition. For this, we prepare the electron spin in $|x\rangle = (|0\rangle + |1\rangle)/\sqrt{2}$ using a $\pi/2$ pulse, and, after the decoupling sequence, we use another $\pi/2$ pulse to map the $x$ basis to the $z$ basis for readout. A conditional gate entangles the electron spin with the nuclear spin, which shows up as a loss of coherence of the electron spin in Fig. 3.3(b). A drop in coherence to $\langle \sigma_z \rangle = 0$ can be caused by coupling to many different spins. A value below that shows a coherent interaction with a single spin system [24]. The nuclear spin bath, composed of spins that have small coupling and cannot be resolved individually, shows up at $\tau \approx \frac{2p+1}{4}\tau_L$, where $\tau_L = 2\pi/\omega_L$ is the Larmor period. In Fig. 3.3(c), the dip in coherence around $\tau = 6.45\,\mu$s is shown. Next to the nuclear spin bath, we observe

one dip separate from the bath, which goes well below $\langle\sigma_z\rangle = 0$, indicating coherent coupling. We calibrate a two-qubit gate with this spin based on the DD spectrum by using the $\tau$ of the center of the dip. The number of pulses in the DD sequence is swept in Fig. 3.3(d), where $\langle\sigma_z\rangle = 0$ indicates the number of pulses required for a maximally entangling gate (dashed line). The decay of the signal is caused by a combination of loss of coherence of the electron spin and residual crosstalk with the spin bath.

The control over the nuclear spin allows us to perform a Ramsey experiment using the sequence in Fig. 3.3(e), where the nuclear spin is prepared in $|x\rangle$ and read out in the $x$ basis. The state of the nuclear spin can be read out by entangling it with the electron spin and reading out the electron spin. We initialize the nuclear spin using measurement-based initialization (MBI)[56], where measuring the electron spin to be $|0\rangle$ prepares $|x\rangle$ on the nuclear spin. A Ramsey measurement is performed in Fig. 3.3(f) by varying the time between the MBI and measurement. After the MBI, the electron spin is in $|0\rangle$, and the Ramsey shows $\omega_0/2\pi = 1116.1(2)$ kHz. Adding a $\pi$ pulse after the MBI allows the measurement of $\omega_1/2\pi = 985.4(3)$ kHz.

In the system of the electron spin of the SnV center and the $^{13}$C nuclear spin, there is no direct measure of the magnetic field. The electronic $g$-factor depends on the unknown strain in the lattice. For the nuclear spin, the unknown hyperfine coupling always influences the precession frequency of the $^{13}$C spin, as there is no spin-0 projection of the electron. Therefore, we extract the Larmor frequency of the $^{13}$C spins from a fit to Fig. 3.3(d), yielding $\omega_L/2\pi = 1048.52(8)$ kHz. From this we extract $A_\parallel/2\pi = -130.9(3)$ kHz and $A_\perp/2\pi = 137(6)$ kHz for this $^{13}$C spin $C_A$. We have corrected for small changes in magnetic field strength between different measurements, see Appendix 3.9.4. We can observe and control this nuclear spin using the DD control method because it has a significantly large $A_\perp$ that separates its resonance enough from the nuclear spin bath, whereas the resonances of other nuclear spins overlap with the nuclear spin bath.

## 3.4. DYNAMICALLY DECOUPLED RADIO FREQUENCY CONTROL

Dynamical Decoupled Radio Frequency (DDRF) control has been suggested to yield a better selectivity for a spin-1/2 system than DD control[25]. In DDRF, a direct drive of the nuclear spin is combined with coherence protection of the electron spin using dynamical decoupling. The most direct way of driving the nuclear spin is with radio frequency (RF) radiation. The required RF driving frequency $\omega_i$ depends on the electron spin state $|i\rangle$ as described by Eq. 3.3. The electron spin coherence must be extended with DD while driving the nuclear spin. To make it work in practice, we need to apply the RF driving pulses in phase with the nuclear spin evolution. Van Ommen *et al.*[57] extend the original work on DDRF[25] with a more precise and generalized analysis that includes the effects of the bandwidths of the RF pulses.

To achieve the desired nuclear spin evolution the phase of the RF pulses is updated after each $\pi$ pulse on the electron spin with

$$\delta\phi = 2\tau\bar{\omega} + \pi, \tag{3.6}$$

where $\bar{\omega} = (\omega_0 + \omega_1)/2$ is the average nuclear spin precession frequency. The $2\tau\bar{\omega}$ is the

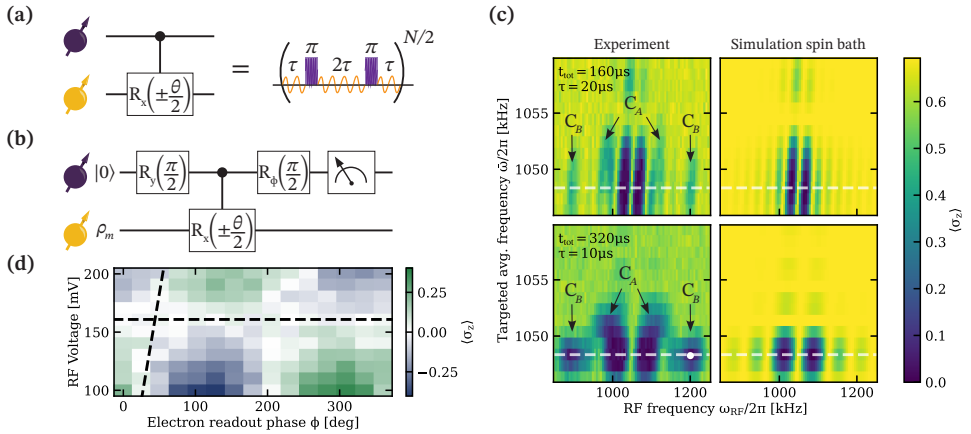


Figure 3.4: **Dynamical decoupled radio frequency (DDRF) control.** (a) A DDRF gate is realized by direct RF driving of the nuclear spin during the interpulse delay of the DD sequence. (b) The sequence to calibrate the gate. The angle $\theta$ is calibrated with the applied RF power. The angle $\phi$ of the second $\pi/2$ gate is calibrated to counteract a phase that the electron picks up due to the RF driving. (c) DDRF spectrum. For each data point in the left panels, the sequence in (b) is measured for multiple electron readout $\pi/2$ pulse phases $\phi$ and fitted to a sine function to account for phases picked up during the RF pulses. The amplitude of the sine is a measure for $\langle\sigma_z\rangle$. The values for $\tau$ are chosen such that for both values of $N$, the expected electron coherence at the end of the sequence is similar. The right panels show a simulation of the Hamiltonian for a collection of weakly coupled spins to imitate the nuclear spin bath, which is described in Appendix 3.9.5. Additionally to the characteristic bath features, two coupled spins (indicated by the arrows) are observable. The white dashed line indicates $\omega_L$. The solid white circle is the used operating point in (d). (d) Nuclear spin gate calibration. The controlled gate can be calibrated by varying the electron readout $\pi/2$ pulse phase and the RF voltage. A fit of the full data with a heuristic model determines the correct voltage for the controlled gate as well as the additional phase picked up by the electron during the gate (dashed lines). After the RF pulses are generated with the reported voltages, they are amplified by 32 dB.

phase update required to follow the spin evolution such that the RF drive induces rotations along a fixed axis in the rotation frame of the nuclear spin. The $\pi$ phase makes the rotation conditional as it inverts the rotation axis for the opposite electron spin state. As the phase update rule depends on $\bar{\omega}$, it has a similar selectivity as the DD control. However, the direct driving of the spin RF frequency, typical of DDRF control, increases its selectivity.

The Fourier transform of the pulse's temporal shape determines the frequency response of the RF drive[57]. For a square pulse of length $2\tau$ it is



$$\Omega(\Delta,\tau) \propto \mathrm{sinc}(\Delta\tau), \tag{3.7}$$

where $\Delta = \omega - \omega_{\mathrm{RF}}$ is the detuning from the RF driving frequency, and $\mathrm{sinc}(x) = \sin(x)/x$. For a typical $\tau$ used in this work, around 5 µs, this sets an upper bound for the selectivity of the RF drive of around 100 kHz. In our experiments, the power broadening of the nuclear spin transition can be neglected as it is around 2 kHz.

As the DDRF control method also gives an effective $S_z I_x$ interaction, like the DD method, similar detection and control circuit diagrams can be used[24]. The DDRF control method now performs the conditional gate, as depicted in Fig. 3.4(a). The DDRF gate depends on both the used RF frequency $\omega_{\mathrm{RF}}$ and the targeted average precession frequency $\bar{\omega}$ through the phase update rule, resulting in a two-dimensional DDRF spectrum. This spectrum is achieved by the gates in Fig. 3.4(b).

In Fig. 3.4(c), we show the resulting spectra for two different decoupling sequences, both using a Rabi frequency of 1.64 kHz. We compare the spectra to simulations of the nuclear spin bath. In this way, we can see which resonances are caused by the bath and which ones show the presence of controllable single nuclear spins. Our measurements show the known nuclear spin $C_A$, as indicated in Fig. 3.4(c). However, there are also resonances belonging to another nuclear spin $C_B$. This nuclear spin has an average precession frequency close to $\omega_L$ (white dashed line), indicating a small $A_\perp$. The splitting between the dips of $\omega_0$ and $\omega_1$ for $C_B$ indicates $A_\parallel/2\pi \approx 300$ kHz. This nuclear spin was not visible in the DD measurements as that method requires a high $A_\perp$ to make it stand out from the bath.

In the spectra, the width of the resonances in targeted $\bar{\omega}$ (vertical) is inversely proportional to the total gate duration, as this is the time over which a difference in $\bar{\omega}$ can build up a phase difference. The width of the resonances in $\omega_{\mathrm{RF}}$ (horizontal) is inversely proportional to the $\tau$ used, as this corresponds to the frequency width of the RF pulse[57].

Nuclear spins have different combinations of $A_\parallel$ and $A_\perp$, resulting in various combinations of $\bar{\omega}$ and $\omega_{\mathrm{RF}}$ for the resonances. This means that the two parameters need to be searched independently to find the different nuclear spins. This is different in a spin-1 system, such as the nitrogen-vacancy center in diamond, when using $s_0 = 0$ and $s_1 = \pm 1$, where the hyperfine parameters influence only $\omega_1$, with $\omega_0$ being constant. For a spin-1, the search space can be reduced to a one-dimensional slice as $\omega_0$ is known in advance.

The high symmetry of the DD sequence, in combination with the symmetric spin projections of a spin-1/2 system, causes the loss of first-order selectivity in the phase update rule. To circumvent this, we explored the use of the less symmetric Uhrig Dynamical Decoupling (UDD) sequence[58] for the DDRF gate, which is discussed in Appendix 3.9.7. The UDD gives differently shaped resonances, which, in our case, causes separation of

the nuclear spin $C_A$ from the bath. However, in our system where the noise spectrum has no hard cutoff, UDD decoupling is inferior to the XY8 decoupling sequence[49], resulting in lower electron coherence, and is therefore not further pursued.

In previous work[25], only a single driving frequency was used, effectively reducing the nuclear spins' driving to half the time. For the spectroscopy in Fig. 3.4(c) we apply the same approach. However, for calibrated DDRF gates, we drive the nuclear spin at both $\omega_0$ and $\omega_1$, making the driving more efficient and reducing heating. Simulations of our experiments show that a double drive with a driving strength of $\Omega/2$ for both transitions is equivalent to a single drive with $\Omega$. For simplicity and consistency, we describe the experiments and theory in this work as if a single drive was used for the DDRF gates.



The dips in the coherence of the electron spin show which combination of $\omega_{\mathrm{RF}}$ and $\bar{\omega}$ can be used to control the nuclear spin. We use the right dip of $C_B$ (white dot) to control it. At this operating point, the RF amplitude is swept in the sequence of Fig. 3.4(b) to calibrate the DDRF gate. A fully entangling gate is created by setting the RF amplitude to the point where $\langle\sigma_z\rangle = 0$ (Fig. 3.4(d)). The phase of the electron spin is also calibrated as the magnetic part of the RF radiation adds an extra phase to the electron spin, which needs to be compensated. We measure the nuclear spin precession frequencies using a nuclear magnetic resonance (NMR; see Appendix 3.9.8) experiment extracting $\omega_0/2\pi = 896.02(3)$ kHz and $\omega_1/2\pi = 1200.49(3)$ kHz for $^{13}$C spin $C_B$, which translates to $A_\parallel/2\pi = 304.45(5)$ kHz and $A_\perp/2\pi = 0(13)$ kHz. For $C_A$, we observe an improved contrast compared to the DD method, indicating that we can better separate this spin from the bath. For the best gate settings, we find a contrast of 0.23 (0.23) for a Ramsey measurement with the electron spin in state $|0\rangle$ ($|1\rangle$) compared to the contrast of 0.19 (0.14) via DD control.

## 3.5. ELECTRON-NUCLEAR ENTANGLEMENT

To use the DDRF gate on $C_B$ for entangling the electron and nuclear spin, we first optimize the gate through simulation in Fig. 3.5(a), using the hyperfine parameters determined in the previous section. For this, we simulate the required RF Rabi frequencies for fully entangling gates with different total lengths and $\tau$. The effective Rabi frequency depends on the total length of the gate and the amount of off-resonant driving of the other nuclear transition. This off-resonant driving occurs because the RF pulse has a finite sinc-shaped frequency bandwidth[57]. Taking the RF Rabi frequency, total gate time, and $\tau$, we simulate the effect of the presence of a nuclear spin bath. Furthermore, the coherence of the electron needs to be preserved for a high-fidelity gate. Therefore, we calculate the coherence of the electron for different DD sequences based on the measurement in Fig. 3.2(e). By combining these two contributions to the infidelity, we get an estimate for the fidelity of a full two-qubit gate. We choose an operating point that gives the highest fidelity within the region of achievable Rabi frequencies ($\Omega/2\pi < 3.1$ kHz). After the choice of the operation point, the simulation was further refined to the one depicted here, showing that a higher gate fidelity might have been possible.

For the optimization, there is a trade-off between preserving electron coherence and gate performance. Shortening the total gate time improves electron coherence but requires a higher Rabi driving frequency. Increasing $\tau$ improves the RF selectivity as the

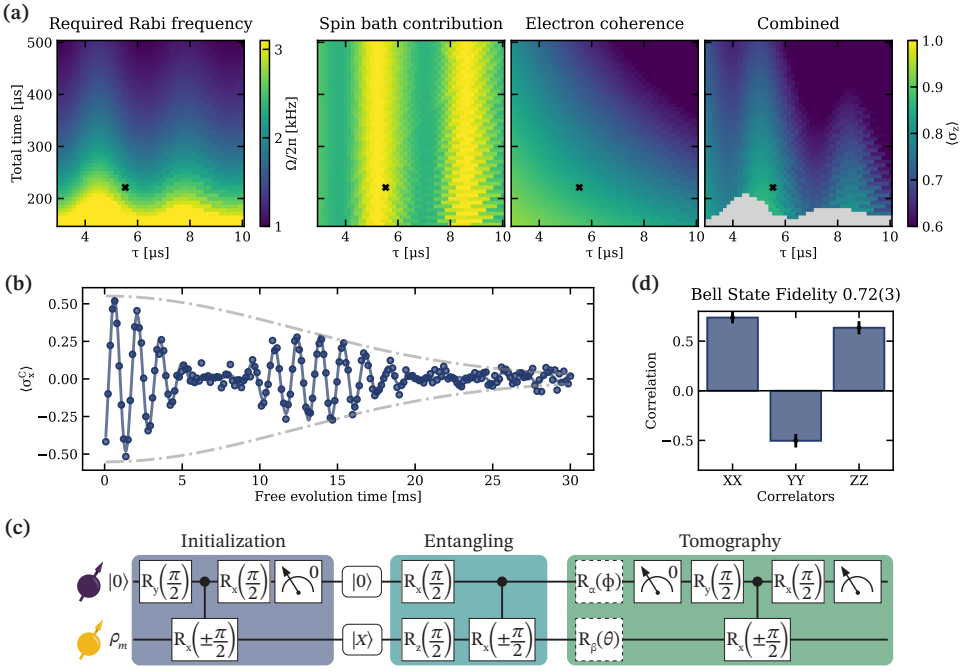


Figure 3.5: **Gate optimization and electron-nuclear entanglement.** (a) Gate parameter simulation. A set of $\tau$ and the total gate duration puts a requirement on the Rabi frequency that needs to be achieved for a gate with $\theta = \pi/2$. For specific values of $\tau$, the spectral shape of the RF tone also drives the other nuclear spin transition (i.e. driving $\omega_0$ while targeting $\omega_1$), resulting in a higher required Rabi frequency $\Omega$ to compensate for this off-resonant driving[57]. The gate fidelity is determined by the combination of electron coherence during DD and extra coherence loss due to the applied DDRF gate. Considering the fidelity and excluding gates with a Rabi frequency higher than the maximally achievable 3.1 kHz (gray region), we choose the working point indicated by the cross. (b) Measurement of the nuclear $T_2^*$ via a Ramsey sequence. The fit accounts for two coupled spins that induce a beating of the Ramsey signal. The envelope (gray dashed line) has the form $A\exp\left(-(t/T_2^*)^n\right)$ with $n = 2.0(2)$ and decay time $T_2^* = 17.2(6)$ ms. (c) Gate sequence for electron-nuclear entanglement. The nuclear spin is prepared into $|x\rangle$ via MBI. The entangling block creates the Bell state $|\Phi^+\rangle$, which is consecutively measured with different correlators. The tomography pulses on the nuclear spin are realized by Larmor precession ($z$-rotations) or direct RF driving. (d) Correlators of the $|\Phi^+\rangle$ state. The error bars indicate their standard deviation. The readout of the nuclear spin in the tomography block is corrected for errors in the two-qubit gate, resulting in an entangled state fidelity of $\mathcal{F}_{\text{Bell}} = 0.72(3)$.

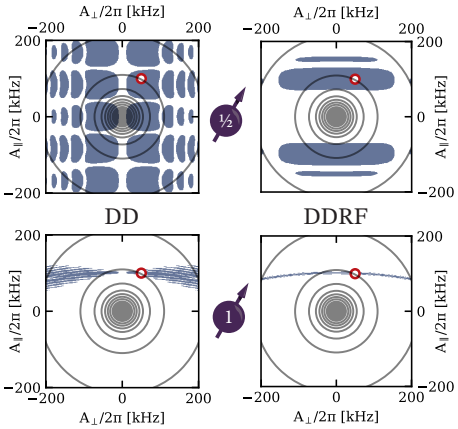


Figure 3.6: **Comparison of nuclear spin control with DD and DDRF methods.** Simulated crosstalk regimes when controlling a target nuclear spin with $A_\parallel/2\pi = 100\,\text{kHz}$ and $A_\perp/2\pi = 50\,\text{kHz}$ (red circle). DD and DDRF control methods are compared for electron spin-1/2 and spin-1. The blue areas correspond to hyperfine parameters for which a bystander nuclear spin would cause more than 5 % decoherence of the electron spin, during a gate performed on the target nuclear spin. The regions between the gray circles contain, for a natural $^{13}$C abundance of 1.1 %, on average one bystander $^{13}$C nuclear spin. For simulation details, see Appendix 3.9.5.

pulse bandwidth is reduced but lowers the electron coherence. Besides this, higher-order resonances with the nuclear spin bath can be avoided by carefully selecting appropriate values for $\tau$.

In Fig. 3.5(b), the optimized gate is used in an undersampled Ramsey measurement on $C_B$. The observed beating pattern is explained by a coupling to two different nuclear spins with 67(4) Hz and 71(4) Hz. The $T_2^* = 17.2(6)\,\text{ms}$ of this nuclear spin is comparable to high values measured using the nitrogen-vacancy center in diamond[25]. We extract a two-qubit gate fidelity of $\mathcal{F}_{\text{gate}} = 0.874(4)$ (see Appendix 3.9.6 for details), which is slightly less than the simulated fidelity $\mathcal{F}_{\text{sim}} = 0.915$. We attribute the difference to the decoherence of the electron spin to coupling to undetected spins, which are not captured by the spin bath simulation.

With this two-qubit gate, we have the tools to entangle the SnV electron spin with the $^{13}$C spin. For this, we initialize the $^{13}$C spin, prepare the electron in a superposition state, and use the two-qubit entangling gate to create the Bell state $|\Phi^+\rangle = \frac{1}{\sqrt{2}}(|00\rangle + |11\rangle)$; see Fig. 3.5(c). The correlators are measured with tomography, from which the fidelity to the Bell state $|\Phi^+\rangle$ is calculated as $\mathcal{F} = (\langle XX\rangle - \langle YY\rangle + \langle ZZ\rangle + 1)/4$. By correcting for known tomography errors, as explained in Appendix 3.9.6, we find a fidelity to the Bell state $|\Phi^+\rangle$ of 72(3) %. As discussed in Appendix 3.9.6, this is mainly limited by the electron coherence loss during the nuclear spin gates.

## 3.6. COMPARISON CONTROL METHODS

In previous sections, we explored the experimental control of $^{13}$C spin with a spin-1/2 electron spin using the DD and DDRF control methods. In this section, we compare the

selectivity of these two methods in simulation. Additionally, we analyze the difference for the case of an electron spin-1 system[24,57]. The different nuclear spins surrounding the electron spin can be characterized by their specific $A_\parallel$ and $A_\perp$. Figure 3.6 visualizes the selectivity of both control methods. We simulate a nuclear spin gate for a nuclear spin with $A_\parallel/2\pi = 100\,\text{kHz}$ and $A_\perp/2\pi = 50\,\text{kHz}$ (red circle). The blue region indicates for which hyperfine parameters a bystander spin would cause more than 5 % coupling to the electron during the same gate.



For each scenario, the most selective gate is found by optimizing the gate parameters under the boundary conditions that the electron has preserved more than 99 % coherence and the gate does not exceed 1 ms. For the simulations, we assume an electron echo time of $T_2^{\text{Echo}} = 1\,\text{ms}$, dynamical decoupling scaling factor $\chi = 2/3$ and a maximum nuclear Rabi frequency of 5 kHz.

The likelihood of having a bystander spin in the blue areas depends on the distribution of hyperfine parameters of the nuclear spins surrounding the color center. The placement of $^{13}$C atoms around a color center in the diamond lattice is probabilistic, resulting in a varying arrangement of the bystander spins for different centers. We simulate the distribution of nuclear spin hyperfine parameters by generating many different random spin configurations and calculating their hyperfine parameters. The distribution of hyperfine parameters of bystander spins is visualized by the regions between the gray lines, which contain on average one nuclear spin. More simulation details can be found in Appendix 3.9.5.

We observe that the selectivity for DD in spin-1/2 systems is reduced compared to spin-1[28]. Most notably, there is considerable crosstalk with the nuclear spin bath, i.e., the spins with a weak coupling. We note that the specific analysis depends on the chosen target spin. For example, spins with lower $A_\perp$ have more crosstalk for DD control with electron spin-1/2.

The DDRF method has an enhanced selectivity compared to the DD method as it introduces an extra resonance requirement. Both methods depend on $\bar{\omega}$, DDRF through its phase update rule and DD through the interpulse delay. However, the RF drive in DDRF additionally targets $\omega_0$ or $\omega_1$, which have a first-order dependence on $A_\parallel$, also for electron spin-1/2 systems. This reduces the crosstalk, most notably with the spin bath. The first-order selectivity of the phase update rule scales with the total gate time $2\tau N$ in spin-1 systems and the first-order RF selectivity scales with the interpulse delay $2\tau$ for both systems. Therefore, DDRF for spin-1 systems has a factor $N$ better selectivity[57].

## 3.7. HYPERFINE COUPLING WITH THE EXCITED STATE

So far, we have considered the hyperfine interaction with the ground state of the SnV electron spin. However, the performed Ramsey measurements also give us insight into the hyperfine interaction in the excited state. We observe that the nuclear spin acquires a phase depending on how much time the electron is in the excited state.

During measurement-based initialization (MBI), we use a readout of the electron that is stopped when a photon is detected. This yields the most reliable assignment of the postmeasurement state but also results in a variable readout time. During the readout, the electron spin gets cycled between the ground and excited states. Therefore,

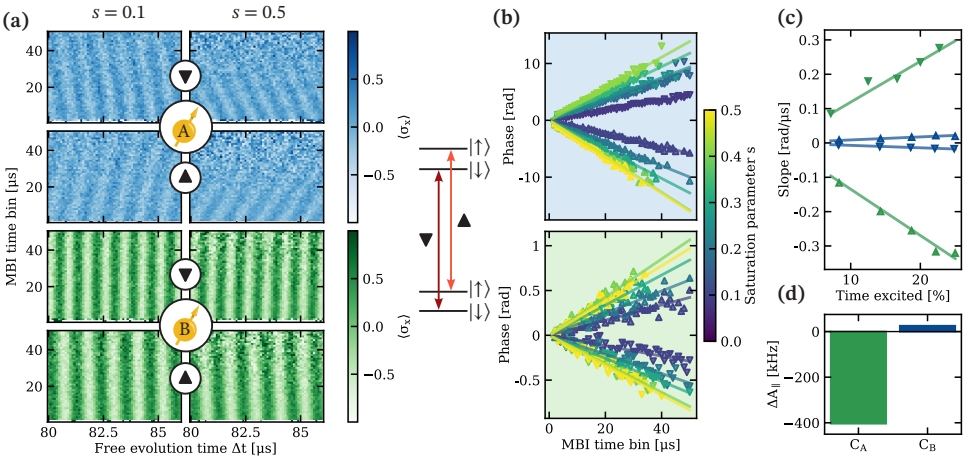


Figure 3.7: **Excited state hyperfine coupling.** (a) The Ramsey measurements of the nuclear spins are binned for the readout time during MBI. We find an additional phase shift depending on the duration of the readout. The blue (green) colored data correspond to $C_A$ ($C_B$). The rate of acquiring phase increases for higher laser powers (left and right column), i.e., longer occupation of the excited state. Changing the optical transition used for the readout during MBI (▲ or ▼) flips the direction of the phase shift. The difference in contrast stems from the better gate fidelities for $C_B$ compared to $C_A$. (b) Extracting the phase shift for different MBI durations and saturation numbers $s$ results in linear slopes. (c) The used power in (b) is converted to time spent in the excited state and shows a linear relation with the slope fitted in (b). (d) The difference in parallel hyperfine parameters between the excited and ground states for both nuclear spins.

the time the electron spends in the excited state depends on the optical power and the readout duration.

In Fig. 3.7(a), Ramsey measurements for $C_A$ and $C_B$ are binned by the readout duration during MBI. We observe that the Ramsey fringes are shifted for longer readout durations, indicating that the nuclear spin acquired an extra phase during readout. Furthermore, the shift depends on the readout power. We use the saturation parameter $s = P/P_{\text{sat}}$, to compare the readout power $P$ to the saturation power $P_{\text{sat}} \approx 88\,\text{nW}$. The observed shift is more significant for a readout with $s = 0.5$ in the right column than a readout with $s = 0.1$ in the left column. Lastly, we see that reading out using the spin-down transition (▼ in Fig. 3.7) results in the opposite shift compared to reading out using the spin-up transition (▲ in Fig. 3.7). The more noisy data for longer readout duration are a consequence of the small amount of data resulting from a low probability of detecting the first photon at those times.

We attribute the extra phase to a different hyperfine coupling of the $^{13}$C spin to the SnV electron in the ground and the excited states. Note that these effects can be avoided in integer-spin systems such as the diamond nitrogen-vacancy center by using an $m_S = 0$ optical transition. Intuitively, as the excited state exhibits a different electron wave function, the coupling to the $^{13}$C can differ from that of the ground state. We can extract the acquired additional phase from the binned Ramsey measurements in the excited state. Figure 3.7(b) shows the fitted phases for the binned Ramsey fringes in Fig. 3.7(a), which are well explained by a constant phase acquisition. Based on saturation measurements,

the readout power can be converted to a fraction of the time spent in the excited state (see Sec. 1.7 in Ref.[59]):

$$t_{\text{exc}}/t = \frac{s}{2s+1}. \tag{3.8}$$

The factor 2 in the denominator stems from the readout being done resonantly, capturing the contribution of stimulated emission. Figure 3.7(c) shows the angular frequency corresponding to the additional phase acquisition as a function of the fraction of time spent in the excited state. Combining this occupancy with the additional phase acquisition in the excited state gives the difference in coupling, which can mainly be assigned to a difference in $A_\parallel$ between the ground and excited states, as a difference in $A_\perp$ has a small second-order effect on the precession frequencies; see Appendix 3.9.9. The extracted difference in parallel hyperfine coupling $\Delta A_\parallel = A_\parallel^e - A_\parallel^g$ is $-404(2)$ kHz and 25.2(4) kHz as displayed in Fig. 3.7(d). The contrast of the Ramsey measurements is mostly preserved for longer readout durations. The exponential decay constant of the Ramsey contrast is $7.5(3) \times 10^2$ and $28(1) \times 10^2$ optical cycles for $C_A$ and $C_B$ respectively, suggesting the nuclear spins are a viable storage of qubit states during optical operations on the electron spin.

## 3.8. DISCUSSION AND OUTLOOK

We have investigated the nuclear spin control using an electron spin-1/2 system. We have shown an improved selectivity in controlling nuclear spins using Dynamically Decoupled Radio Frequency (DDRF) control compared to the more commonly used Dynamical Decoupling (DD) control. Using these methods, we control two nuclear spins and show entanglement between the nuclear spin of a $^{13}$C atom and the electron spin of a tin-vacancy (SnV) center in diamond.

These findings directly translate to other systems with an electron spin-1/2, such as rare-earth ions[10] and many other color centers like the silicon-vacancy and other group-IV vacancy centers in diamond[7,35,53], the T center in silicon[31] and the vanadium center in silicon carbide[60].

Decoupling with longer $\tau$ improves the RF selectivity. Longer gates allow for better phase selectivity. Both these factors improve the selectivity for a single gate, allowing the control of more $^{13}$C spins. In this work, the electron coherence limits the electron-nuclear gate fidelity. This is not intrinsic to the SnV center or the nuclear spins but can be attributed to the presence of an electron spin bath. Recently, it has been shown that the SnV can indeed have longer coherence times during dynamical decoupling[50], which would improve the nuclear spin control as well.

The selectivity of the nuclear spin gates with DDRF is better than with DD for electron spin-1/2. However, it is still reduced compared to spin systems with a larger magnitude. To counteract this, less symmetric decoupling sequences[61], like the UDD[58], can be explored to increase the selectivity of DDRF further.

The selectivity of the nuclear spin gates in electron spin-1/2 systems can be further improved by interleaving a single DD or DDRF gate by periods in which the electron spin is in an eigenstate. In these periods, the nuclear spins will precess with $\omega_i$ as opposed to $\bar{\omega}$ during decoupling, thereby recovering the first-order selectivity to $A_\parallel$ of spin-1 systems. To preserve the state of the electron spin during those periods, it needs to be tem-

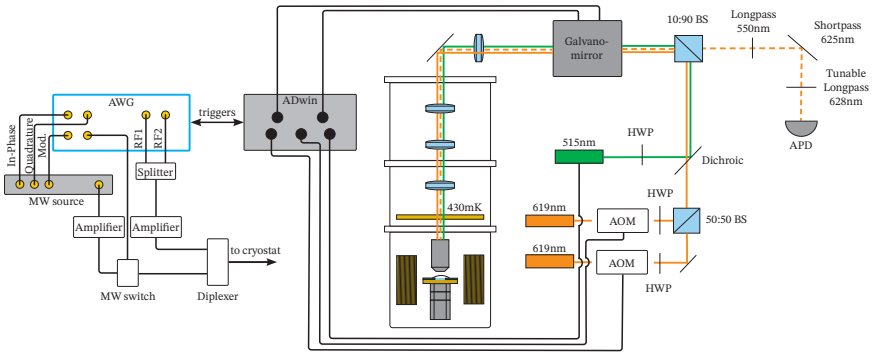


Figure 3.8: **Experimental Setup.** The setup consists of a cryostat with optical access, control electronics, and optical excitation and collection paths. The dashed line represents the fluorescence from the SnV center. A detailed description is provided in the text.

porarily stored in an easily accessible quantum memory[62]. In the SnV center, this role could be fulfilled by the nuclear spin of $^{117}$Sn or $^{119}$Sn[63].

Lastly, we investigated the hyperfine coupling of the nuclear spins with the excited state of the electron, showing a different coupling in the excited state compared to the ground state of the electron. Additionally, we can conclude that it also showed that the nuclear spins surrounding the SnV center stay coherent while the optical transition is cycled hundreds of times, making these memories robust against the optical readout of the electron spin.

The improved selectivity of the DDRF control and the insights in nuclear spin coupling during readout bring high-fidelity spin control in electron spin-1/2 systems closer.

The data and simulations that support this manuscript are available at 4TU.ResearchData[64].

## 3.9. SUPPLEMENTARY INFORMATION

### 3.9.1. EXPERIMENTAL SETUP

The setup is schematically shown in Fig. 3.8. The center of the setup is a BlueFors LD250He system with a base temperature of 430 mK with a 1-1-1 T vector magnet. A positioner stack provides movement of the device. Confocal microscopy experiments are performed with a high-NA objective and a double-4f system with a two-axis galvanomirror. Microwaves and radiofrequency drives are supplied via superconducting coaxial cables (not shown in the figure) and a flex-cable to allow movement of the device (not shown in the figure). To minimize heating, the signal is guided via a custom printed circuit board to a bondwire $\approx 100\,\mu$m above the device. The total microwave losses through the system at the relevant frequency 3.1 GHz are 5 dB.

The experiment is controlled via a home-written software infrastructure based on QMI[65]. A microcontroller (ADwin Pro II, Jäger Messtechnik) controls the experiment, and laser pulses are controlled via its DAC module. For microwave and radio-frequency

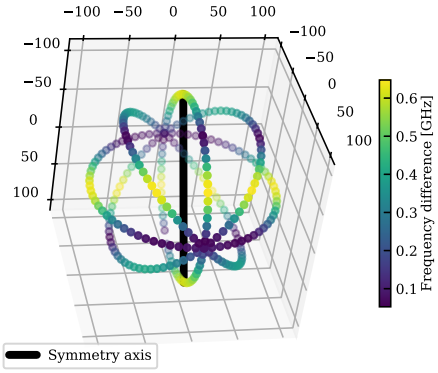


Figure 3.9: **Magnetic field sweep.** The frequency difference of the two spin-conserving optical transitions is shown as a function of the 3D magnetic field in the laboratory frame in units of mT. The solid black line shows the direction of the SnV center symmetry axis. In laboratory spherical coordinates, it is oriented along $(\theta,\phi) = (54.2(1)^\circ, -1.0(2)^\circ)$.

pulses, the ADwin triggers an arbitrary waveform generator (HDAWG, Zurich Instruments). The HDAWG modulates a microwave signal generator (SGS100A, Rohde & Schwarz) with IQ-signals to generate phase-controlled microwave pulses. The microwave pulses are amplified (Model 40S1G4, Amplifier Research) to 26 dBm for all measurements in the main text, which yields an estimated power of 20 dBm at the device location. To prevent the shot noise of the amplifier during free evolution periods from entering the system, a microwave switch and high-pass filter (not in the figure) are employed. The radio frequency signals are directly generated by oscillators of the HDAWG and amplified to 18 dBm. The transmission for these megahertz signals is almost lossless. We use two driving frequencies for the control with DDRF gates and drive both resonance frequencies of the nuclear spin, resulting in a $\sqrt{2}$ improvement of the Rabi frequency for the same power. These two driving tones are combined with a directional coupler and then via a diplexer with the microwave signal. An additional DC-block (not in the figure) after the diplexer completes the chain.

The electron spin is addressed optically via a confocal microscopy setup. Two resonant excitation lasers (DLpro SHG-TA, Toptica) are modulated via the ADwin and AOMs (Fiber-Q 637nm, Gooch&Housego) and combined via a beamsplitter. An off-resonant repump laser at 515nm (Cobolt 06-03-MLD515, Hübner Photonics) is added with a dichroic mirror. The excitation light is coupled into the beam path of the cryostat through a 10:90 beam splitter and the galvanomirror. The collected light is spectrally filtered (FELH0600, Thorlabs; FF625-SDi01 and TLP01-628, Semrock) and detected by a single photon detector (COUNT, LaserComponents). A counter module of the ADwin stores the registered counts in 1 µs time bins.

### 3.9.2. MAGNETIC FIELD SWEEP

We investigate the behavior of the SnV center by sweeping the magnetic field along four great circles with magnetic field strength 100 mT (see Fig. 3.9). We monitor the frequen-

Table 3.1: Magnetic field fitting parameters.

| Term | Value | Origin |
|---|---|---|
| $\lambda_g/2\pi$ | 830 GHz | [34] |
| $\lambda_e/2\pi$ | 2988 GHz | [34] |
| $B$ | 97.8 mT | Appendix 3.9.4 |
| $\theta_{\mathrm{SnV}}$ | 54.2(1)° | Fit |
| $\phi_{\mathrm{SnV}}$ | −1.0(2)° | Fit |
| $\Upsilon_g$ | 352(7) GHz | Fit |
| $\Upsilon_e$ | 674(17) GHz | Fit |
| $f_g$ | 0.171 | [34] |
| $f_e$ | 0.072 | [34] |
| $\delta_g$ | 0.015 | [34] |
| $\delta_e$ | 0.176 | [34] |



cies of both spin-conserving transitions with PLE measurements. We model the SnV center Hamiltonian as described in Ref.[34], Eq. B5. To extract relevant parameters from the available data, we have to fix some Hamiltonian parameters. Specifically, our PLE measurements do not give us access to the ground-state splitting.

Fitting the resulting data with the SnV center Hamiltonian with the strain and the laboratory orientation of the SnV center as free parameters, we find a laboratory direction of the SnV center symmetry axis of $(\theta,\phi) = (54.2(1)°, -1.0(2)°)$. Since we use a ⟨100⟩-cut diamond with ⟨110⟩ side faces, these values match the expectation given the alignment of the diamond with respect to the magnet. The strain values result in $\Upsilon_g = 355(8)$ GHz and $\Upsilon_e = 689(20)$ GHz for the ground and excited state, respectively. This moderate strain is smaller than the spin-orbit coupling in both manifolds, yet allows for direct driving of the microwave transition. The fit parameters are summarized in Table 3.1.

### 3.9.3. ELECTRON COHERENCE

#### RAMSEY

To investigate the coherence of the electron spin, we conduct a Ramsey measurement. We perform the experiment on resonance and vary the phase of the second $\pi/2$ pulse to artificially introduce the signature of a detuning with $\Delta = 5$ MHz. The resulting signal in Fig. 3.10(a) shows a slow beating in addition to the oscillation with $\Delta$. A fit of two sine functions with a power exponential envelope

$$\langle\sigma_z\rangle(t) = A\exp\left(-\left(\frac{t}{T_2^*}\right)^n\right)\sum_{i=1,2}\left(\sin\left(\omega_i t+\phi_i\right)\right)+c \tag{3.9}$$

reveals a frequency difference of 312(3) kHz of the sines, coinciding with the coupling strength of $C_B$ in the main text. The decay of the envelope with exponent $n = 2.8(2)$ leads to $T_2^* = 2.42(4)$ µs. An exponent bigger than one indicates that the coherence is limited by slow-varying noise in the spin bath, which can possibly be counteracted by dynamical decoupling. This result is in accordance with the expected Ramsey coherence time of color centers in naturally abundant diamond[66].

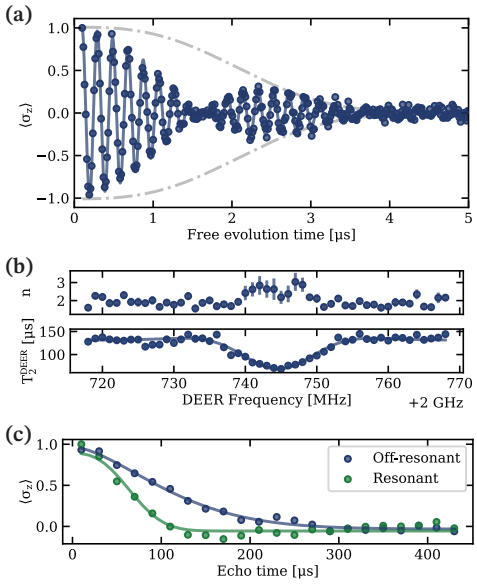


Figure 3.10: **Electron Ramsey and DEER measurements.** (a) Ramsey measurement. The Ramsey measurement is performed with an artificial detuning of 5 MHz, implemented via an evolution time-dependent phase on the second $\pi/2$ gate. The beating frequency of 312(3) kHz. (b) The frequency of the second MW pulse in the DEER measurement is varied to find the resonance of the electron spin bath. Both the echo time and the power of the power exponential fit in Eq. 3.9 are given. The error bars indicate their standard deviation. (c) Two examples of the Hahn echo measurements from (b), where a resonant MW pulse with the electron spin bath decreases the coherence time of the Hahn echo.

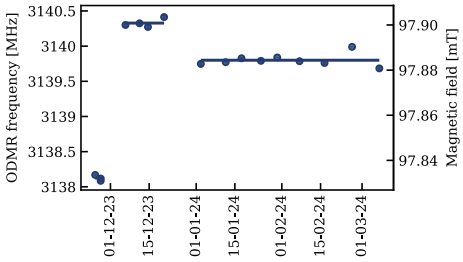


Figure 3.11: **Magnetic field strength over time.** The changes in the magnetic field strength are monitored using the MW frequency of the electron spin, through an ODMR measurement.



### DEER

The scaling of the coherence time $T_2^N = T_2^{\text{Echo}} N^{\chi}$ with $T_2^{\text{Echo}} = 129(2)\,\mu\text{s}$ with the number of pulses $N$ via $\chi = 0.47(1)$ is less than we expect for a pure nuclear spin bath limitation[67]. We conduct a double electron-electron resonance (DEER) measurement to verify electron bath noise. When measuring the Hahn echo decay time of the electron spin while applying a microwave pulse with varying frequency simultaneously to the decoupling pulse, we see a clear reduction of the coherence time when driving the surrounding with 2.745 GHz, see Fig. 3.10(b). We extract the decay constant $\tau$ and the exponent $n$ from the function

$$T_2^{\text{DEER}} = A \exp\left(-(t/\tau)^n\right). \tag{3.10}$$

We find a spin bath resonance frequency of 2.7446(2) GHz. This corresponds very well with electrons with a $g$-factor of 2 and a magnetic field of 97.884 mT, as determined in Appendix 3.9.4. The $T_2^{\text{DEER}} = 76(4)\,\mu\text{s}$ has significantly decreased compared to a $T_2^{\text{Echo}} = 128(5)\,\mu\text{s}$. The origin of this spin bath noise is unknown; it might stem from crystal damage due to insufficient annealing or residual tin ions in the surrounding.

## 3.9.4. MAGNETIC FIELD STRENGTH CHANGES

During the experiments, the magnetic field strength has not been constant as shown in Fig. 3.11, hampering direct comparison between measurements. As we have no direct measure of the magnetic field, we use the MW transition frequency of the electron spin, as measured by the ODMR measurements over time, to keep track of the relative magnitude of the magnetic field. The orientation of the magnetic field also influences the MW transition frequency, but as this is a second-order effect[34] we neglect this contribution. We observe three periods in which the magnetic field was stable. We suspect that switching the superconducting magnet to persistent mode caused the first jump and temporarily warming up to 4 K caused the second one. Using these relative variations in the field strength allowed us to fit Fig. 3.3(d) while using the $\omega_0$ and $\omega_1$ extracted from Fig. 3.3(f) to determine the Larmor frequency. This Larmor frequency could then be converted to an absolute magnetic field strength by using the gyromagnetic ratio of the nuclear spin, as indicated in Fig. 3.11. The reported value of $\omega_L$ in the main text is based on the second time period.

### 3.9.5. SIMULATIONS

All the code to generate the figures in this paper, including the simulations are available in the repository supporting this manuscript[64].

#### DD

The DD simulations are all based on the analytic formulas from Ref.[36], which describe both electron spin-1/2 and spin-1 systems.



To simulate the nuclear spin bath, we first generate a random distribution of the nuclear spins. For this, we randomly place the nuclear spins in a sphere with radius 30 nm around the electron spin with a density corresponding to 1.1 % $^{13}$C atoms. The hyperfine parameters are then calculated by assuming just the dipole-dipole interaction. For the DD spin bath simulations only spins with a hyperfine coupling $A/2\pi < 100\,\text{kHz}$ are included, where $A = \sqrt{A_\parallel^2 + A_\perp^2}$.

For Fig. 3.3(c), ten different realizations of the spin bath are generated, and the region between the highest and lowest line is shown.

#### DDRF

For the DDRF simulations in Figs. 3.4(b), 3.5(a) and 3.13 numerical methods based on the Python framework QuTiP[68] are used to simulate the Hamiltonian of the RF drive from Ref.[57]. These simulations include the exact pulse shape and length as were used in our experiments. For the comparison in Fig. 3.6 the analytic formulas from Ref.[57] are used.

The simulations of the nuclear spin bath in Figs. 3.4(b), 3.5(a) and 3.13 are based on the spin bath simulations in Ref.[57]. Rather than simulating a randomly generated nuclear spin bath, we approximate it with a probability distribution of the hyperfine parameters. For the distribution of $A_\parallel$, we take the heuristic distribution from the supplement of Ref.[69]. We assume that the nuclear spin bath has $A_\perp = 0\,\text{kHz}$, as the bath has weak coupling and $A_\perp$ has only a second-order effect on $\omega_0$ and $\omega_1$, which are the parameters relevant for the DDRF simulation. In this work, we consider spins with a $|A_\parallel|/2\pi < 20\,\text{kHz}$ to be part of the spin bath for the DDRF simulations as these spins are below our detection limit. We then subdivide the distribution of the bath in bins of $\Delta A_\parallel = 2\,\text{kHz}$ and weigh their effect by the number of expected spins in that bin. Finally, we combine the effect of the different bins on the electron to get the effect of the whole nuclear spin bath.

#### COMPARISON

The comparison in Fig. 3.6 is performed by finding the coherent and fast two-qubit gate on the target spin that minimizes the crosstalk with bystander spins. We consider it fast and coherent if the electron coherence after the gate is above 99 % and the total gate duration is below 1 ms. A bystander spin is considered to cause crosstalk for a gate if the loss in the coherence of the electron due to this bystander spin is bigger than 5 %. The gate is optimized to cause crosstalk with the fewest possible bystander spins, i.e., minimizing the blue region in Fig. 3.6. This metric is not weighted for the bystander spin density.

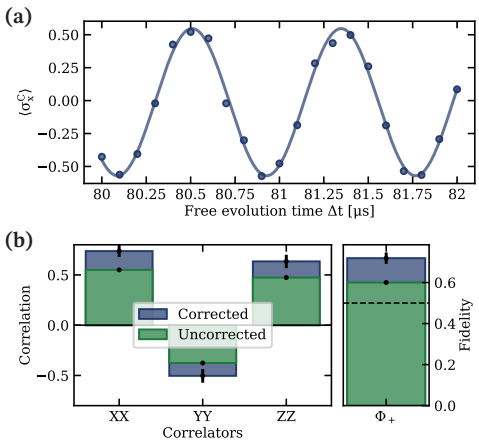


Figure 3.12: **Readout correction for Bell state measurement.** (a) Ramsey measurement to determine two-qubit gate fidelity. The contrast of the Ramsey measurement is reduced due to imperfect two-qubit gates. For the measurement, the two-qubit gate is performed to initialize and read out the nuclear spin. A model based on imperfect state preparation and positive operator-valued measure (POVM) measurements yields $\mathscr{F}_{\text{gate}} = 0.874(4)$. (b) Data for the Bell state measurement in Fig. 3.5(d), including the outcomes without correcting for the two-qubit gate fidelity. The error bars show the standard deviation.

For the DD method, the gate with the smallest crosstalk is found by sweeping the interpulse delay $\tau$ and the number of decoupling pulses $N$. For the DDRF method, the interpulse delay $\tau$, the number of decoupling pulses $N$, and the RF driving strength $\Omega$ are swept to find the most selective gate.

The circles indicating the bystander spin density are based on the average of 100 randomly generated spin bath configurations. The spin baths are generated in the same way as for the DD spin bath simulations, see Appendix 3.9.5.

### 3.9.6. BELL STATE

#### READOUT GATE CORRECTION

When determining the fidelity of the Bell state $|\Phi^+\rangle$ in the main text, we apply a readout correction to the nuclear spin readout via MBI. To this end, we estimate the two-qubit gate fidelity $\mathscr{F}_{\text{gate}}$ via a Ramsey measurement. The fit of a sinusoidal function to Fig. 3.12(a) shows an amplitude of $\langle\sigma_x\rangle = 0.559(12)$. We model the imperfect initialization and readout of the nuclear spin in the $x$ basis with the preparation of state

$$\rho = \begin{pmatrix} \mathscr{F}_{\text{gate}} & 0 \\ 0 & 1-\mathscr{F}_{\text{gate}} \end{pmatrix}, \tag{3.11}$$

and readout via a POVM measurement with the matrix set

$$E_x = \begin{pmatrix} \mathscr{F}_{\text{gate}} & 0 \\ 0 & 1-\mathscr{F}_{\text{gate}} \end{pmatrix}, \quad E_{-x} = \begin{pmatrix} 1-\mathscr{F}_{\text{gate}} & 0 \\ 0 & \mathscr{F}_{\text{gate}} \end{pmatrix}. \tag{3.12}$$

The expectation value of this model is

$$\langle\sigma_x\rangle = 1\cdot p_x - 1\cdot p_{-x} = 1 - 4\mathscr{F}_{\text{gate}} + 4\mathscr{F}_{\text{gate}}^2, \tag{3.13}$$

Table 3.2: Gate fidelites of electron (e) and nuclear (n) spin.

| Gate | Fidelity | Method |
|---|---|---|
| Init. (e) | 0.981(5) | Calibration |
| Init. (n) | 0.874(4) | Ramsey contrast |
| $R(\pi/2)$ (e) | 0.98(2) | Process tomography |
| $R_z(\pi/2)$ (n) | 1 | Calibration |
| $cR_x(\pm\pi/2)$ | 0.874(4) | Ramsey contrast |
| $R_{x,y}(\pi/2)$ (n) | - | Undetermined |



with $p_i = \mathrm{Tr}\left(\rho E_i\right)$. Solving for the gate fidelity results in $\mathscr{F}_{\mathrm{gate}} = 0.874(4)$. This value is slightly below the simulated gate fidelity shown in Fig. 3.5(a) of 0.915. We attribute this difference to the coupling of the electron spin to unknown spins.

We use the estimated fidelity to perform a readout correction following the formalism outlined in Ref.[21], Appendix A. The uncorrected and corrected data of the Bell state measurement is shown in Fig. 3.12(b).

#### ERROR BUDGET ESTIMATION

The measured Bell state does not have perfect fidelity. This section provides an overview of the known and unknown sources of infidelity to estimate the expected fidelity for the Bell state measurements.

The experimental gate sequence as shown in Fig. 3.5(c) is comprised of three logic blocks with single- and two-qubit gates.

In the "Initialization" block, both the electron spin and nuclear spin are prepared into known states $|0\rangle$ and $|x\rangle$. The probability of correctly measuring the electron in state $|0\rangle$ after the two-qubit gate is 98 %, mainly limited by the spin pump fidelity. The correct initialization of the nuclear spin is limited by the two-qubit gate fidelity of 87.4 %.

The "Entangling" block consists of a $\pi/2$ gate on the electron spin, a $z$ rotation of the nuclear spin (implemented by a waiting time, assumed to be perfect) and a two-qubit gate identical to the initialization. We determine the average electron spin gate fidelity to 0.98(2) via process tomography.

The last block, "Tomography", consists of another single-qubit rotation on the electron spin as well as the nuclear spin, followed by a single-shot readout of both qubits individually. To prepare the nuclear spin for a readout in the $x$ or $y$ basis, a $z$ rotation is performed via a waiting time. The error of this gate is determined by the uncertainty of the Ramsey frequency, which we determine to be less than $1 \times 10^{-4}$ relative error in the main text. For readout in the $z$ basis, a direct RF gate is implemented as reported in Appendix 3.9.8. This gate is calibrated via a Rabi experiment. However, the fidelity of the gate has not been determined. We correct for the readout processes following the description of Appendix A of Ref.[21] for the electron spin and Appendix 3.9.6 for the nuclear spin.

All known and unknown fidelities are listed in Table 3.2.

To estimate the expected fidelity of the Bell state measurement, we use a simplified model in which we assume all gates except the $cR_x(\pm\pi/2)$ to be perfect for simplicity, as their infidelity is small compared to the two-qubit gate. We describe the two-qubit gate

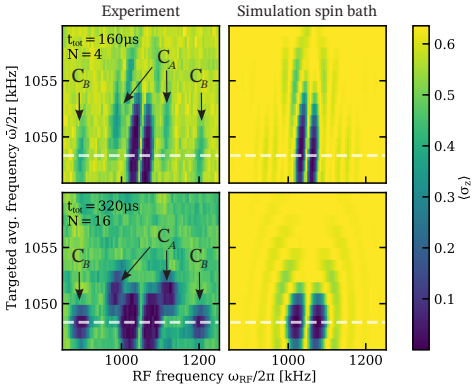


Figure 3.13: **DDRF Spectrum using the UDD sequence.** The same DDRF spectrum as in Fig. 3.4(c) but now implemented with UDD. The upper row is using 4, while the bottom row is using 16 decoupling pulses.

as an ideal gate with probability $p = \mathcal{F}_{\text{gate}}$ and an ideal gate with an additional phase error on the electron with probability $1-p$. With this phase error, we take the loss of coherence of the electron spin during the gate into account, which is the main reason for the gate infidelity, as detailed in Fig. 3.5(a). For the modeling, we exclude the tomography pulses and, hence, compare the calculated value to the readout-corrected measured fidelity.

The estimated fidelity of the created Bell state with the sequence shown in Fig. 3.5(c) is $\mathcal{F}_{\text{ideal}} = 0.76$ with respect to the target state $|\Phi\rangle^+$. This is in good agreement with the measured fidelity of $\mathcal{F}_{\text{Bell}} = 0.72(3)$. We attribute the additional infidelity in the measurement to the single-qubit errors summarized in this section.

### 3.9.7. DDRF USING UDD

To see if we could improve on the selectivity of DDRF with the symmetric XY8 decoupling sequence, we use Uhrig Dynamical Decoupling[58]. In this sequence, the time between the pulses varies as

$$\delta_j = \sin^2\left(\frac{j\pi}{2N+2}\right), \tag{3.14}$$

where $j$ is the index of the interpulse delay and $N$ is the total number of pulses. The DDRF can be implemented in the same way as for an XY8 decoupling sequence. However, the phase update for the RF driving field is now different between each pulse and needs to be calculated explicitly by keeping track of the phase of the nuclear spin.

In Fig. 3.13, a spectrum similar to Fig. 3.4(c) is shown but now implemented with UDD. The top row shows UDD with $N = 4$, and the bottom row shows $N = 16$. The same two nuclear spins can be observed as with the DDRF with XY8. However, the nuclear spin bath has a different fingerprint, revealing $C_A$ better in the spectrum of $N = 4$.

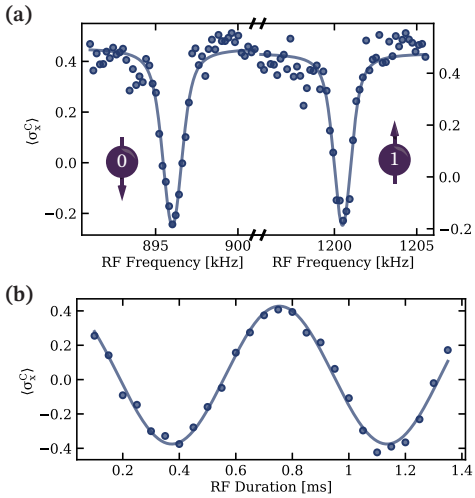


Figure 3.14: **Nuclear spin magnetic resonance and Rabi drive.** (a) Nuclear magnetic resonance experiment. The two resonance frequencies appear as a dip in the readout signal and depend on the state of the electron spin. The frequency matches well with the frequencies determined by Ramsey measurements. (b) Direct RF drive Rabi experiment. The measured Rabi frequency of 1.31(1) kHz matches the expected frequency determined by simulation.

### 3.9.8. NUCLEAR SPIN NMR AND RABI

In addition to Ramsey measurements to determine the nuclear precession frequencies, we use a direct RF drive on $C_B$ to find the two resonance frequencies. We measure the nuclear magnetic resonance (NMR) spectra by initializing the nuclear spin into state $|x\rangle$, applying the RF signal for 300 µs with varying frequency, and reading out in the $x$ basis. The resonances are shown in Fig. 3.14(a) for both electron spin states during the experiment. We determine $\omega_0/2\pi = 896.02(3)$ kHz and $\omega_1/2\pi = 1200.49(3)$ kHz.

For the tomography of the Bell state, we need to employ an $R_x(\pi/2)$ gate on the nuclear spin. We implement this gate via direct RF drive at $\omega_0$ while the electron is in state $|0\rangle$. In Fig. 3.14(b), a Rabi experiment shows a Rabi frequency $\Omega/2\pi = 1.31(1)$ kHz of the nuclear spin. From this, we calibrate the $\pi/2$ gate employed in the experiments. Furthermore, this measurement allowed us to covert the RF power used in the DDRF spectra in Figs. 3.4 and 3.13 to a Rabi frequency of $\Omega/2\pi = 1.64$ kHz, which was used in the nuclear spin bath simulations.

### 3.9.9. HYPERFINE COUPLING EXCITED STATE

In Sec. 3.7, we observe that the precession frequency of the nuclear spins depends on whether the electron spin is in the ground or excited state. The difference in precession frequency is

$$\Delta\omega_i = \omega_i^e - \omega_i^g, \tag{3.15}$$

where $\omega_i^g$ ($\omega_i^e$) is the precession frequency of the nuclear spin if the electron is in the ground (excited) state. Exciting the electron spin to the excited state with $s_i$ spin projec-

tion gives a way to measure $\Delta\omega_i$. Using Taylor expansion we can write $\omega_i$, the magnitude of Eq. (3.3), as

$$\omega_i = \omega_L \left[ 1 + \frac{s_i A_\parallel}{\omega_L} + \frac{1}{2} \left( \frac{s_i A_\perp}{\omega_L} \right)^2 \right]. \tag{3.16}$$

This allows us to write Eq. (3.15) as

$$\Delta\omega_i = s_i \left( A_\parallel^e - A_\parallel^g \right) + \frac{s_i^2}{2\omega_L} \left( A_\perp^{e\,2} - A_\perp^{g\,2} \right). \tag{3.17}$$



For our spin system with $s_0 = -1/2$ and $s_1 = 1/2$ this results in

$$A_\parallel^e - A_\parallel^g = \Delta\omega_1 - \Delta\omega_0, \tag{3.18}$$

giving us the difference in parallel hyperfine coupling between the ground and excited states. Extracting the difference in perpendicular hyperfine components is less precise as it shows up as a second-order effect in these measurements.

## REFERENCES


[1] D. D. Awschalom, R. Hanson, J. Wrachtrup and B. B. Zhou, *Quantum technologies with optically interfaced solid-state spins,* Nature Photonics **12**, 516 (2018).

[2] J. R. Maze *et al., Nanoscale magnetic sensing with an individual electronic spin in diamond,* Nature **455**, 644 (2008).

[3] M. H. Abobeih *et al., Atomic-scale imaging of a 27-nuclear-spin cluster using a quantum sensor,* Nature **576**, 411 (2019).

[4] A. J. Stolk *et al., Metropolitan-scale heralded entanglement of solid-state qubits,* Science Advances (2024), 10.1126/sciadv.adp6442.

[5] D. M. Lukin, M. A. Guidry and J. Vučković, *Integrated Quantum Photonics with Silicon Carbide: Challenges and Prospects,* PRX Quantum **1**, 020102 (2020).

[6] M. Ruf, N. H. Wan, H. Choi, D. Englund and R. Hanson, *Quantum networks based on color centers in diamond,* Journal of Applied Physics **130**, 070901 (2021).

[7] C. M. Knaut *et al., Entanglement of nanophotonic quantum memory nodes in a telecom network,* Nature **629**, 573 (2024).

[8] A. M. Dibos, M. Raha, C. M. Phenicie and J. D. Thompson, *Atomic Source of Single Photons in the Telecom Band,* Physical Review Letters **120**, 243601 (2018).

[9] A. Ruskuc, C.-J. Wu, J. Rochman, J. Choi and A. Faraon, *Nuclear spin-wave quantum register for a solid-state qubit,* Nature **602**, 408 (2022).

[10] M. T. Uysal *et al., Coherent Control of a Nuclear Spin via Interactions with a Rare-Earth Ion in the Solid State,* PRX Quantum **4**, 010323 (2023).

[11] A. Ruskuc *et al., Scalable Multipartite Entanglement of Remote Rare-earth Ion Qubits,* (2024), arXiv:2402.16224 [quant-ph] .

[12] G. D. Fuchs, V. V. Dobrovitski, D. M. Toyli, F. J. Heremans and D. D. Awschalom, *Gigahertz Dynamics of a Strongly Driven Single Quantum Spin,* Science **326**, 1520 (2009).

[13] D. J. Christle *et al., Isolated electron spins in silicon carbide with millisecond coherence times,* Nature Materials **14**, 160 (2015).

[14] D. D. Sukachev *et al., Silicon-Vacancy Spin Qubit in Diamond: A Quantum Memory Exceeding 10 ms with Single-Shot State Readout,* Physical Review Letters **119**, 223602 (2017).

[15] L. Robledo *et al., High-fidelity projective read-out of a solid-state spin quantum register,* Nature **477**, 574 (2011).

[16] J. M. Kindem *et al., Control and single-shot readout of an ion embedded in a nanophotonic cavity,* Nature **580**, 201 (2020).

[17] M. K. Bhaskar *et al.*, *Experimental demonstration of memory-enhanced quantum communication,* Nature **580**, 60 (2020).

[18] H. K. Beukers *et al.*, *Remote-Entanglement Protocols for Stationary Qubits with Photonic Interfaces,* PRX Quantum **5**, 010202 (2024).

[19] N. H. Wan *et al.*, *Large-scale integration of artificial atoms in hybrid photonic circuits,* Nature **583**, 226 (2020).

[20] M. H. Abobeih *et al.*, *Fault-tolerant operation of a logical qubit in a diamond quantum processor,* Nature **606**, 884 (2022).

[21] M. Pompili, *Multi-Node Quantum Networks with Diamond Qubits*, Ph.D. thesis, Delft University of Technology (2021).

[22] S. L. N. Hermans *et al.*, *Entangling remote qubits using the single-photon protocol: An in-depth theoretical and experimental study,* New Journal of Physics **25**, 013011 (2023).

[23] T. Van Der Sar *et al.*, *Decoherence-protected quantum gates for a hybrid solid-state spin register,* Nature **484**, 82 (2012).

[24] T. H. Taminiau *et al.*, *Detection and Control of Individual Nuclear Spins Using a Weakly Coupled Electron Spin,* Physical Review Letters **109**, 137602 (2012).

[25] C. E. Bradley *et al.*, *A Ten-Qubit Solid-State Spin Register with Quantum Memory up to One Minute,* Physical Review X **9**, 031045 (2019).

[26] J. Cramer *et al.*, *Repeated quantum error correction on a continuously encoded qubit by real-time feedback,* Nature Communications **7**, 11526 (2016).

[27] S. Maity *et al.*, *Mechanical Control of a Single Nuclear Spin,* Physical Review X **12**, 011056 (2022).

[28] C. T. Nguyen *et al.*, *Quantum Network Nodes Based on Diamond Qubits with an Efficient Nanophotonic Interface,* Physical Review Letters **123**, 183602 (2019).

[29] C. Babin *et al.*, *Fabrication and nanophotonic waveguide integration of silicon carbide colour centres with preserved spin-optical coherence,* Nature Materials **21**, 67 (2022).

[30] D. B. Higginbottom *et al.*, *Optical observation of single spins in silicon,* Nature **607**, 266 (2022).

[31] P. Inc *et al.*, *Distributed Quantum Computing in Silicon,* (2024).

[32] C. T. Nguyen *et al.*, *An integrated nanophotonic quantum register based on silicon-vacancy spins in diamond,* Physical Review B **100**, 165428 (2019).

[33] K. Senkalla, G. Genov, M. H. Metsch, P. Siyushev and F. Jelezko, *Germanium Vacancy in Diamond Quantum Memory Exceeding 20 ms,* Physical Review Letters **132**, 026901 (2024).

[34] E. I. Rosenthal *et al.*, *Microwave Spin Control of a Tin-Vacancy Qubit in Diamond,* Physical Review X **13**, 031022 (2023).

[35] P. Wang *et al.*, *Transform-Limited Photon Emission from a Lead-Vacancy Center in Diamond above 10 K,* Physical Review Letters **132**, 073601 (2024).

[36] M. Zahedian, V. Vorobyov and J. Wrachtrup, *Blueprint for efficient nuclear spin characterization with color centers,* Physical Review B **109**, 214111 (2024).

[37] S. Maity *et al.*, *Spectral Alignment of Single-Photon Emitters in Diamond using Strain Gradient,* Physical Review Applied **10**, 024050 (2018).

[38] S. D. Tchernij *et al.*, *Single-Photon-Emitting Optical Centers in Diamond Fabricated upon Sn Implantation,* ACS Photonics **4**, 2580 (2017).

[39] T. Iwasaki *et al.*, *Tin-Vacancy Quantum Emitters in Diamond,* Physical Review Letters **119**, 253601 (2017).

[40] M. E. Trusheim *et al.*, *Transform-Limited Photons From a Coherent Tin-Vacancy Spin in Diamond,* Physical Review Letters **124**, 023602 (2020).

[41] J. Görlitz *et al.*, *Spectroscopic investigations of negatively charged tin-vacancy centres in diamond,* New Journal of Physics **22**, 013048 (2020).

[42] A. E. Rugar *et al.*, *Narrow-Linewidth Tin-Vacancy Centers in a Diamond Waveguide,* ACS Photonics **7**, 2356 (2020).

[43] A. E. Rugar *et al.*, *Quantum Photonic Interface for Tin-Vacancy Centers in Diamond,* Physical Review X **11**, 031021 (2021).

[44] R. Debroux *et al.*, *Quantum Control of the Tin-Vacancy Spin Qubit in Diamond,* Physical Review X **11**, 041041 (2021).

[45] X. Guo *et al.*, *Microwave-Based Quantum Control and Coherence Protection of Tin-Vacancy Spin Qubits in a Strain-Tuned Diamond-Membrane Heterostructure,* Physical Review X **13**, 041037 (2023).

[46] M. Pasini *et al.*, *Nonlinear Quantum Photonics with a Tin-Vacancy Center Coupled to a One-Dimensional Diamond Waveguide,* Physical Review Letters **133**, 023603 (2024).

[47] J. M. Brevoord *et al.*, *Heralded initialization of charge state and optical-transition frequency of diamond tin-vacancy centers,* Physical Review Applied **21**, 054047 (2024).

[48] E. I. Rosenthal *et al.*, *Single-Shot Readout and Weak Measurement of a Tin-Vacancy Qubit in Diamond,* (2024), arXiv:2403.13110 [quant-ph] .

[49] G. De Lange, Z. H. Wang, D. Ristè, V. V. Dobrovitski and R. Hanson, *Universal Dynamical Decoupling of a Single Solid-State Spin from a Spin Bath,* Science **330**, 60 (2010).

[50] I. Karapatzakis *et al., Microwave Control of the Tin-Vacancy Spin Qubit in Diamond with a Superconducting Waveguide,* Physical Review X **14**, 031036 (2024).

[51] A. P. Nizovtsev *et al., Non-flipping$^{13}$ C spins near an NV center in diamond: Hyperfine and spatial characteristics by density functional theory simulation of the $C_{510}$ [NV]$H_{252}$ cluster,* New Journal of Physics **20**, 023022 (2018).

[52] P. Neumann *et al., Multipartite Entanglement Among Single Spins in Diamond,* Science **320**, 1326 (2008).

[53] N. Grimm *et al., Coherent Control of a Long-Lived Nuclear Memory Spin in a Germanium-Vacancy Multi-Qubit Node,* Physical Review Letters **134**, 043603 (2025), arXiv:2409.06313 [quant-ph] .

[54] S. Kolkowitz, Q. P. Unterreithmeier, S. D. Bennett and M. D. Lukin, *Sensing Distant Nuclear Spins with a Single Electron Spin,* Physical Review Letters **109**, 137601 (2012).

[55] N. Zhao *et al., Sensing single remote nuclear spins,* Nature Nanotechnology **7**, 657 (2012).

[56] M. H. M. A. Abobeih, *From Atomic-Scale Imaging to Quantum Fault-Tolerance with Spins in Diamond*, Ph.D. thesis, Delft University of Technology (2021).

[57] H. van Ommen *et al., Improved Electron-Nuclear Quantum Gates for Spin Sensing and Control,* PRX Quantum **6**, 020309 (2025).

[58] G. S. Uhrig, *Keeping a Quantum Bit Alive by Optimized π -Pulse Sequences,* Physical Review Letters **98**, 100504 (2007).

[59] R. Loudon, *The Quantum Theory of Light,* 3rd ed. (Oxford Univ. Press, Oxford, 2006).

[60] T. Astner *et al., Vanadium in silicon carbide: Telecom-ready spin centres with long relaxation lifetimes and hyperfine-resolved optical transitions,* Quantum Science and Technology **9**, 035038 (2024).

[61] J. Casanova, Z.-Y. Wang, J. F. Haase and M. B. Plenio, *Robust dynamical decoupling sequences for individual-nuclear-spin addressing,* Physical Review A **92**, 042304 (2015).

[62] P.-J. Stas *et al., Robust multi-qubit quantum network node with integrated error detection,* Science **378**, 557 (2022).

[63] I. B. W. Harris *et al., Hyperfine Spectroscopy of Isotopically Engineered Group-IV Color Centers in Diamond,* (2023), arXiv:2306.00164 [quant-ph] .

[64] H. K. Beukers *et al., Data and simulations underlying the research article 'Control of solid-state nuclear spin qubits using an electron spin-1/2',* (2025).

[65] I. T. Raa *et al., QMI - Quantum Measurement Infrastructure, a Python 3 framework for controlling laboratory equipment,* 4TU.ResearchData (2023).

[66] T. H. Taminiau, J. Cramer, T. van der Sar, V. V. Dobrovitski and R. Hanson, *Universal control and error correction in multi-qubit spin registers in diamond,* Nature Nanotechnology **9**, 171 (2014).

[67] Z.-H. Wang, G. de Lange, D. Ristè, R. Hanson and V. V. Dobrovitski, *Comparison of dynamical decoupling protocols for a nitrogen-vacancy center in diamond,* Physical Review B **85**, 155204 (2012).

[68] J. Johansson, P. Nation and F. Nori, *QuTiP: An open-source Python framework for the dynamics of open quantum systems,* Computer Physics Communications **183**, 1760 (2012).

[69] G. L. Van De Stolpe *et al.*, *Mapping a 50-spin-qubit network through correlated sensing,* Nature Communications **15**, 2006 (2024).

# 4

# TWO-PHOTON QUANTUM INTERFERENCE

*In this chapter we show two-photon quantum interference experiments with tin-vacancy centers in diamond. First, we describe how single photons are generated and measured. Then, we discuss the process of finding two tin-vacancy centers compatible to perform two-photon quantum interference. Lastly, we show the results of our two-photon quantum interference experiments with different experimental settings.*

## 4.1. GENERATION OF SINGLE PHOTONS

### 4.1.1. SETUP

Remote entanglement protocols based on spontaneous emission require a rapid excitation of one isolated optical transition of the SnV center[1]. The duration of the excitation pulse should be short compared to the optical lifetime to avoid *double excitation* events, in which a photon is emitted via spontaneous emission during the excitation pulse. As this photon is inevitably lost and not interfered, subsequent re-excitation of the SnV and emission of a photon does not lead to spin-photon entanglement and cannot be used to create remote spin-spin entanglement (see Sec. 2.5). The creation of the short optical pulse is detailed in Sec. 2.3.



The frequency of the emitted photon is not necessarily identical for different SnV centers. However, the Barrett-Kok protocol as outlined in Sec. 2.5 requires indistinguishable photons in all degrees of freedom. Due to the vanishing susceptibility of the optical transition frequency to electric fields in first order, the Stark effect cannot be used for resonance tuning SnVs like for NV centers in diamond[2,3]. The frequencies of photons stemming from different emitters can be matched by either tuning the optical transitions onto each other with magnetic field or strain tuning[4,5]. Magnetic field tuning is limited in its tuning range via the Zeeman splitting to maximally around $\frac{\delta\omega}{\delta B} \approx 2\pi \times 6\,\mathrm{GHz\,T^{-1}}$ for aligned fields in low-strain emitters[6,7]. In practice, the magnetic field influences other parameters of the SnV center like the qubit frequency, optical cyclicities and driven spin dynamics. Each of these impose restrictions on the choices of B-fields that enable entanglement experiments. For example, the dependence of the qubit frequency on the magnetic field limits the tuning range to a few hundred MHz in order to maintain well-operable MW frequencies.

To employ magnetic field tuning, two SnVs with frequencies $\omega_\mathrm{A}$ and $\omega_\mathrm{B}$ (here, $\omega_\mathrm{A} > \omega_\mathrm{B}$ without loss of generality) are Zeeman-split with a magnetic field of $B = (\omega_\mathrm{A} - \omega_\mathrm{B}) / \frac{\delta\omega}{\delta B}$. As a result, the lower energy spin-conserving transition of SnV *A* becomes resonant with the higher energy spin-conserving transition of SnV *B*. Deviations of the splitting ratios between the two emitters can be compensated by adjusting the magnetic field strength appropriately. Strain tuning can tune SnV centers for tens of GHz, but has not been implemented yet for the experiments in this work.

Alternatively, the frequency of the already emitted photon can be shifted as well. Crucially, the spin-photon entanglement needs to be conserved, so no information must be leaked to the environment. Additionally, the photons need to stay indistinguishable in all other degrees of freedom like spatial mode and polarization. Successful remote entanglement generation with frequency shifting of photons has been demonstrated with quantum frequency conversion[8,9] and side-band creation with a phase electro-optical modulator (pEOM)[9].

In this work, we implement the latter method. A continuous MW signal at the frequency difference between the input photon and its target frequency on the pEOM creates sidebands with amplitudes governed by the Bessel functions of first order. We select the first sideband with a narrow filter cavity (FWHM $\approx$ 140 MHz, transmission 80 %) that is locked to the target frequency with a PID loop. Theoretically, the first order sideband

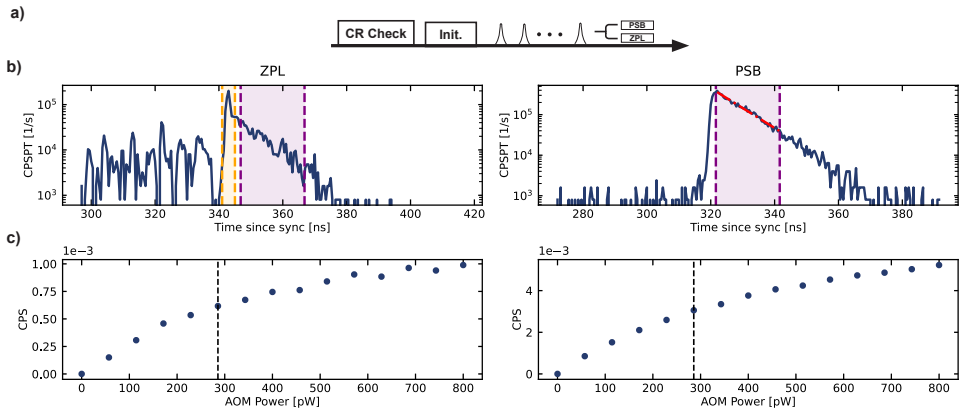


Figure 4.1: **Optical pulse measurements.** (a) Pulse sequence. A charge-resonance check (CRC) ensure that the SnV center is in the correct charge state and on resonance with the control lasers. The qubit is initialized into $|0\rangle$ during the initialization sequence by applying a laser resonant with the $B2$ transition until state $|1\rangle$ is depleted via spin-flipping. Subsequently, a train of short optical pulses resonant with the $A1$ transition is sent to the SnV center. The collected photons are spectrally separated into ZPL and PSB, and undergo additional spectral and cross-polarization filtering to reduce laser-induced photon noise before being detected by single photon detectors and timetagged referenced to a fixed synchronization pulse. (b) Timetraces of the detected photons upon short optical excitation. The ZPL (left) and PSB (right) photon count rates per shot (CPSPT) are plotted semi-logarithmically as a function of the detection time. The yellow shaded region marks the short optical pulse which is suppressed by 30 dB via cross-polarization. The ripples at earlier times in the ZPL stem from optical reflections in the setup that reach the detector earlier. The exponential decay in count rate observed in the purple shaded region are photons emitted by the SnV center. The red dashed-dotted line is an exponential fit to extract the emitter lifetime.(c) Counts per shot (CPS) for different optical pulse powers. The CPS are the integrated count rates in the purple window of (b). A saturation for increased optical pulse powers can be observed. The maximum achievable CPS for this SnV in the ZPL and PSB are around $1 \times 10^{-3}$ and $5 \times 10^{-3}$, respectively. A further increase of the optical pulse power decreases the CPS as the excitation is a coherent rotation. This effect has been observed in these measurements, but is not shown here due to power limitations in the setting of these measurements.

can contain as much as 34 % of the input signal. In our implementation, we are limited to an effective conversion fraction of around 25 % as the high MW powers required distort the wavefront and worsen the in-coupling efficiency in the collection path. Combined with all losses, including the narrow filter cavity, the shifting efficiency of a single photon is around 8 %.

### 4.1.2. MEASUREMENTS

The measurement sequence to generate single photons through spontaneous emission is shown in Fig. 4.1(a). Following a charge-resonance (CR) check[10] to ensure resonance between the laser field and the SnV center, the qubit is prepared into the bright state (labeled $|0\rangle$) by spin pumping. A train of 25 optical pulses with varying power is sent to the SnV center and the emitted light is separated into the ZPL and PSB before detection with single photon detectors as detailed in Sec. 2.3.

The timetraces of the recorded photons are shown in Fig. 4.1(b) for the ZPL and PSB respectively as *counts per shot per time*. The short optical pulse is visible in the ZPL as a

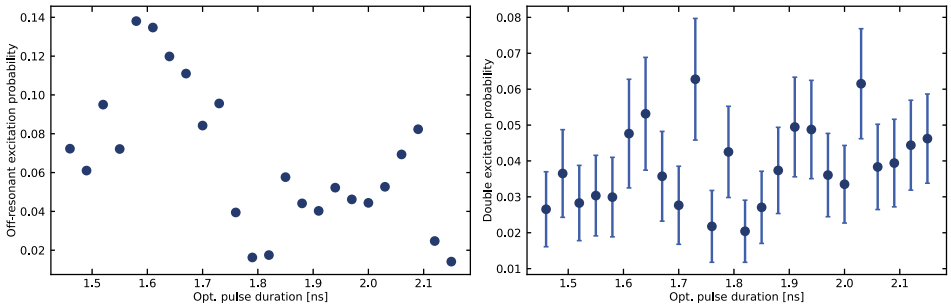


Figure 4.2: **Measurements for off-resonant and double excitation.** (a) Off-resonant excitation. Only one spin-conserving transition should be addressed by the short optical pulse. The relative probability of also exciting the unwanted transition is shown as a function of the pulse duration. The probability is dominated by the spectral density of the laser pulse. A minimum can be observed around 1.8 ns. Statistical error bars are within the data point. (b) Double excitation probability. For a finite pulse duration, the SnV can spontaneously decay during the pulse and be re-excited. The probability for this processes increases with longer pulses.



sharp peak (orange shaded region). The exponential distribution of spontaneously emitted photons from the SnV follows the excitation pulse. To guarantee a clean signal without laser background, the integration window in the ZPL starts slightly after the pulse (purple shaded region). For the PSB, no laser light is visible. The red dashed-dotted line is an exponential fit in the integration window of the PSB revealing the lifetime of the SnV to be 8.84(23) ns. This lifetime is long compared to previous measurements of SnV centers in waveguides [11,12]. We attribute this prolonged lifetime to a reduced local density of states for SnV centers close to surfaces compared to bulk diamond [13]. This behavior is expected for our devices, as the emitters are likely very close (around 50 nm) to the surface as a result of some surface-graphitization during the fabrication process which needed to be removed.

By integrating over the purple shaded regions, the *counts per shot* (CPS) are extracted which represent the probability of detecting a photon after a single short optical pulse. Changing the power of the laser pulse, a damped Rabi oscillation can be observed. As we typically want to operate the optical transition at less than a full $\pi$-rotation to minimize double excitation [1], the power limits for these measurements were chosen accordingly. The achieved CPS in the ZPL of 0.1 % are comparable to the best achieved CPS for NV centers in confocal microscopy setups [14–17]. Near-future improvements like in-contact coupling of the fiber to the waveguide and improved collection setups should enhance the collection efficiency further into the percent regime. The CPS in the PSB are higher as no cross-polarization needs to be deployed, and the photons can be collected with a multi-mode fiber as their spatial profile is not relevant for quantum network experiments.

## 4.2. OFF-RESONANT AND DOUBLE EXCITATION

Two promiment errors stemming from the photon generation step in the Barrett-Kok protocol are *off-resonant* and *double* excitation. Off-resonant excitation describes the

process where the wrong qubit state is excited due to poor selectivity of the optical pulse, whereas double excitation refers to the chance to emit a photon both during and after the optical pulse.

The spin-conserving transitions for SnV centers are degenerate at zero external magnetic field and split via the Zeeman effect due to slight differences of the $g$-factor in the ground and excited state at non-zero magnetic field. The splitting rate is highly dependent on strain and the magnetic field angle, but has been observed and simulated to be around $6\,\mathrm{GHz\,T^{-1}}$ for low-strain emitters in fields aligned to the high-symmetry axis of the defect[6,7,18]. Misaligning the field from the high-symmetry axis, the splitting rate becomes smaller. Typical splittings between the optical lines in this thesis are between 500 and 600 MHz.

When addressing one of the spin-conserving transitions with a short optical pulse of duration $t_{\mathrm{opt}}$ at frequency $\nu$, its spectral power profile $S(\omega)$ needs to be taken into account to guarantee selective drive. In the limit of a perfect rectangular pulse, the spectral density is

$$S(\omega,\nu) \propto \mathrm{sinc}^2\left(\frac{(\omega-\nu)\,t_{\mathrm{opt}}}{2}\right). \tag{4.1}$$

$S(\omega)$ is zero at a distance $\Delta\omega = \frac{2\pi}{t_{\mathrm{opt}}}$ from the center frequency $\nu$, so ideally the frequency splitting between the spin-conserving transitions should equal $\Delta\omega$. Experimentally, perfect square pulses are not realizable due to finite rise- and fall-times of modulators, so the actual optimal time duration for a pulse for a given frequency detuning might deviate. Additionally, the contrast might be not perfect as the spectral profile might not have a root at all.

In Fig. 4.2(a), the ratio of photons recorded in the PSB when preparing the qubit in state $|1\rangle$ (which should not be affected by the optical pulse) to preparing in state $|0\rangle$ (which should be addressed by the optical pulse) is shown. For the measurements, the total energy in the pulse is kept constant by inversely scaling the laser power with the pulse duration. The total rotation angle of the optical transition is roughly $\pi/2$. A clear dependence of the CPS on the pulse duration can be observed, with a minimum for a pulse duration around $t_{\mathrm{opt.}} = 1.8\,\mathrm{ns}$. The splitting between the two spin-conserving transitions for this measurement is $\Delta\omega = 2\pi\times 506\,\mathrm{MHz}$, predicting a minimum excitation probability of state $|1\rangle$ for a pulse duration of $t_{\mathrm{opt.}} = 1.98\,\mathrm{ns}$. The deviation from the actual minimum at around $t_{\mathrm{opt.}} = 1.8\,\mathrm{ns}$ can be caused by imperfect pulse shaping due to finite system-response times. An experimental optimization of $t_{\mathrm{opt.}}$ is therefore crucial to prevent off-resonant excitation errors.

*Double excitation* describes events where the emitter undergoes two excitation cycles during one optical pulse. As the drive is coherent, this can only happen through spontaneous decay. The decay happens during the optical pulse, and as subsequently the emitter is re-excited, the (potentially*) produced photon is projected into the time-window of the optical pulse. We measure the double excitation probability $p_{\mathrm{de}}$ by measuring coincidences of photon detection events during the optical pulse in the PSB with events in the detection window after the pulse in the ZPL. We use these two separate

*In principle, the decay can also happen via non-radiative channels, our definition of the collection efficiency for Eq. 4.2 covers this case.

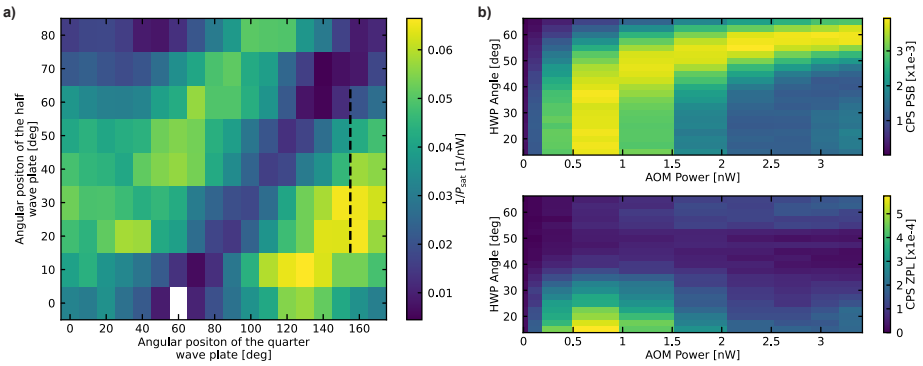


Figure 4.3: **Cross-polarization measurements.** (a) Inverse saturation power as function of excitation polarization. The excitation polarization is controlled via a set of half- and quarter waveplates (HWP/QWP). A low saturation power indicates a good alignment to the SnV dipole. (b) Optical pulse measurement with varying power along the waveplate settings following the dashed line in (a). The shape of the CPS in the ZPL and PSB differ vastly, with an expected behavior in the PSB of requiring more optical pulse power for worse alignment of the polarization, and an unexpected behavior in the ZPL with maximum CPS for good alignment with the dipole.

paths as detection events during the pulse will cause the detector to be offline during the detection window. The double excitation probability is [1]

$$p_{\mathrm{de}} = \frac{N_{\mathrm{coin}}}{(1-\mathrm{DW})\eta_{\mathrm{PSB}}(N_{\mathrm{all}} - N_{\mathrm{coin}}) + N_{\mathrm{coin}}}, \tag{4.2}$$

where $N_{\mathrm{coin}}$ are the amount of coincidence events described above, $N_{\mathrm{all}}$ are all detection events in the ZPL during the detection window, $\eta_{\mathrm{PSB}}$ is the collection efficiency of the PSB path and the Debye-Waller factor DW = 0.57 is the proportion of photons emitted into the ZPL [13]. Fig. 4.2(b) shows $p_{\mathrm{de}}$ as a function of the pulse duration. Like for panel (a), the pulse energy is kept constant and the pulse is approximately a $\pi/2$ rotation of the optical transition. A slight tendency to higher values of $p_{\mathrm{de}}$ for longer pulse durations can be observed. This is to be expected as a longer pulse increases the chance of spontaneous decay during it.

From these measurements, we find that our main metric for optimization of the optical pulse duration is the off-resonant excitation probability. To prepare for experiments, we choose an operational magnetic field, which sets $\Delta\omega$ and subsequently minimize the off-resonant excitation probability.

## 4.3. CROSS-POLARIZATION IN NANOPHOTONIC DEVICES

Usually, strong laser pulses are required for the generation of single photons from color centers. While spectral filtering can be employed for the creating of PSB photons, ZPL photons are emitted at the same frequency as the excitation pulse. To suppress the reflections of the optical pulse for entanglement generation, polarization filtering via *cross-polarization* is used. For cross-polarization, the excitation polarization is rotated with respect to the dipole orientation of the optical transition. In the collection path, a polarizer

is used to suppress the reflected laser light, cutting away some of the emitted photons as well. The usual trade-off is that a bigger misalignment of the excitation polarization with respect to the emitter dipole allows for higher collection efficiencies of the emitted photons, but requires more power for the excitation. To investigate the alignment of the polarization to the SnV dipole, we conduct a saturation measurement. Here, the power of a long laser drive tone (order of 100 µs) is swept while recording the photon count rate in the PSB. The count rate $r_{\text{ph}}$ is subsequently fitted with [19]

$$r_{\text{ph}} = A\frac{P}{2P + P_{\text{sat}}}, \tag{4.3}$$

where $P$ is the applied resonant laser power and $P_{\text{sat}}$ is the saturation power†.

Panel (b) of Fig. 4.3 shows the inverse of $P_{\text{sat}}$ as a function of the excitation polarization controlled via a half- and quarter-waveplate. At points of lower saturation power, we expect to be well aligned with the optical transition dipole. To this end, an optical pulse measurement like in Fig. 4.1 is conducted for various half-waveplate settings. In the usual picture of cross-polarization, we expect an increase in required pulse power for the maximum of CPS when misaligning from the dipole towards larger half-waveplate angles. Simultaneously, the count rate in the ZPL should increase. The upper panel in 4.3 (c) shows the expected increase in required pulse power in the PSB, and confirms that the optical transitions is fully saturated at all half-waveplate settings up to 60°. Surprisingly, the maximum CPS in the ZPL does not occur at waveplate positions where the pulse polarization is misaligned to the dipole, but at relatively aligned polarization.

A possible interpretation of this data could be that the angle between the excitation polarization and optical transition is different from the one between the reflected laser photons and the emitted photons. The origin of this difference is not clear, it could either stem from a polarization rotation on the reflection compared to the excitation polarization (e.g. by imbalanced reflection coefficients for orthogonal polarization) or by a rotation of the emitted photon polarization compared to the dipole (e.g. by imbalanced collection efficiencies for orthogonal polarization). The exact underlying mechanism remains open for further investigation.

This effect creates a desirable setting where the collection efficiency can be maximized at manageable required pulse powers. We did not investigate the exact origin of this effect as it requires detailed understanding of the polarization change caused by the tapered optical fiber tip into the waveguide. We suspect some non-unitary operations like partial polarization due to unbalanced transfer of the different polarizations.

## 4.4. MATCHMAKING

For quantum networking experiments, more than one emitter needs to be used simultaneously. Crucially, the properties of the emitted photons need to be identical to be able to interfere them, which is needed for two-photon quantum interference and entanglement generation (see Chap. 2). Usually, it is straight-forward to match the spatial mode and polarization of the photons as they can be easily controlled after emission.

†Mind, that this is not the only definition of $P_{\text{sat}}$. Often, it is also defined such that the count rate is $\frac{2}{3}A$ at saturation power, see e.g. Section 2.4 of Ref. [20]

Table 4.1: **Statistics from the search for pairs of emitters.** The two searches differ in their definition of a "usable SnV", details are provided in the main text.*: Not all pairs were investigated for their MW properties.

| | 1st search | | 2nd search | |
|---|---|---|---|---|
| | Alice | Bob | Alice | Bob |
| # of measured waveguides | 12 | 28 | 23 | 32 |
| # of usable SnVs | 18 | 26 | 15 | 9 |
| # of pairs (no MW constraints) | 16 | | 24 | |
| # of pairs (MW constraints) | 1* | | 4 | |



The temporal shape is governed by the lifetime and is harder to control without altering the local density of states via material engineering and nano-fabrication, but in similar environments, the photons from emitters of the same species usually have similar lifetimes. For solid state emitters like the SnV, the frequency spectrum of the photon poses the biggest challenge. For spontaneously emitted photons, it takes a Lorentzian shape. To match the photons, the center of the distribution should be identical, and both distributions should be lifetime-limited to avoid leakage of information of the photon to the environment.

In preparation for experiments with two SnVs, we conduct a search to find pairs of emitters that are close enough in frequency such that we can tune their photons onto the same frequency. We use the setup as described in Sec. 2.3, and call one side of the setup *Alice* and the other side *Bob*. In the following sections, we employ frequency tuning via magnetic field strength and sideband-shifting. These methods are limited to a maximum frequency shift of roughly 5 GHz due to available hardware. In future devices, this constraint will either be lifted by tuning the strain locally to change the emission frequency or via quantum frequency conversion, where a broad band of photons can be converted to the same frequency.

In our case, we conduct two searches for pairs of emitters. With the pair we select in the first search, the experiments in Sec. 4.5.1 are performed. After these experiments, a break-down of the setup, in which the superconducting magnet quenched, requires several temperature cycles and rewiring. For one emitter of the pair, the strain- or electric environment changed so significantly, that we were not able to continue working with this pair. The second search thereafter leads to the experiments in Sec. 4.5.3 and 4.5.2.

Table 4.1 summarizes the findings of the searches qualitatively. The findings are not fully comparable: during the second search, emitters were already selected on their MW qualities while for the first search, only optical properties were initially investigated. Therefore, less promising emitters were found in the second search, especially on Bob's side. We suspect a poorer microwave delivery there, likely caused by a bigger distance between the bondwire and the emitters.

Another significant difference between the searches is the investigated frequency regime. In the first search, a frequency range of 40 GHz around the center of the inhomogeneous distribution (full width at half maximum on the order of 100 GHz) was investigated. During the second search, the investigated range was red-shifted from the center of the inhomogeneous distribution by around 70 GHz. The reason for this is that we noticed during the first search, that emitters close to the center of the inhomoge-

neous distribution seemed to have little to no transversal strain, which makes MW driving less efficient. We suspect emitters further away from the center of the distribution to experience more strain, and hence enhance the MW drivability. As a consequence, we find fewer emitters within the investigated frequency window.

The searches also differ in the way the pairs are formed. For the first search, only magnetic field tuning was planned to tune the SnVs onto resonance. To allow for spin-selective optical pulses, we constrained the frequency difference to a minimum fo 600 MHz. On the other hand, a reasonably small magnetic field is required to keep the qubit frequency in an operable regime of less than 6 GHz, which limits the allowed frequency difference to around 1.2 GHz. When forming pairs in the second search, this upper limit of the frequency difference was increased to 5 GHz as photon frequency shifting was accessible for the experiments.



## 4.5. TWO-PHOTON QUANTUM INTERFERENCE

We report on three separate two-photon quantum interference (TPQI) experiments in this section. For the first experiment, a shared optical pulse is used. In this scenario, we do not have the means to create a distinguishable case and extract the visibility from Eq. 2.13, but need to involve more mathematical methods. The emitters are tuned onto resonance via magnetic field tuning.

The other two experimental runs are conducted with a different pair of emitters and two individual laser pulses, so we can create a distinguishable scenario by delaying one of the pulses significantly. The experiments differ in the way the emitters are tuned onto resonance: for the first, the photon frequency of one of the emitters is shifted after emission with a phase EOM while for the second, magnetic field tuning is used.

### 4.5.1. TPQI WITH SHARED PULSE

The data for the first experiment is taken with two SnV centers that share the same crystallographic orientation in nanophotonic waveguides. Their optical transitions are tuned onto resonance via magnetic field tuning at 830 mT aligned field. First, we verify that the emitted photons truly are single photons by performing a second-order intensity autocorrelation measurement. The measurement is performed in a binned fashion by performing 100 subsequent optical pulses after initializing the qubit into the bright state and routing the ZPL photons to a balanced beamsplitter. Upon detection, the photons are labeled with their respective excitation bin. The discrete autocorrelation function $g^{(2)}(m)$ is defined as

$$g^{(2)}(m) = \sum_k \frac{\langle n_k n_{k+m} \rangle}{\langle n_k \rangle \langle n_{k+m} \rangle}, \tag{4.4}$$

where the $\langle n_k \rangle$ is the amount of recorded photons bin $k$, $m$ is the bin difference, and the numerator describes the coincidence counts between bin $k$ and $k+m$. Fig. 4.4(a) shows the measured $g^{(2)}(m)$ for $|m|$ up to 9 normalized to the average value of the non-zero bin differences. The value of $g^{(2)}(0) = 0.06(4)$ is a clear signature of single photon emission.

To systematically record $g^{(2)}(0)$ during the two-photon quantum interference experiment, the measurement is interleaved with $g^{(2)}$ measurements for both emitters. The

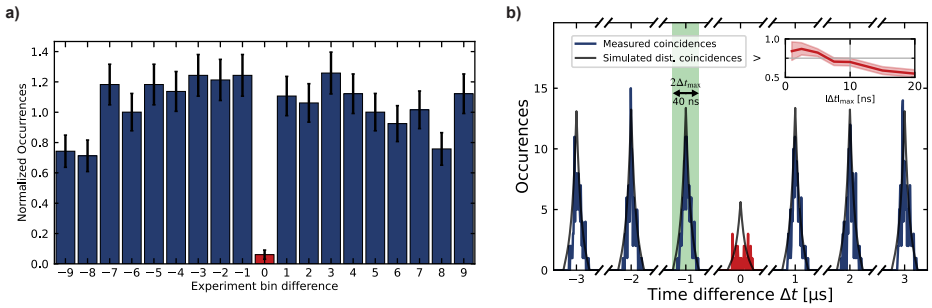


Figure 4.4: **Two-photon quantum interference experiment with aligned SnVs.** (a) Single photon purity measurement via $g^2$ experiment. Coincidences of ZPL photons are recorded as function of excitation bin difference. The coincidences are normalized to the mean of non-zero bin difference. The low value of $g^2(0)$ is proof for a high single-photon purity. (b) TPQI experiment. The ZPL photons of two SnVs are interfered at a beamsplitter and the coincidences at the output port are recorded as a function of detection time difference. For coincidences stemming from different rounds of excitation, a double-exponential envelope is observed. The black lines describe the expected coincidences from the emitter lifetimes and CPS for fully distinguishable photons. Coincidences from the same round of excitation should be suppressed, and take a different shape. The difference in measured coincidences from the expectation value for fully distinguishable photons reveals the visibility.



data in the run leads to $g^{(2)}(0) = 0.07(5)$ and $g^{(2)}(0) = 0.0$ for the two SnV centers, where the latter value is probably due to a very small $g^{(2)}(0)$ and the premature abort of the measurement because of a cryostat failure.

The data of the TPQI experiment is shown in Fig. 4.4(b). The experimental sequence is the same as for the $g^{(2)}$ measurement, only that this time the optical pulse is routed to both emitters and the arrival time of the photons at the beamsplitter is matched. In addition to the $g^{(2)}$ data, the data is resolved in bins of 800 ps to show the arrival time differences of the photons for each coincidence. The coincidence distribution for non-zero bin differences follows a double-exponential given by the photon wavefunctions. The expected coincidence probability distribution is simulated (see Ref.[21]) from the known single photon detection probabilities and properties. As no distinguishable measurement can be conducted easily in this configuration, Eq. 2.13 has to be slightly modified to extract the visibility $V$ as

$$V = 1 - \frac{N_{\text{coinc}}}{N P^{\text{dist}}_{\text{coinc}}}, \tag{4.5}$$

where $N_{\text{coinc}}$ is the count of measured coincidences with zero bin difference for $N$ repetitions and $P^{\text{dist}}_{\text{coinc}} = p_{A\to1}p_{B\to2} + p_{A\to2}p_{B\to1}$ is the extrapolated coincidence probability of two photons stemming from emitters $A$ and $B$ based on their photon detection probabilities $p$ in detector 1 and 2.

Eq. 4.5 results in a measured visibility of $V = 0.55(5)$ when including the total integration window. The structure of the detection time difference distribution in the zero bin however allows for additional filtering by limiting the accepted detection time difference $|\Delta\ t|_{\text{max}}$. The inset in Fig. 4.4 show the visibility increasing when reducing $|\Delta\ t|_{\text{max}}$ up to $V = 0.84(12)$ at the cost of higher uncertainty due to reduced data. The increase

in visibility for smaller $|\Delta\ t|_{\max}$ is a consistent with the presence of spectral diffusion as discussed in Sec. 2.4.2.

### 4.5.2. TPQI WITH FREQUENCY SHIFTING

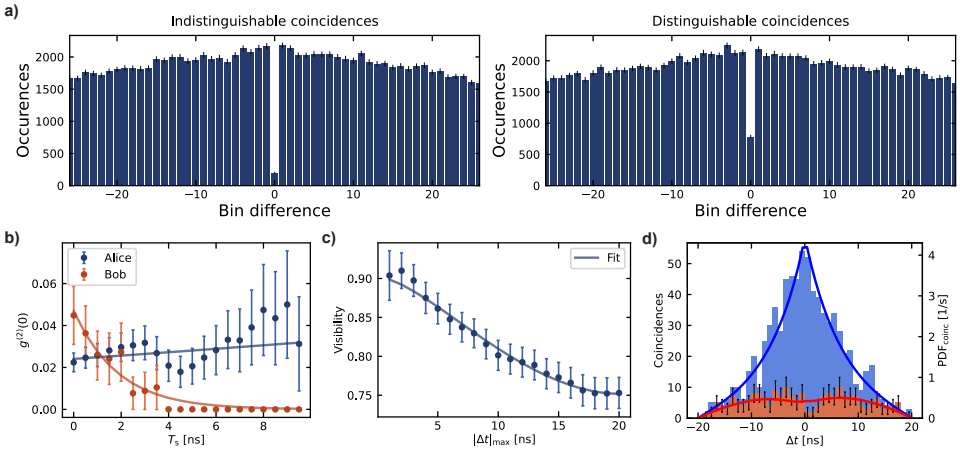


Figure 4.5: **Two photon quantum interference with independent pulses and photon shifting.** (a) Histogram of coincidence events as function of excitation pulse difference. The two histograms are taken for an indistinguishable setting, where the photons overlap in all degrees of freedom, and a distinguishable scenario, where they are shifted with respect to each other in time. The reduced coincidences in the zero difference bin for the indistinguishable case is the signature of the Hong-Ou Mandel effect. (b) $g^{(2)}(0)$ as a function of the detection window start. The noise contribution is modeled as an exponential source for both emitters individually. (c) Detection time difference filtering. The fit model reveals the total linewidth broadening, details in the main text. (d) Detection time difference resolved coincidences in the zero bin. The probability distribution resulting from the fit is overlaid.

For the second experimental run for the TPQI experiment, the optical pulse stems from two separate lasers, allowing for the creation of a distinguishable scenario, where one of the photons is delayed by roughly 40 lifetimes. The SnV centers used for this experiment have different orientations in the crystal lattice, requiring a misaligned field for at least one emitter. As the two emitters are detuned by 3.5 GHz, we employ frequency shifting on the photons of one of the emitters with the method detailed in sec. 4.1.1.

Fig. 4.5(a) shows the coincidences for the indistinguishable and distinguishable scenario. Compared to the experimental sequence in Sec. 4.5.1, the train of optical excitations after the qubit initialization contains only $N = 150$ pulses due to the limited cyclicity. Therefore, a characteristic pyramid shape can be seen in the number of coincidences as a function of the excitation bin difference stemming from the possible combinations to achieve the bin difference[22]. We only show the data up to an excitation bin difference of 25 for readability. The zero bin in the distinguishable case is expected to be reduced by a factor $\frac{N}{2(N-1)}$ compared to the first bin as it does not contain coincidences from two photons emitted by the same SnV center.

A clear reduction of the measured coincidences in the zero bin is observed in the indistinguishable scenario, whereas the other bins match the distinguishable case. The

extracted visibility via Eq. 2.13 is $V = 0.64(5)$ but increases up to $V = 0.84(8)$ by additionally filtering the on $|\Delta t|_{\max}$ to 5 ns as shown in Fig. 4.5(b).

We extract the individual photon detection probabilities for both emitters from the distinguishable case and find $p_A = 4.6(2) \times 10^{-4}$ and $p_B = 2.3(1) \times 10^{-4}$. We limit $p_A$ to roughly $2p_B$ artificially to avoid massive influences from noise sources on Alice's side. The non-zero $g^{(2)}$ value as a function of the detection window start $T_s$ in Fig. 4.5(b) is modeled as an independent shot noise source (e.g. laser, other emitters) with an exponential probability. The resulting auto-correlation function can be written as

$$g^{(2)}(T_s) = \frac{2p_s(T_s)p_n(T_s) + g_n^{(2)} p_n^2(T_s)}{\left(p_s(T_s) + p_n(T_s)\right)^2}, \tag{4.6}$$



where $p_s(T_s)$ ($p_n(T_s)$) is the probability to detect a signal (noise) photon in the detection window with starting time $T_s$, respectively, and $g_n^{(2)}$ is the autocorrelation function for the noise source. In the case of laser noise, the autocorrelation would take the value $g_n^{(2)} = 1$, for a single second emitter $g_n^{(2)} = 0$. If the background noise is caused by a multitude of other emitters, the $g_n^{(2)}$ approaches 1 as well. For our analysis, we assume an autocorrelation of $g_n^{(2)} = 1$ for the noise.

From Eq. 4.6, we extract a noise source with $p_n^A = 5.6(4) \times 10^{-6}$ and $\tau_n^A = 11(3)$ ns for Alice and $p_n^B = 5.6(4) \times 10^{-6}$ and $\tau_n^B = 1.4(1)$ ns for Bob. The noise source for Alice is unknown, whereas the source on Bob is laser photons delayed by the narrow filter cavity used in the frequency shifting setup, which is expected to have a lifetime of around 1.4 ns.

Having the photons profiles for signal and noise fixed on both sides, we can fit the visibility as a function of the maximum detection time difference with the combined pure dephasing and spectral diffusion as free parameters according to Eq. 2.26. The fit in Fig. 4.5(c) results in a combined pure dephasing rate $\Gamma^* = 19(2)$ MHz and a combined spectral diffusion with full width at half maximum $\Sigma/2\sqrt{2\ln 2} = 27(2)$ MHz It is important to note that the correlation between $\Gamma^*$ and $\Sigma$ in the fit result is $-0.98$, revealing that the model cannot accurately differentiate the contributions of both noise sources for our data. The linewidth results match the linewidth we typically measure with photoluminescence frequency scans. The fit describes the data well, but seems to underestimate the visibility for small $|\Delta t|_{\max}$.

In Fig. 4.5(d) we overlay the measured zero bin coincidences with the probability distribution profile from the fit. The data shows less coincidences close to $\Delta t_{\max} = 0$, matching the observation that the fit does not describe the data very accurately here. This could however be a statistical effect as the number of coincidences per bin is single digits. A more accurate analysis would require more data.

The model derived in Sec. 2.4.2 assumes a single-photon noise statistic. The noise contribution on Bob likely stems from a classical laser field leaking out of the filter cavity. Hence, a treatment as a coherent state would be required. However, as the measured noise detection probability is on the order of $10^{-6}$, the weak coherent state is described by its eigenvalue $\alpha \propto \sqrt{10^{-6}}$. This results in a negligible contribution of the $|2\rangle$-photon number state and it is appropriate to model the field as a single photon.

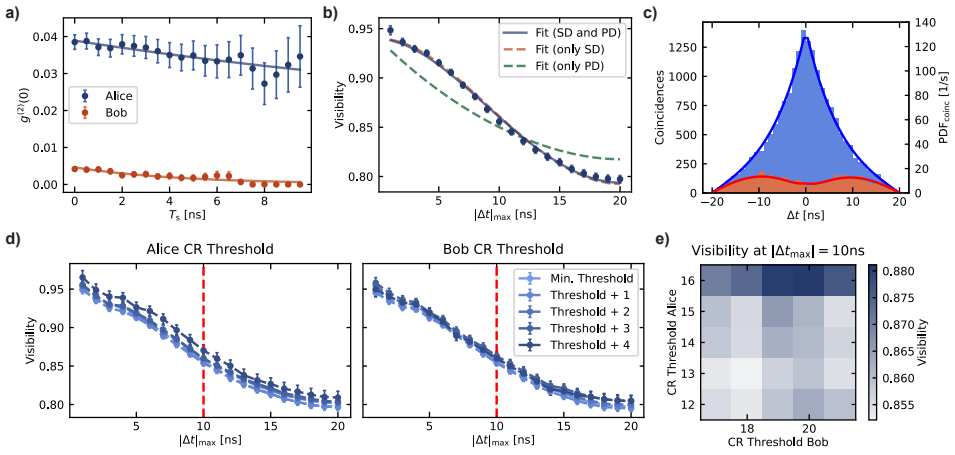


Figure 4.6: **TPQI measurements with magnetic field tuning.** (a) $g^{(2)}(0)$ as a function of the detection window start. In contrast to Fig. 4.5, no filter cavity is employed at Bob. The noise contribution is modeled as an exponential source for both emitters. (b) Visibility as a function of maximum detection time difference. The data cannot be fitted well by only employing spectral diffusion (SD) or pure dephasing (PD), but requires a combination of both. (c) Detection time difference resolved coincidences in the zero bin. The data is overlaid with the predicted probability distribution from the fit model and matches well. (d) Spectral diffusion mitigation by stricter post-selected resonance checking. Increasing the threshold heralding resonance of the emitter to the laser on Alice improves the visibility, hinting towards remaining SD with the data acquisition parameters. On Bob, this improvement is less pronounced. Red dashed line indicates the cut used for panel (e). (e) Visibility at $|\Delta t|_{\max}$ as function of resonance threshold. Stricter thresholding improves the visibility slightly at the cost of data acquisition rate.

### 4.5.3. TPQI WITH MAGNETIC FIELD TUNING

After the experiment in sec. 4.5.2, we perform a full thermal cycle of the cryostat with the goal to improve the microwave delivery as well as installing a temperature sensor closer to the device. We deemed this necessary to be able to proceed with longer experiments including microwave control towards the goal of spin-spin entanglement. After the thermal cycle, we conduct another TPQI experiment with the same emitters. This time, the resonances of the emitters are close enough together to employ magnetic field tuning and overlapping two spin-conserving transitions. We attribute this change in resonance frequency of a few GHz to a slightly different local strain- or electrostatic environment. The experiment is conducted at a different magnetic field to ensure overlap of the resonance transitions. This magnetic field has a magnitude of $B = 117\,\mathrm{mT}$ and is misaligned by 20 deg (70 deg) with Alice (Bob), respectively. The cyclicities of both emitters at this field are around 700 and 350, respectively. We observe small diffusion of the resonances over long timescales (days to weeks) which do not exceed the inhomogeneous resonance distributions of the emitters attainable by changing the charge environment with a green laser. Hence, we do not have to adjust the magnetic field but rather rely on the CR check to ensure resonance.

Fig. 4.6(a-c) show the fit results to the same model as detailed in Sec. 4.5.2. Avoiding the losses of the frequency shifting board (and hence removing the restriction for Alice)

improves our detection probabilities to $p_A = 1.8(1) \times 10^{-3}$ and $p_B = 1.9(1) \times 10^{-3}$. The noise contributions have detection probabilities of $p_n^A = 3.6(1) \times 10^{-5}$ and $p_n^B = 4.1(3) \times 10^{-6}$ with decay constants $\tau_n^A = 6.2(1)$ ns and $\tau_n^B = 2.8(2)$ ns. This differs significantly from the experiment in Sec. 4.5.2. For Alice, the decay constant of the noise source could be attributed to another SnV center in the vicinity. At the time of the writing, we do not have a definitive explanation for where this $g^2$ behavior originates from and whether the thermal cycle and change in magnetic field could explain this behavioral difference on Alice's side. For Bob, the $g^{(2)}(0)$ does not show the quick exponential decay any longer, confirming the hypothesis that this was indeed caused by the filtering cavity.

The visibility as a function of $|\Delta t|_{max}$ in Fig. 4.6(b) qualitatively matches the data in Fig. 4.5(d), indicating a good repeatability and stability of the emitter quality in regard of thermal cycles and different operation conditions. Due to the higher photon detection probability, the data quality allows for better fits, differentiating the influence of spectral diffusion (SD) and pure dephasing (PD). The solid fit to the data has the combined SD and combined PD of both emitters as free parameters, whereas the dashed lines show the best fit when discarding one of the effects, respectively. We observe a dominance of the spectral diffusion contribution, resulting in $\Sigma/2\sqrt{2\ln 2} = 33.0(7)$ MHz and $\Gamma^* = 2(1)$ MHz. As previously, the SD and PD are anti-correlated parameters with a correlation of $-0.97$, confirming the difficulty to differentiate the exact origin of the linewidth broadening in the model. The fit matches the data well but seems to not capture the behavior of the data fully, indicating the necessity for a more complex model in the future. In panel (c), we show the predicted coincidence probability in the zero bin of the TPQI experiment as a function of detection time difference. The shape of the recorded coincidence events matches the prediction well.

As SD seems to still be present despite live-conditioning the experiment on resonance between the laser and emitters, we investigate whether stricter conditioning impacts the visibility in Fig. 4.6(d-e). In panel (d), we show the impact of increasing the threshold condition of Alice (Bob) in post-selection on the visibility in the left (right) panel. While little improvement is observable for stricter thresholds on Bob, we find some improvement when increasing Alice's threshold. The effect is however relatively small, improving the visibility by less than 2% at $|\Delta t|_{max} = 10$ ns. Panel (e) shows the visibility at $|\Delta t|_{max} = 10$ ns for combinations of stricter thresholding on both emitters, confirming a bigger improvement for stricter thresholds on Alice.

A possible reason why stricter thresholds do not significantly reduce the SD might be the timescale of the effect: In experiments presented, we perform 3 blocks of 100 optical pulses interleaved with a spin-pumping sequence on the emitters per successful resonance check. Spectral diffusion throughout this sequence cannot be mitigated by thresholding before the experiment.

### 4.5.4. DISCUSSION OF TPQI

In this section, we presented two-photon quantum interference experiments with two different pairs of SnV centers. Compared to prior TPQI experiments with SnV centers, where the centers were excited off-resonantly at zero magnetic field[23], our experiments are directly compatible with remote entanglement generation protocols. In the first scenario, the two SnV centers are aligned to the same crystallographic axis, which allows

for an operation at aligned magnetic field, yielding higher cyclicities at the cost of slower initialization. Both SnVs are excited with he same optical pulse that is split in two. Therefore, no distinguishable scenario can be created easily. The raw visibility for a detection window of 20 ns, roughly 2-3 lifetimes of the emitters, is $V = 0.55(5)$. The arrival time-resolved $\Delta t$ coincidence distribution shows clear signs of spectral diffusion[21,24,25]. Upon filtering of this quantity, a visibility of $V = 0.84(12)$ is observed. This visibility is comparable to earlier reports with the nitrogen- and silicon-vacancy center in diamond[26,27] as well as current results with frequency converted photons from nitrogen-vacancy centers[22], but slightly worse than the interference visibility of optimized nitrogen-vacancy centers without conversion[15]. Spectral diffusion likely limits the visibility, as it causes more coincidences than expected when increasing the arrival time difference. Additionally, pure dephasing can cause coincidences independent of $\Delta t$. Both of these effects can be caused by unstable charge environments, for example from implantation-induced damage or surface charges. For future experiments, improving the visibility is key to enhance the achievable entanglement fidelity for remote entanglement protocols based on photon emission.



The second and third experiment are conducted with a pair of SnVs whose symmetry axes are not aligned with respect to each other. The magnetic field is hence misaligned for both emitters, leading to cyclicities in the low hundreds. In the first setting, one of the emitted photon is shifted onto the same frequency as the other photon after emission, in the second run the emitters are tuned onto resonance with each other via the magnetic field strength. For this experiment, the optical pulses for the two emitters are generated independently, which allows for the creation of fully distinguishable photons. The dependence of visibility on the detection time difference of the photons indicates a limitation by spectral diffusion. The raw visibility for a 20 ns detection window is $V = 0.75(2)$ ($V = 0.79(1)$), which improves to $V = 0.80(2)$ ($V = 0.85(1)$) for two separate experiments respectively. The raw and time-filtered extracted visibilities as well as the overall behavior of the visibility for different detection time differences from these two experiments are comparable, emphasizing the repeatability of high-quality photon interference between SnV centers. As these measurements were separated by a few months, this gives confidence that the performance of the emitters is stable over long periods of time.

## REFERENCES

[1] S. L. N. Hermans *et al.*, *Entangling remote qubits using the single-photon protocol: An in-depth theoretical and experimental study,* New Journal of Physics **25**, 013011 (2023).

[2] Ph. Tamarat *et al.*, *Stark Shift Control of Single Optical Centers in Diamond,* Physical Review Letters **97**, 083002 (2006).

[3] L. De Santis, M. Trusheim, K. Chen and D. Englund, *Investigation of the Stark Effect on a Centrosymmetric Quantum Emitter in Diamond,* Physical Review Letters **127**, 147402 (2021).

[4] S. Meesala *et al.*, *Strain engineering of the silicon-vacancy center in diamond,* Physical Review B **97**, 205444 (2018).

[5] J. M. Brevoord *et al.*, *Large-range tuning and stabilization of the optical transition of diamond tin-vacancy centers by in situ strain control,* Applied Physics Letters **126** (2025), 10.1063/5.0251211.

[6] E. I. Rosenthal *et al.*, *Microwave Spin Control of a Tin-Vacancy Qubit in Diamond,* Physical Review X **13**, 031022 (2023).

[7] H. K. C. Beukers *et al.*, *Control of Solid-State Nuclear Spin Qubits Using an Electron Spin- 1 / 2,* Physical Review X **15**, 021011 (2025).

[8] A. J. Stolk *et al.*, *Metropolitan-scale heralded entanglement of solid-state qubits,* Science Advances (2024), 10.1126/sciadv.adp6442.

[9] C. M. Knaut *et al.*, *Entanglement of nanophotonic quantum memory nodes in a telecom network,* Nature **629**, 573 (2024).

[10] J. M. Brevoord *et al.*, *Heralded initialization of charge state and optical-transition frequency of diamond tin-vacancy centers,* Physical Review Applied **21**, 054047 (2024).

[11] J. Arjona Martínez *et al.*, *Photonic Indistinguishability of the Tin-Vacancy Center in Nanostructured Diamond,* Physical Review Letters **129**, 173603 (2022).

[12] M. Pasini *et al.*, *Nonlinear Quantum Photonics with a Tin-Vacancy Center Coupled to a One-Dimensional Diamond Waveguide,* Physical Review Letters **133**, 023603 (2024).

[13] J. Görlitz *et al.*, *Spectroscopic investigations of negatively charged tin-vacancy centres in diamond,* New Journal of Physics **22**, 013048 (2020).

[14] B. Hensen *et al.*, *Loophole-free Bell inequality violation using electron spins separated by 1.3 kilometres,* Nature **526**, 682 (2015).

[15] P. C. Humphreys *et al.*, *Deterministic delivery of remote entanglement on a quantum network,* Nature **558**, 268 (2018).

[16] M. Pompili *et al.*, *Realization of a multinode quantum network of remote solid-state qubits,* Science **372**, 259 (2021).

[17] S. L. N. Hermans *et al.*, *Qubit teleportation between non-neighbouring nodes in a quantum network,* Nature **605**, 663 (2022).

[18] I. Karapatzakis *et al.*, *Microwave Control of the Tin-Vacancy Spin Qubit in Diamond with a Superconducting Waveguide,* Physical Review X **14**, 031036 (2024).

[19] R. Loudon, *The Quantum Theory of Light,* 3rd ed. (Oxford Univ. Press, Oxford, 2006).

[20] A. M. Stramma, *The Tin-Vacancy Centre in Diamond: A Coherent Spin-Photon Interface for Quantum Network Nodes*, Ph.D. thesis, University of Cambridge (2024).

[21] T. Dolné, *Demonstration of Two-Photon Quantum Interference with Two Tin-Vacancy Centers in Diamond*, Master's thesis, Delft University of Technology (2024).

[22] A. Stolk *et al.*, *Telecom-Band Quantum Interference of Frequency-Converted Photons from Remote Detuned NV Centers,* PRX Quantum **3**, 020359 (2022).

[23] V. Bushmakin *et al.*, *Two-Photon Interference of Photons from Remote Tin-Vacancy Centers in Diamond,* (2024), arXiv:2412.17539 [quant-ph] .

[24] T. Legero, T. Wilk, A. Kuhn and G. Rempe, *Time-resolved two-photon quantum interference,* Applied Physics B **77**, 797 (2003).

[25] F. W. Sun and C. W. Wong, *Indistinguishability of Independent Single Photons,* Physical Review A **79**, 013824 (2009).

[26] H. Bernien *et al.*, *Heralded entanglement between solid-state qubits separated by three metres,* Nature **497**, 86 (2013).

[27] A. Sipahigil *et al.*, *Indistinguishable Photons from Separated Silicon-Vacancy Centers in Diamond,* Physical Review Letters **113**, 113602 (2014).

# 5

# Heralded Entanglement Generation between Tin-Vacancy Centers in Diamond Waveguides

*In this chapter we show spin-photon and spin-spin correlation measurements. We describe the additions to the setup for these measurements, explain the experimental sequence and present an analytical model to simulate the achievable entanglement fidelity in our infrastructure. We report the outcomes of spin-photon correlation measurements of two individual tin-vacancy centers as well as measurements of their joint state after creating heralded entanglement between them.*

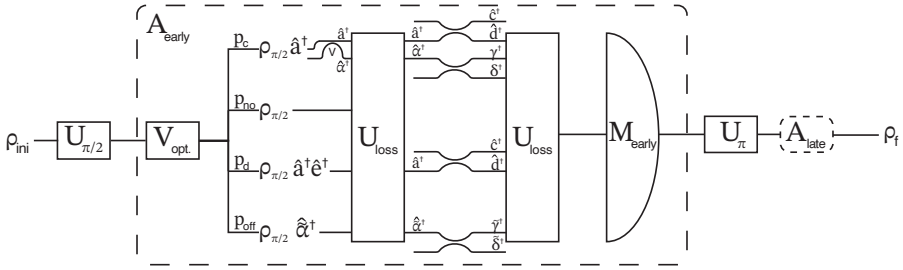


Figure 5.1: **Error model for the Barrett-Kok protocol.** The different steps performed on a single qubit during the protocol as well as the photonic modes involved are presented. A detailed description of all steps can be found in the main text.

## 5.1. STEP-BY-STEP DERIVATION OF THE BARRETT-KOK MODEL INCLUDING ERRORS



In real-life experiments, all of the many steps involved in the Barrett-Kok protocol[1] are subject to errors. In this section, we present an analytical model treating these errors and derive an expression for the success probability and fidelity. Naturally, we cannot account for all errors but mainly select the error sources most prominent in our system. The flow of the protocol for one of the qubits in a schematic circuit-diagram is depicted in Fig. 5.1. The qubit start out in a mixed state $\rho_{\mathrm{m}}$ and is prepared into an eigenstate $\rho_{\mathrm{ini}} = |0\rangle\langle 0|$ with error probability $p_{\mathrm{ini}}$ to actually create the orthogonal eigenstate $|1\rangle\langle 1|$. Afterwards, applying a $\pi/2$-gate with error probability $p_{\pi/2}$ creates an equal superposition state.

Then, an optical pulse excites the qubit and possibly creates a photon. We consider four scenarios: In the error-free case with probability $p_{\mathrm{c}}$, a coherent single photon $\hat{a}^\dagger$ is created from the $|0\rangle$-part of the superposition. To account for finite Hong-Ou-Mandel (HOM) visibility of the photons, it is split into two modes, where the indistinguishable mode $\hat{a}^\dagger$ will later interfere with mode $\hat{b}^\dagger$ from the other qubit and the distinguishable mode $\hat{\alpha}^\dagger$ does not interfere with the photon from the other qubit. Secondly, with probability $p_{\mathrm{no-exc}}$, the superposition state is not excited (as we do not necessarily apply a full $\pi$-rotation on the optical transition) and remains is not connected to a photonic mode. The last two cases cover double excitation, where a second mode $\hat{e}^\dagger$ is populated and later traced out; and off-resonant excitation, where the photon stems from the $|1\rangle$-part of the superposition is considered incoherent. More details on the exact implementation of this optical pulse will be discussed in Sec. 5.1.2.

All photonic channels are then subject to loss before entering the HOM beamsplitter. Here, only the indistinguishable modes $\hat{a}^\dagger$ and $\hat{b}^\dagger$ from both qubits are interfered with each other, all distinguishable modes from both qubits get treated with separate beamsplitter modes. Another loss channel is followed by a measurement of the photons. This concludes the early timebin. After a $\pi$-rotation on the qubits, a second round of optical excitation, interference and detection takes place. Finally, the two-qubit state $\rho_{\mathrm{f}}$ is obtained.

In the following analysis, we explain the steps of the protocol for qubit $A$ unless mentioned otherwise, qubit $B$ is treated equivalently by substituting the corresponding photonic operators and variables.

### 5.1.1. QUBIT INITIALIZATION AND PREPARATION OF SUPERPOSITION

Before the protocol, both qubits start out in a mixed state. We prepare them into a superposition in two steps. First, an initialization sequence maps both qubits into state $|0\rangle$, after which a MW $\pi/2$-pulse generates a superposition state $|x\rangle = \frac{1}{\sqrt{2}}(|0\rangle + |1\rangle)$. We model the error of the spinpump as a chance of $p_{\text{ini}}$ to prepare the orthogonal state $|1\rangle$, resulting in an initial density matrix

$$\rho_{\text{ini}} = \left(1 - p_{\text{ini}}\right)|0\rangle\langle 0| + p_{\text{ini}}\,|1\rangle\langle 1|\,. \tag{5.1}$$

The $\pi/2$-pulse error is modeled via a fully depolarizing channel[2] via

$$\rho_{\pi/2} = \left(1 - p_{\pi/2}\right) U_{\pi/2}\rho_{\text{ini}}U_{\pi/2}^{\dagger} + p_{\pi/2}\frac{I}{2}, \tag{5.2}$$

where $U_{\pi/2}$ is the unitary describing the qubit rotation and $I$ is the single-qubit identity matrix. Under consideration of all possible combinations of errors to occur, the initial state for either qubit $Q \in \{A, B\}$ is

$$\rho_{\text{ini}}^{Q} = \left(1 - p_{\pi/2}^{Q}\right)\left((1 - p_{\text{ini}}^{Q})\,|x\rangle\langle x| + p_{\text{ini}}^{Q}|-x\rangle\langle -x|\right) + \frac{1}{2}p_{\pi/2}^{Q}\left(|0\rangle\langle 0| + |1\rangle\langle 1|\right). \tag{5.3}$$

### 5.1.2. EARLY TIMEBIN - OPTICAL PULSE

The optical pulse has various ways in which it can cause errors in the protocol. We model the optical excitation as an isometry $V$ that extends the Hilbert space of the qubit to also include photon modes via

$$V : \mathcal{H}_{\text{qubit}} \rightarrow \mathcal{H}_{\text{qubit}} \otimes \mathcal{H}_{\text{photon}} \tag{5.4}$$

$$V = |0\rangle\langle 0| \otimes \left(\sqrt{q}(A\hat{a}^{\dagger} + \bar{A}\hat{\alpha}^{\dagger}) + \sqrt{s}(A\hat{a}^{\dagger} + \bar{A}\hat{\alpha}^{\dagger})e^{\dagger} + \sqrt{n}\right)|0_p\rangle \tag{5.5}$$

$$+ |1\rangle\langle 1| \otimes \left(\sqrt{u}\hat{\alpha}^{\dagger} + \sqrt{1-u}\right)|0_p\rangle\,, \tag{5.6}$$

where four different excitation scenarios are considered. In the first case, the bright state $|0\rangle$ of the qubit is transformed via ideal excitation scenario, where the population is transferred to the excited state a single photon is created. To capture the finite visibility of this photon, it is split into an indistinguishable (distinguishable) mode with creation operator $\hat{a}^{\dagger}$ ($\hat{\alpha}^{\dagger}$). The parameter $A = \sqrt[4]{V}$ makes sure that these modes have the appropriate likelihood, with $A^2 + \bar{A}^2 = 1$.

Since the optical excitation pulse has a finite length, there is a chance $p_{\text{double}}$ that the qubit is excited, spontaneously emits a photon and is re-excited during the pulse. The emitted photon is inevitably lost as it is temporally confined within the laser pulse[3].

Hence, this first photon has to be described with a separate photonic mode, which we call $\hat{e}^\dagger|0_p\rangle$ and trace out immediately after the optical pulse has been performed.

Lastly, the optical excitation might not transfer all of the population in state $|0\rangle$ to the excited state. This part with amplitude $p_{\text{no-exc}}$ will hence be connected to the photonic vacuum state.

The probabilities of these events are modeled as mutually exclusive, such that $s = p_{\text{double}}$, $n = p_{\text{no-exc}}$ and $q = 1 - s - n$.
The $|1\rangle$-part of the qubit state can undergo some excitation as well. Short laser pulses have a finite spectral width. If the optical transition connecting state $|1\rangle$ is not far detuned from the optical transition of state $|0\rangle$, off-resonant excitation may occur with probability $u = p_{\text{off}}$. We model this with a separate photonic mode $\hat{\tilde{a}}^\dagger|0_p\rangle$, which is assumed to be fully distinguishable from the other photon modes.

Applying the isometry in Eq. 5.4 directly to Eq. 5.3 results in a complicated density matrix. Instead, we track how the channel alters all elements of the density matrix by applying it to a (non-normalized) toy density matrix

$$\sigma = |0\rangle\langle 0| + |0\rangle\langle 1| + |1\rangle\langle 0| + |1\rangle\langle 1|. \tag{5.7}$$

This is advantageous, as the Barrett-Kok protocol requires two optical pulses with subsequent photon interference, so we can re-use our findings for both excitation rounds. Additionally to applying the channel, we add losses with probability $p_{\text{loss}}$ to all photon modes via

$$\hat{a}^\dagger \to \bar{l}\hat{a}^\dagger + l\hat{\kappa}^\dagger, \tag{5.8}$$

where $l = \sqrt{p_{\text{loss}}}$ and $\bar{l} = \sqrt{1-l^2}$. The loss mode $\hat{\kappa}^\dagger$ is traced out subsequently.

With this, we find[1]

$$\begin{aligned}
\sigma_1^{(1)} = |0\rangle\langle 0| \otimes \Big[ (q+s)\Big[A^2\left(\bar{l}^2\hat{a}^\dagger|0_p\rangle\langle 0_p|\hat{a} + l^2\right) + \bar{A}^2\left(\bar{l}^2\hat{\alpha}^\dagger|0_p\rangle\langle 0_p|\hat{\alpha} + l^2\right)\Big] + \\
\sqrt{qn}\,\bar{l}\left(\hat{a}^\dagger|0_p\rangle + \langle 0_p|\hat{a}\right) + n\Big] \\
+ |0\rangle\langle 1| \otimes \left[\sqrt{q(1-u)}A\bar{l}\hat{a}^\dagger|0_p\rangle + \sqrt{n(1-u)}\right] \\
+ |1\rangle\langle 0| \otimes \left[\sqrt{q(1-u)}A\bar{l}\langle 0_p|\hat{a} + \sqrt{n(1-u)}\right] \\
+ |1\rangle\langle 1| \otimes \left[u\left(\bar{l}^2\hat{\tilde{a}}^\dagger|0_p\rangle\langle 0_p|\hat{\tilde{a}} + l^2\right) + 1 - u\right].
\end{aligned}$$

### 5.1.3. EARLY TIMEBIN - PHOTON INTERFERENCE

At this point, the photons arrive at the central beamsplitter, where they interfere. We model the beamsplitter as unbalanced and loss-free. The photonic modes $\hat{a}^\dagger, \hat{\alpha}^\dagger$ and $\hat{\tilde{a}}^\dagger$ of qubit $A$ and $\hat{b}^\dagger, \hat{\beta}^\dagger$ and $\hat{\tilde{\beta}}^\dagger$ of qubit $B$ transform to where $r = \sqrt{R_{\text{bs}}}$ and $t = \sqrt{T_{\text{bs}}}$ are the reflectance and transmittance coefficients of the beamsplitter with $R_{\text{bs}} + T_{\text{bs}} = 1$.

The capitalized photonic modes originating from qubit $B$ indicate that there is no interference between the distinguishable photon modes. All forms of the letter $C(D)$ are considered to be in one arm of the beamsplitter and routed to detector $C$ ($D$).

[1] We immediately trace out the photon mode $\hat{e}^\dagger|0_p\rangle$ and omit distinguishable photon modes in the coherence terms for readability as they will be discarded by the measurements of the photons in the later steps of the protocol anyway.

$$\begin{aligned}
\hat{a}^\dagger &\to r\hat{c}^\dagger + t\hat{d}^\dagger, \quad \hat{b}^\dagger \to t\hat{c}^\dagger - r\hat{d}^\dagger,\\
\hat{\alpha}^\dagger &\to r\hat{\gamma}^\dagger + t\hat{\delta}^\dagger, \quad \hat{\beta}^\dagger \to t\hat{\Gamma}^\dagger - r\hat{\Delta}^\dagger,\\
\hat{\tilde{\alpha}}^\dagger &\to r\hat{\tilde{\gamma}}^\dagger + t\hat{\tilde{\delta}}^\dagger, \quad \hat{\tilde{\beta}}^\dagger \to t\hat{\tilde{\Gamma}}^\dagger - r\hat{\tilde{\Delta}}^\dagger,
\end{aligned}$$

Similarly to the optical pulse, we use a two-qubit toy density matrix to determine the prefactors added from this operation. As the two qubits so far are completely independent from each other, we can use the previously determined $\sigma_1^{(1)}$ for both qubits individually. This results in

$$\begin{aligned}
\sigma_{\mathrm{A}}^{(1)} = &|0\rangle\langle 0| \left[x_{\mathrm{A}} X_{\mathrm{A}} + n_{\mathrm{A}} + \sqrt{q_{\mathrm{A}} n_{\mathrm{A}}}\left(r(\hat{c}^\dagger + \hat{c}) + t(\hat{d}^\dagger + \hat{d})\right)\right]\\
&+ |0\rangle\langle 1| \left[\sqrt{q_{\mathrm{A}}(1-u_{\mathrm{A}})} A \bar{l}_{\mathrm{A}}\left(r\bar{l}_{\mathrm{C}}\hat{c}^\dagger + t\bar{l}_{\mathrm{D}}\hat{d}^\dagger\right) + \sqrt{n_{\mathrm{A}}(1-u_{\mathrm{A}})}\right]\\
&+ |1\rangle\langle 0| \left[\sqrt{q_{\mathrm{A}}(1-u_{\mathrm{A}})} A \bar{l}_{\mathrm{A}}\left(r\bar{l}_{\mathrm{C}}\hat{c} + t\bar{l}_{\mathrm{D}}\hat{d}\right) + \sqrt{n_{\mathrm{A}}(1-u_{\mathrm{A}})}\right]\\
&+ |1\rangle\langle 1| \left[u_{\mathrm{A}} Y_{\mathrm{A}} + 1 - u_{\mathrm{A}}\right],
\end{aligned} \tag{5.9}$$

and

$$\begin{aligned}
\sigma_{\mathrm{B}}^{(1)} = &|0\rangle\langle 0| \left[x_{\mathrm{B}} X_{\mathrm{B}} + n_{\mathrm{B}} + \sqrt{q_{\mathrm{B}} n_{\mathrm{B}}}\left(t(\hat{c}^\dagger + \hat{c}) - r(\hat{d}^\dagger + \hat{d})\right)\right]\\
&+ |0\rangle\langle 1| \left[\sqrt{q_{\mathrm{B}}(1-u_{\mathrm{B}})} A \bar{l}_{\mathrm{B}}\left(t\bar{l}_{\mathrm{C}}\hat{c}^\dagger - r\bar{l}_{\mathrm{D}}\hat{d}^\dagger\right) + \sqrt{n_{\mathrm{B}}(1-u_{\mathrm{B}})}\right]\\
&+ |1\rangle\langle 0| \left[\sqrt{q_{\mathrm{B}}(1-u_{\mathrm{B}})} A \bar{l}_{\mathrm{B}}\left(t\bar{l}_{\mathrm{C}}\hat{c} - r\bar{l}_{\mathrm{D}}\hat{d}\right) + \sqrt{n_{\mathrm{B}}(1-u_{\mathrm{B}})}\right]\\
&+ |1\rangle\langle 1| \left[u_{\mathrm{B}} Y_{\mathrm{B}} + 1 - u_{\mathrm{B}}\right].
\end{aligned} \tag{5.10}$$

Here, the subscripts $A$ and $B$ indicate the corresponding qubit, $x = q + s$, and

$$\begin{aligned}
X_{\mathrm{A}} =& A^2 \bar{l}_{\mathrm{A}}^2\left(r\bar{l}_{\mathrm{C}}\hat{c}^\dagger + t\bar{l}_{\mathrm{D}}\hat{d}^\dagger\right)\left(r\bar{l}_{\mathrm{C}}\hat{c} + t\bar{l}_{\mathrm{D}}\hat{d}\right) + \bar{A}^2 \bar{l}_{\mathrm{A}}^2\left(r\bar{l}_{\mathrm{C}}\hat{\gamma}^\dagger + t\bar{l}_{\mathrm{D}}\hat{\delta}^\dagger\right)\left(r\bar{l}_{\mathrm{C}}\hat{\gamma} + t\bar{l}_{\mathrm{D}}\hat{\delta}\right) +\\
&\bar{l}_{\mathrm{A}}^2\left(r^2 l_{\mathrm{C}}^2 + t^2 l_{\mathrm{D}}^2\right) + l_{\mathrm{A}}^2,\\
X_{\mathrm{B}} =& A^2 \bar{l}_{\mathrm{B}}^2\left(t\bar{l}_{\mathrm{C}}\hat{c}^\dagger - r\bar{l}_{\mathrm{D}}\hat{d}^\dagger\right)\left(t\bar{l}_{\mathrm{C}}\hat{c} - r\bar{l}_{\mathrm{D}}\hat{d}\right) + \bar{A}^2 \bar{l}_{\mathrm{B}}^2\left(t\bar{l}_{\mathrm{C}}\hat{\Gamma}^\dagger - r\bar{l}_{\mathrm{D}}\hat{\Delta}^\dagger\right)\left(t\bar{l}_{\mathrm{C}}\hat{\Gamma} - r\bar{l}_{\mathrm{D}}\hat{\Delta}\right) +\\
&\bar{l}_{\mathrm{B}}^2\left(t^2 l_{\mathrm{C}}^2 + r^2 l_{\mathrm{D}}^2\right) + l_{\mathrm{B}}^2,\\
Y_{\mathrm{A}} =& \bar{l}_{\mathrm{A}}^2\left(r\bar{l}_{\mathrm{C}}\hat{\tilde{\gamma}}^\dagger + t\bar{l}_{\mathrm{D}}\hat{\tilde{\delta}}^\dagger\right)\left(r\bar{l}_{\mathrm{C}}\hat{\tilde{\gamma}} + t\bar{l}_{\mathrm{D}}\hat{\tilde{\delta}}\right) + \bar{l}_{\mathrm{A}}^2\left(r^2 l_{\mathrm{C}}^2 + t^2 l_{\mathrm{D}}^2\right) + l_{\mathrm{A}}^2,\\
Y_{\mathrm{B}} =& \bar{l}_{\mathrm{B}}^2\left(t\bar{l}_{\mathrm{C}}\hat{\tilde{\Gamma}}^\dagger - r\bar{l}_{\mathrm{D}}\hat{\tilde{\Delta}}^\dagger\right)\left(t\bar{l}_{\mathrm{C}}\hat{\tilde{\Gamma}} - r\bar{l}_{\mathrm{D}}\hat{\tilde{\Delta}}\right) + \bar{l}_{\mathrm{B}}^2\left(t^2 l_{\mathrm{C}}^2 + r^2 l_{\mathrm{D}}^2\right) + l_{\mathrm{B}}^2,
\end{aligned}$$

where we included already loss $l_{\mathrm{C}}$ and $l_{\mathrm{D}}$ after the beamsplitter for the two detector paths $C$ and $D$. For brevity, we omit writing out the photonic vacuum state $|0_p\rangle$ in Eq. 5.9. The two-qubit state is then

$$\sigma_2^{(1)} = \sigma_{\mathrm{A}}^{(1)} \otimes \sigma_{\mathrm{B}}^{(1)} \tag{5.11}$$

### 5.1.4. EARLY TIMEBIN - HERALDING

In order to successfully herald entanglement, one photon needs to detected in the early timebin. For the derivation here, we consider the case of a detection event in detector $C$. For this, we trace over all non-zero photon modes that can be detected by detector $C$.

Since typically photon detectors are not number-resolving, we also consider two-photon states. The operation can be expressed as

$$\sigma_2^{(2)} = \sum_{i \in P} \langle i | \sigma_2^{(1)} | i \rangle , \tag{5.12}$$

with $P = \{|1_c\rangle, |1_\gamma\rangle, |1_c 1_\gamma\rangle, |2_c\rangle, ...\}$. We can additionally make use of the fact that photon modes of the form $|1_c 1_d\rangle$ can be rejected by the protocol and exclude them from $P$.

It is essential to realize, that only terms in Eq. 5.9 containing complete pairs of creation and annihilation operators of the same mode contribute to $\sigma_2^{(2)}$. Any unpaired operator (e.g. a single $\hat{c}^\dagger$ or a term like $\hat{c}^\dagger \hat{d}^\dagger \hat{c}$) vanishes under the trace. With this method, all 16 elements $E_{ijkl}$ of $\sigma_2^{(2)}$ can be determined.

At this point, we also incorporate dark counts of the detectors, that lead to independent heralding events. Conceptually, we have to multiply Eq. 5.9 with a term $(p_C^{DC} \hat{g}^\dagger \hat{g} + 1 - p_C^{DC})((p_D^{DC} \hat{h}^\dagger \hat{h} + 1 - p_D^{DC}))$, where $p_Q^{DC}$ is the dark count probability on detector $Q$ and $\hat{g}^\dagger$ ($\hat{h}^\dagger$) is the dark count photon mode on detector $C$ ($D$). If we herald on photon modes in detector $C$, a dark count in detector $D$ actually invalidates the herald. This leads to a factor $(1 - p_D^{DC})$ for terms that can lead to a valid herald on detector $C$. On the other hand, a dark count on detector $C$ does not invalidate heralds as the detectors are assumed to be non-number resolving. However, it creates a valid herald with probability $p_C^{DC}$ for terms that are not connected to any photon mode.

### 5.1.5. TIME BIN PULSE ON THE QUBITS

We model the imperfect $\pi$-pulse on the qubits separating the timebins as fully depolarizing noise. The transformations are

$$\sigma_2^{(3)} = (1 - p_\pi^A)(U_A \otimes I_B)\sigma_2^{(2)}\left(U_A^\dagger \otimes I_B\right) + \frac{p_\pi^A}{2} I_A \otimes \mathrm{Tr}_A\left(\sigma_2^{(2)}\right), \tag{5.13}$$

$$\sigma_2^{(4)} = (1 - p_\pi^B)(I_A \otimes U_B)\sigma_2^{(3)}\left(I_A \otimes U_B^\dagger\right) + \frac{p_\pi^B}{2} \mathrm{Tr}_B\left(\sigma_2^{(3)}\right) \otimes I_B, \tag{5.14}$$

where $p_\pi$ is the error probability of the $\pi$ pulse, $U = R_y(\pi)$ is the rotation unitary for $\pi$ around the $y$-axis, $I$ is the identity operation and $\mathrm{Tr}_i$ is the partial trace over qubit $i$. The subscripts $A$ and $B$ indicate on which qubit the operation acts.

### 5.1.6. LATE TIMEBIN AND TOTAL RESULT

For the late timebin, we perform the same steps as described in Sec. 5.1.2 to 5.1.4 on $\sigma_2^{(4)}$. After these steps, we end up with $\sigma_2^{(f)}$, which captures the transformation that all elements of the two-qubit density matrix $\sigma_2^{(1)}$ undergo.

By multiplying $\rho_{ini}^A \otimes \rho_{ini}^B$ from Eq. 5.3 element-wise with $\sigma_2^{(f)}$, we receive the total heralded density matrix $\rho_{tot}$ for two heralding photon events in detector $C$. The same steps can be repeated for the remaining three heralding patterns. Under the assumption that the beamsplitter is perfect and that the losses and dark counts in both detector arms are equal, the outcome is the identical for all patterns.

$\rho_{tot}$ is not normalized, its trace corresponds to the heralding probability of the corresponding detector click pattern.

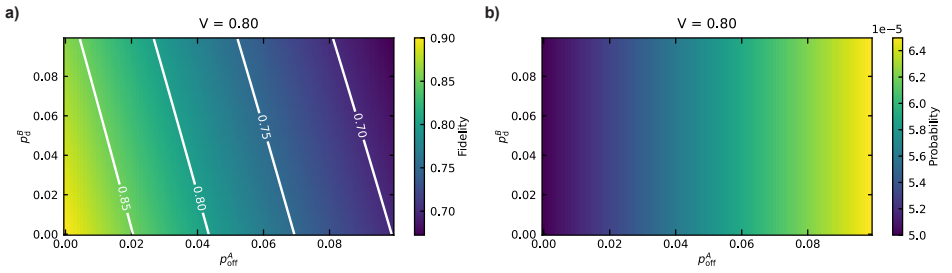


Figure 5.2: **Error-model simulations.** The expected (a) fidelity and (b) heralding probability are shown under the assumption of no errors except 99 % loss from both emitters, off-resonant excitation on Alice, double-excitation on Bob and a Hong-Ou-Mandel visibility of 0.8. Vanishing errors lead to the expected fidelity of 0.9 with maximum probability at the expected protocol success probability. The isolines show a stronger impact of off-resonant excitation on the fidelity. Off-resonant excitation also enhances the heralding probability due to the creation of more photons than desired.

### 5.1.7. EVALUATION OF THE PROTOCOL



We implement the error model in Python with *sympy*. Working with the assumption that all detection patterns are equally likely and the generated state is the same up to the parity of the click pattern, we extract the fidelity $\mathcal{F}$ with respect to the ideal Bell state $|\psi_+\rangle$ and success probability of the protocol as

$$\mathcal{F} = \langle\psi_+|\,\rho_{\text{tot}}\,|\psi_+\rangle\,, \tag{5.15}$$

$$p_{\text{success}} = 4\,\text{Tr}\left(\rho_{\text{tot}}\right). \tag{5.16}$$

In scenarios with different detector efficiencies, an imperfect beamsplitter or other unbalancing errors, the protocol has to be evaluated for all four possible heralding click patterns to get an average fidelity and success probability.

We analyze and verify parameterized analytic solution for $\mathcal{F}$ for different regimes. Figure 5.2(a) shows the expected fidelity for a fixed interference visibility $V = 0.8$ and varying off-resonant (double) excitation error probability on Alice (Bob), respectively. Additionally, both emitters are assumed to have a photon loss probability of 99 %. In the error-free scenario, the fidelity and rate can be calculated to be bound to $\mathcal{F} = 1/2 + V/2 = 0.9$ and $p_{\text{herald}} = \frac{1}{2}(1-p^A_{\text{loss}})(1-p^B_{\text{loss}}) = 5\times10^{-5}$, which is represented by the simulation. Furthermore, it is apparent from the slope of the isolines that off-resonant excitation errors impact the achievable fidelity more than double excitation errors. This can be intuitively understood by considering the resulting state in case of an error. For a single off-resonant excitation error, a photon is connected the wrong qubit state, resulting (on average) in a fully mixed two-qubit state. When a single double-excitation error occurs, the coherence between the qubit and the photon is lost, resulting in a mixed state $\rho_{\text{m}} = \frac{1}{2}(|01\rangle\langle01| + |10\rangle\langle10|)$. Crucially, the populations of this mixed state are still the same as for the intended Bell state, hence the effect on the fidelity is reduced compared to the off-resonant excitation.

In Figure 5.2(b), we show the probability of a successful herald, retrieved from the trace of the final density matrix. As expected, double-excitation errors do not influ-

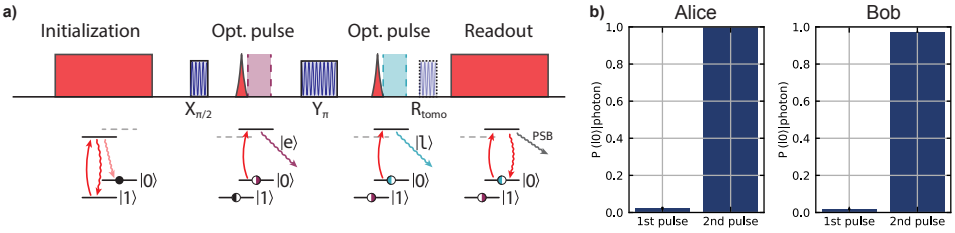


Figure 5.3: **Spin-Photon correlation measurements.** (a) Experimental sequence. After initializing the qubit into state $|x\rangle$, two optical pulses separated by a $\pi$-pulse on the qubit are performed. A tomography pulse selects the readout basis before reading out the spin. The lower row shows the evolution of the qubit for the spin-photon correlation measurement, where the readout is performed in the $Z$-basis. (b) Measured spin-photon correlations for two SnVs. The sequence should result in qubit state $|1\rangle$ when a photon is detected after the first optical pulse and state $|0\rangle$ after the second optical pulse. The deviations from the ideal case are effects of imperfect selectivity of the optical pulse and MW pulse errors. Errorbars indicate the readout uncertainty.

5

ence the success probability. Off-resonant excitation errors however enhance the success probability. Intuitively, this can be seen as follows: If an off-resonant excitation event occurs in any timebin, this emitter has the chance to emit a second photon in the other timebin from its bright state. Therefore, more photons are available. In the limit of high loss, events where an off-resonant photon coincides with another photon in the same timebin and therefore leads to a rejected event are rare and do not counteract the enhanced heralding probability completely.

## 5.2. SPIN-PHOTON CORRELATIONS

The first straight-forward measurement to combine microwave control with single photon generation is to measure the correlation between the qubit spin state and generated single photons. Fig. 5.3(a) shows the experimental and logical sequence for this experiment. After initializing the qubit into $|0\rangle$ it is prepared into an equal superposition state with a MW $\pi/2$-pulse. Subsequently, the population in $|0\rangle$ is excited with an optical pulse to generate a single photon. A MW $\pi$-pulse flips the population before another optical pulse creates a single photon from the $|0\rangle$ state. Finally, conditioned on detecting a single photon after either the first or second optical pulse, the qubit state is read out in the basis selected by the MW tomography pulse. The correlation between the timebin in which the photon was detected and the qubit readout in the $Z$ basis is shown in Fig. 5.3(b) for the two SnV centers discussed in Sec. 4.5.3.

A clear correlation between the qubit state and the arrival bin of the photon can be observed. If the photon was detected in the early bin, the qubit state is expected to be $|1\rangle$ due to the MW $\pi$-pulse changing the population after creating the photon from exciting $|0\rangle$. On the other hand, the creation of a photon form $|0\rangle$ in the late bin leaves the qubit in the same state for the readout. This expectation is clearly represented in the shown data, implying that the combined MW and optical control works as expected. The fidelities of the spin-photon correlated state are $\mathcal{F}_{\text{alice}} = 0.977(7)$ and $\mathcal{F}_{\text{bob}} = 0.954(5)$, respectively.

The deviation from the ideal case for the early bin is a combination of off-resonant excitation connecting a photon to the $|1\rangle$ state, MW pulse errors effectively not flipping

the qubit state after detecting an early photon. For the late bin, only off-resonant excitation can cause an error as no more MW pulses are applied afterwards. In principle, also spin-flipping events, where the excited state does not preserve the spin-state during a ZPL decay event, can also cause errors. We ignore these in our discussion, as the probability is less than 1 % for both emitters. The high quality of the spin-photon correlated states gives high confidence over the quality of MW pulses as well as the state-selectivity of the optical pulses on both emitters.

## 5.3. HERALDED ENTANGLEMENT OF TWO TIN-VACANCY CENTERS

With both SnV centers being able to create spin-photon correlated states, we can create spin-spin entangled states by playing the sequence simultaneously on both qubits and selecting on events where a photon was detected after the first and second optical pulse respectively. The experimental sequence is that same as in Fig. 5.3(a), only now with the condition of detecting a photon both in the early and late detection window. For this experiment, we implement an additional piece of logic that suppresses the MW $\pi$-pulse on one emitter if no photon was detected in the early time bin and hence the attempt already cannot lead to a success. Moreover, we calibrated two sets of MW $\pi/2$-pulses, where the preparation pulse in Fig. 5.3 is played with lower power, resulting in less heating whereas the (potential) tomography pulse after the sequence is played at higher power to maximize its fidelity. The reason for is that the main limitation in our setup is heating from the microwave pulses on one of the emitters as it requires 10x higher driving power than the other SnV. As we work in the limit of low detection efficiency with $p_{\text{det}} < 0.1\,\%$, almost all attempts fail already at the first timebin, and we suppress roughly 99.9 % of the MW pulses. If we do not suppress the MW pulse, we would have to run with a much lower attempt rate to avoid excessive heating.

This experimental sequence should result in the Bell state $|\Psi^{\pm}\rangle$ upon heralding, where the sign is determined by the click-pattern of the detectors. We employ a compiled Pauli correction gate for the tomography pulse such that the resulting state is always $|\Psi^{-}\rangle$. This state is anti-correlated in the $\langle XX\rangle$, $\langle YY\rangle$, and $\langle ZZ\rangle$-bases.

The setup used for this experiment is depicted in Fig. 2.3 with two changes. First, the seed laser for the optical pulse generation is the same for both nodes. This removes the necessity to implement a frequency lock between the two lasers, which would be necessary to ensure a stable phase of the entangled state throughout the whole experiment. Secondly, the signal of the SNSPDs is routed to the timetagger and an additional field-programmable gate array (FPGA) which allows for real-time logic like conditional MW pulse switching and heralding of photon detection events. Before starting the experiment, we defined a set of parameters for the analysis of the measurement. We limit the detection window to a length of 20 ns in accordance to the TPQI measurement in Sec. 4.5.3 to guarantee a good signal-to-noise ratio. This window is about three times the optical lifetime of the emitters and hence captures most of the emitted photons. For debugging purposes, the acceptance window to herald an event is chosen slightly larger than the detection window and includes part of the laser pulse. This leads to false heralds which are discarded by the analysis if at least one of the heralding photons was not

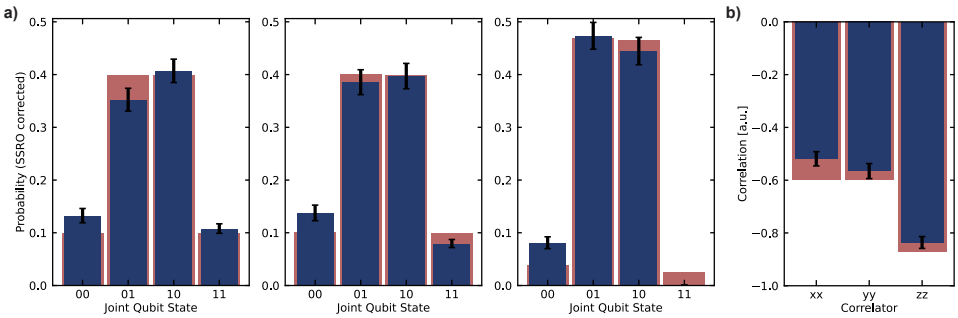


Figure 5.4: **Entanglement of two tin-vacancy centers.** The sequence in Fig. 5.3(a) played on both SnVs and conditioned on detection of a photon in both timebins heralds an entangled state $|\Psi^{\pm}\rangle$ depending on the click pattern. Via Pauli correction, we prepare the state $|\Psi^{-}\rangle$ for any herald. (a) The panels show the readout corrected correlators in different bases for of the two-qubit state. The red bars are expected correlation based on known error sources. (b) The correlation values of the experiment are slightly worse compared to the fidelity predicted by the simulation.

5

detected in the detection window. To ensure good visibility of the photons following Fig. 4.6, we limit the maximum detection time difference of the photons with respect to the detection window to $|\Delta t|_{\max} = 10\,\text{ns}$. Both of these metrics are available at the time of the herald and could be checked live when using appropriate timetaggers. Additionally, we discard blocks of data where the calibration metrics are out of a pre-defined and pre-characterized bound. In particular, for the data reported here, we discard one block of data where the single shot readout was subject to high dark counts which result in a mis-calibrated readout duration. It is important to note that the discard of the data is already done before the time of its acquisition. Hence, no post-selection per se is necessary and the entanglement is heralded and event-ready.

The readout correct measurement outcomes are shown in Fig. 5.4. The fidelity of the entangled state is given by

$$\mathscr{F} = \frac{1}{4}(1 - \langle XX\rangle - \langle YY\rangle - \langle ZZ\rangle). \tag{5.17}$$

With eq. 5.17, we find $\mathscr{F} = 0.73(1)$, clearly violating the classical threshold of 0.5. In red, the expected outcomes based on the model in Sec. 5.1 are presented. The experimentally estimated error probabilities in Tab. 5.1 are determined by supporting measurements like calibrations.

The measurement is conducted over one week in blocks of 1.5 h. Between each block, an automatic routine re-calibrates the lasers, single-shot readout duration, MW frequency, optimizes the cross-polarization rejection and takes supporting data like saturation curves and optical pulse measurements. We predefine boundary conditions for the calibrations to be valid. As for the time-tag information described above, this information is in principle available at the moment of the experimental run and could (with some adaptation of the experimental code) prevent the acquisition of faulty data.

In total, we gather 70 blocks of data out of which one gets discarded due to an invalid readout calibration, leading to unusable readout outcomes. This results in 822

Table 5.1: **Estimated errors for the experiment.** The values are extracted from supporting calibration measurements. We assume negligible dark count contributions for the simulation. For each error source, we consider two scenarios: First, we show the fidelity of the entangled state if the source was the only imperfection in the simulation. Secondly, we show the fidelity if all other errors were present except the reported error. The base fidelity of the simulation with all error sources is $\mathscr{F} = 0.767$.

| Source of infidelity | Value for simulation | Expected fidelity if only source present | Expected improvement once removed |
|---|---|---|---|
| $V$ | 0.861 | 0.930 | 0.815 |
| $R_{\mathrm{bs}}$ | 0.542 | 0.999 | 0.768 |
| $T_{\mathrm{bs}}$ | 0.458 | 0.999 | 0.769 |
| $p^A_{\mathrm{ini}}$ | 0.002 | 0.998 | 0.768 |
| $p^B_{\mathrm{ini}}$ | 0.010 | 0.990 | 0.773 |
| $p^A_{\pi/2}$ | 0.02 | 0.990 | 0.773 |
| $p^B_{\pi/2}$ | 0.01 | 0.995 | 0.770 |
| $p^A_{\pi}$ | 0.02 | 0.980 | 0.780 |
| $p^B_{\pi}$ | 0.01 | 0.990 | 0.773 |
| $p^A_{\mathrm{double}}$ | 0.050 | 0.975 | 0.784 |
| $p^B_{\mathrm{double}}$ | 0.084 | 0.958 | 0.796 |
| $p^A_{\mathrm{off}}$ | 0.008 | 0.977 | 0.783 |
| $p^B_{\mathrm{off}}$ | 0.019 | 0.945 | 0.808 |
| $p^A_{\mathrm{no-exc}}$ | 0.050 | 1.000 | 0.769 |
| $p^B_{\mathrm{no-exc}}$ | 0.050 | 1.000 | 0.770 |

data points. The resulting entanglement rate is $r_{\mathrm{ent}} = 2.2\,\mathrm{mHz}$ excluding overhead. This matches well with the expected entanglement rate $r_{\mathrm{ent}} = 2\,\mathrm{mHz}$ based on the photon detection probability ($p_{\mathrm{det}} = 2 \times 10^{-3}$ per emitter) and attempt rate $r_{\mathrm{attempt}} = 1\,\mathrm{kHz}$ using[4]

$$r_{\mathrm{ent}} = \frac{p_{\mathrm{det}}^2}{2} r_{\mathrm{attempt}}. \tag{5.18}$$

The data points for the different correlators are distributed probabilistically due to the false heralds as explained above, leading to 303/259/260 data points for the $XX/YY/ZZ$ correlator, respectively.

The presented analysis is to be understood as a preliminary discussion of the data. There are still several aspects that need to be investigated more carefully.

The readout correction is performed via iterative bayesian unfolding to prevent unphysical results that would be attainable by simple matrix inversion (see Appendix A of Ref.[5] for details). The uncertainties are then determined by a Monte-Carlo simulation sampling from the distribution of readout fidelities obtained during the periodic

calibrations in the experiment. This current way for this error propagation leads to balanced error bars, which is unreasonable for data points at extreme populations of 0 or 1. Therefore, a more elaborate error propagation needs to be employed to estimate the uncertainty of the $|11\rangle$-contribution in the $ZZ$-basis.

The simulation in Fig. 5.4(a) describes the observed correlations qualitatively, however the unbalance between $|00\rangle$ and $|11\rangle$ events seems to be stronger in the measured data than predicted by the simulation. The origin of the discrepancy between simulation and experiment might be an overestimation of some error sources and/or some oversimplifications in the model. For instance, we did not conduct proper gate calibrations via randomized benchmarking or gate-set tomography[6], but rather estimate the error from the infidelity of the measurement outcome when detecting an early photon in the spin-photon correlations in Fig. 5.3(b). For this, we identify off-resonant excitation as well as MW $\pi$-pulse errors as sources of infidelity. We determine the off-resonant excitation probability in an independent measurement and assign the remaining infidelity of the microwave pulse via

$$p_\pi^{\text{simu}} = 2 \cdot \left(\bar{\mathcal{F}}_{\text{earlybin}} - p_{\text{off}}/2\right). \tag{5.19}$$

The factor 2 originates from the fact that we model the MW pulse error as fully depolarizing, which can be interpreted as effectively resulting in the correct pure state half of the times when an error occurs. Since the qubit was originally prepared in an equal superposition, off-resonant excitation can only occur with half the probability compared to the measurement in which it is determined.

The corresponding MW $\pi$-pulse errors are $p_\pi^A = 0.02$ and $p_\pi^B = 0.01$. Due to a lack of a better metric, we assume the same error magnitude of the MW $\pi/2$-pulses.

Additionally, we model the error as a fully depolarizing channel. In the case of a coherent rotation-angle error, this might overestimate the impact on the resulting states, especially due to the loss of all coherence of the superposition-bases. At the moment of writing, it is yet to be determined whether all of the used error sources as well as their implementation in the model are completely consistent with each other. However, we expect that a more thorough modeling will likely change the value of the predicted fidelity, but not to an extent that the model would start to strongly disagree with the data. The simulated expectation in Fig. 5.4 should therefore be only seen as a qualitative estimate rather than a complete description of the experiment settings.

## 5.4. DISCUSSION

We present conclusive evidence for heralded entanglement between tin-vacancy centers in nanophotonic diamond waveguides. The extracted fidelity of $\mathcal{F} = 0.73(1)$ is to be understood as a preliminary analysis, further analysis is required to fully incorporate all uncertainties properly. The measurement outcomes qualitatively match the expectation from the simulation with the error model in Sec. 5.1.

In the current configuration, we employ magnetic field tuning to ensure indistinguishability of the emitted photons. This is not a feasible tuning mechanism for follow-up experiments. Frequency shifting of photons leads to additional losses as detailed in Sec. 4.1.1 and requires many optical elements. A promising route for tuning is employing

strain-tuning, which has been demonstrated for waveguide devices with similar geometry to the ones in this work[7].

The experimental speed and quality are limited by the MW-drive induced heating. For the experiment shown here, we need to limit the attempt rate to 1 kHz to avoid excessive heating. Improving the MW delivery via superconducting transmission lines has the potential to achieve high quality control with little heat[8]. Additionally, the gate fidelity can be improved by higher Rabi frequencies. Another necessary improvement is the initialization speed of the spin. For good readout with current collection efficiencies on the percent level in the PSB, a cyclicity of more than 100 is desirable. Initialization via spin pumping is the limited to tens of µs, naturally limiting the attempt rate to less than 100 kHz. Measurement-based initialization via short, high-fidelity readout on the µs-scale of the qubit could overcome this limitation.

As the Barret-Kok protocol relies on the detection of two photons, the photon collection efficiency of 0.2 % is a crucial limitation for the success rate of the protocol. As an additional benefit, measurement-based initialization also gains from better collection efficiency. Further improvements can be achieved by optimizing the fiber-waveguide interface and the collection path efficiency.



In a realistic near-term scenario, where heating limitations are overcome, collection efficiencies improved to $p_{\text{det}} = 1\,\%$ and MBI improves the duration of a single entanglement attempt to 5 µs, entanglement rates on the order of 10 Hz should be attainable. Crucially, our platform of broadband nanophotonic devices provides opportunities for multiplexing (e.g. fiber-glued packaging[9] and photonic integration [10]) which could drastically speed up entanglement rates by using multiple emitters per node.

## REFERENCES

[1] S. D. Barrett and P. Kok, *Efficient high-fidelity quantum computation using matter qubits and linear optics,* Physical Review A **71**, 060310 (2005).

[2] M. A. Nielsen and I. L. Chuang, *Quantum Computation and Quantum Information: 10th Anniversary Edition*, 1st ed. (Cambridge University Press, 2012).

[3] S. L. N. Hermans *et al.*, *Entangling remote qubits using the single-photon protocol: An in-depth theoretical and experimental study,* New Journal of Physics **25**, 013011 (2023).

[4] H. Bernien *et al.*, *Heralded entanglement between solid-state qubits separated by three metres,* Nature **497**, 86 (2013).

[5] M. Pompili, *Multi-Node Quantum Networks with Diamond Qubits*, Ph.D. thesis, Delft University of Technology (2021).

[6] E. Nielsen *et al.*, *Gate Set Tomography,* Quantum **5**, 557 (2021).

[7] J. M. Brevoord *et al.*, *Large-range tuning and stabilization of the optical transition of diamond tin-vacancy centers by in situ strain control,* Applied Physics Letters **126** (2025), 10.1063/5.0251211.

[8] I. Karapatzakis *et al.*, *Microwave Control of the Tin-Vacancy Spin Qubit in Diamond with a Superconducting Waveguide,* Physical Review X **14**, 031036 (2024).

[9] B. Zeng *et al.*, *Cryogenic packaging of nanophotonic devices with a low coupling loss <1 dB,* Applied Physics Letters **123**, 161106 (2023).

[10] N. H. Wan *et al.*, *Large-scale integration of artificial atoms in hybrid photonic circuits,* Nature **583**, 226 (2020).

# 6

# CONCLUSION AND OUTLOOK

## 6.1. CONCLUSION

In this thesis, we build and test a quantum network node based on the tin-vacancy center in diamond. We discuss the tin-vacancy center and how it is controlled and show these methods experimentally in various experiments. Here, we provide a brief summary of the chapters in this thesis:

- In Chapter 3, we controlled the electron spin of the tin-vacancy center and investigated the control of surrounding nuclear spins. We compared different control mechanisms for spin-1/2 systems like the tin-vacancy center and spin-1 systems like the nitrogen-vacancy center. Selecting the most suitable control for our system, we entangled the electronic spin with a nuclear spin. Finally, we extract the different hyperfine coupling strengths in the ground and excited state, which is relevant to understand the nuclear spin decoherence during optical activity of the tin-vacancy center.

- In Chapter 4, we performed two-photon quantum interference experiments between two different pairs of tin-vacancy centers. We employed tuning via the magnetic field controlled Zeeman-splitting as well as electro-optic frequency shifting of one of the emitted photons. For all experiments, we found clear signatures of Hong-Ou-Mandel interference and were able to improve the interference visibility by additional time filtering, indicating spectral diffusion as the main limiting noise source.

- In Chapter 5, we derive an analytical error model for the Barrett-Kok protocol, covering the major error sources of our platform. Additionally, we combined the spin control from Chapter 4 with the optical control from Chapter 4 to create spin-photon and heralded spin-spin entangled states. The measured correlations agree qualitatively with the expectations based on the simulations.

## 6.2. ADVANCING QUANTUM NETWORKS WITH THE TIN-VACANCY CENTER

The key challenge for any quantum network platform is scalability. A metric to quantify the effectiveness of a quantum link is its link efficiency, given by the ratio of entanglement distribution over decoherence rate of the qubits used for the operation. While it is an important line of research to decrease the decoherence rate, we will focus this discussion on the entanglement distribution rate as this metric is also of key importance to speed up the runtime of any application requiring multiple entangled states. We split the discussion into near-term improvements and future improvements.

### 6.2.1. NEAR-TERM IMPROVEMENTS

**Frequency tuning** For the experiments in Chapters 4 and 5, the choice of tin-vacancy centers was limited by the spectral distribution of the emitters and the limited tuning mechanisms at our disposal. In a network that facilitates connectivity to multiple nodes, the photons from each node have to be indistinguishable from the connected nodes. Hence, larger tuning ranges are required to combat the spectral distribution. Alternatively, it could also be an option to narrow the distribution to an extent, where no external tuning is needed. As this most likely involves removing all strain from the environment (as axial strain shifts the optical transitions of the SnV), this is not favorable for microwave-based spin control. Using devices with controllable strain has been shown to be able to tune the relevant optical transitions of the SnV by tens of GHz, which is on the order of the spectral distribution in our devices [1]. For long-distance quantum networks, it is favorable to transmit telecom-band photons. For this, quantum frequency conversion can be used [2,3]. This technique also allows effective tuning of the photons onto resonance by adjusting the laser fields involved in the process to guarantee a fixed converted photon frequency.



**Microwave delivery** The experiments in Chapters 3 and 5 were limited by excessive heating of the system caused by the MW pulses. In Chapter 3, this limited the amount of decoupling pulses that we could perform and hence the achievable coherence of the SnV center. In Chapter 5, a slow build-up of heat in the system had to be mitigated via extensive inactive cooling periods, which limited the experimental rate. The microwave delivery is currently implemented via a suspended bondwire with a distance of roughly 100 µm from the diamond. Earlier attempts of on-chip transmission lines out of metal caused instantaneous heating of the tin-vacancy centers, decohering them. Promising advances have been shown with superconducting microwave transmission lines [4]. Alternatively, thermally decoupled rigidly connected flip-chips could decrease the required amount of microwave power drastically. Additionally, strain engineering with static strain can improve the susceptibility to the microwave field, further lowering the required powers [5]. Increasing the rate at which entanglement generation can be attempt is vital for future quantum networks.

**Collection efficiency** The experiments in Chapter 3 have been conducted with a confocal microscopy setup. While with the collection efficiency of ZPL photons of the NV center has been optimized to a few percent with confocal setups[6] and to 20 %[7] with an emission-enhancing micro-cavity, both methods involve bulky microscope objectives to address the emitters. As future quantum nodes likely require multiple emitters per node to enable multiplexed operation, this approach is not desirable. In Chapters 4 and 5, we used tapered optical fibers to address SnVs in nanophotonic waveguides. While we operated in a non-optimal lensed-fiber configuration with limited collection efficiency, the waveguide-to-fiber interface has been shown to reach up to 90 % transmission efficiency, bringing collection efficiencies above 10 % into reach. Additionally, this approach allows for access to multiple emitters within one network node. In our experiments, the fiber-waveguide interface was limited due to strong perturbations of the SnV upon physical contact between the fiber and the waveguide. We suspect either heat or vibrationally induced strain to be the cause, both of which can be solved via engineering solutions in the setup. Improving the collection efficiency directly translates into faster entanglement rates.

**Device fabrication** As the results in Chapter 4 suggest, our Hong-Ou-Mandel visibility is likely limited by spectral diffusion. We suspect to main causes for this. First, we suffered from graphitization of the diamond surface during the annealing. This graphite had to be removed subsequently, which resulted in shallower SnVs than planned for, which additionally experience a less perfect diamond surface. Secondly, our SnV implantation procedure creates a lot of damage in the crystal. In Chapter 3, we observe an electron bath that limits our qubit coherence, likely this also has an influence on the optical stability. There are multiple paths forward to reduce the damage in the crystal and improve the stability of SnV centers. Shallow ion implantation with overgrowth[8] significantly reduces the implantation damage and allows for an arbitrary implantation depth by controlling the subsequent overgrowth thickness. A challenge for this technique is the creation of a defect-free interface between the substrate diamond and the overgrown layer. An alternative approach is the fabrication of thin-film diamond[9,10] that can be bonded to a carrier substrate afterwards. This technique has the advantage that no undercut of the diamond is required anymore, allowing for the „simple“ fabrication of devices along arbitrary directions in the membrane plane.



Improvements on all capabilities discussed here could enable considerable entanglement rates in the near term. Boosting the detection probability of a single ZPL photon after a short optical excitation to 1 % and increasing the entanglement attempt rate to 50 kHz[1] would already result in an entanglement success rate on the order of Hz with the Barrett-Kok protocol as opposed to the achieved tens of mHz[12,13].

[1] In experiments with NV centers in diamond, entanglement attempt rates of more than 100 kHz have been achieved[11]. A major difference is between the NV and SnV is the speed at which initialization of the spin can be achieved, which is why we take a more conservative attempt rate as estimate here.

### 6.2.2. FUTURE IMPROVEMENTS

The SnV center is an exciting platform to advance quantum networks along a new dimension: Multiplexing. In a future quantum network, it is highly unlikely that entanglement between distant nodes will be established only by utilizing a single pair of spin-photon interfaces. In a setting of two nodes separated by $L = 50\,\mathrm{km}$ with the heralding station in the middle, already just the photon travel and classical communication time to inform the nodes whether entanglement was generated combines to $t = L/c_{\mathrm{fiber}} = 250\,\mu\mathrm{s}$. This limits the maximum attempt rate to 4 kHz. Assuming unity collection efficiency of emitted photons, quantum frequency conversion to the telecom C-band with unity efficiency, fiber losses of $0.2\,\mathrm{dB\,km^{-1}}$ and perfect detector efficiency, the maximum achievable entanglement rate with the Barrett-Kok protocol is $r_{\mathrm{max}} = 200\,\mathrm{Hz}$.

Naturally, generating entanglement between distant nodes can be sped up by lifting the restriction of using just a single spin-photon interface per node. For a timebin size of 1 µs, up to 125 entanglement attempts „fit“ simultaneously into the channel between node and heralding station at any time. Adding the possibility to multiplex in frequency scales this number even further. Spatial multiplexing by using multiple fibers per connection (e.g. multicore fibers), even higher degrees of parallelization can be achieved. To exploit all of these degrees of freedom, a large number of spin-photon interfaces need to be accessible in parallel. This requires many drastic improvements on multiple levels, a few of which we want to discuss in the following.



#### PHOTONIC INTEGRATION

Accessing hundreds or thousands of spin-photon in a single node poses a significant challenge. The footprint of the devices (in our case nanophotonic diamond waveguides) is actually negligible, our current $4 \times 4\,\mathrm{mm}$ chip holds thousands waveguides. The challenge lays in addressing all devices optically and electrically. While this would be simply not possible in the same way as reported in Chapters 4 and 5 via positionable optical fibers, *photonic integrated chips* (PICs) provide a viable way to access large numbers of devices simultaneously. While diamond is a host to multiple promising spin-photon interfaces, its inert properties (chemically and optically) hinder the development of integrated photonic elements like phase shifters, optical switches, filters and beamsplitters. More advanced platforms like silicon nitride, aluminum nitride or lithium niobate offer to relieve this drawback by integrating diamond devices onto PICs from these materials[14]. First successful hybrid integration attempts already showed promising results of integrating more than 100 devices, including strain tuning capabilities to control the emission frequency of individual emitters[15]. Further improvements of the PICs by adding more capabilities like filtering, switching and more will be necessary to build deployable quantum network nodes based on diamond vacancy centers. As PICs are also being developed for a range of classical applications and can be fabricated in foundries, an essential step for maturing the technology also for quantum applications is already in progress.

#### NODE HARDWARE

Next to the actual quantum processor that will be the center piece of a quantum network node, a multitude of hardware components is required to control the quantum emit-

ters. The results in presented in Chapters 3 to 5 required a full laboratory of high-tech equipment including at least two PhD researchers to control up to two SnV centers at the same time. Extending this to hundreds or thousands of emitters must not scale linearly in terms of space, resources and (in)human labor. Each SnV needs to be controlled dynamically optically (one repump laser and one resonant laser[2]), electrically (e.g. strain tuning) and via radio-frequencies (qubit and memory control).

In particular, multiplexing emitters with the same frequency in time allows for multiplexing the corresponding lasers in the same way. A bigger challenge is posed by the radio-frequency equipment used to control the qubits. While waiting for the outcome of an entanglement attempt, the coherence of the involved qubits has to be preserved. This typically requires active measures like dynamical decoupling (DD) to extend the qubit coherence as the communication delay is much larger than $T_2^*$ of the SnV qubit. While the control hardware can be reused during the free evolution time $2\tau$ in the DD sequence, it requires sophisticated control to keep track of the qubit phase via local oscillators as well as routing to prevent cross-talk. Since the SnV qubit frequency depends both on the local magnetic field as well as strain, active control over the qubit frequency can help reduce cross-talk by spacing out the qubit frequencies of SnVs that are spatially grouped on the chip.

The SnV requires an operating temperature of around 1.5 K to prevent qubit decoherence via interaction with phonons. Cooling powers of cryostats in that temperature regime are limited to tens of mW currently with potential avenues for hundreds of mW. Still, even this improvement would give a cooling power budget of less than 1 mW per SnV for future large systems. As the qubit consists of an effective electron spin-$\frac{1}{2}$, significant AC-magnetic field strengths are require to coherently control the qubit state. While resistive losses can be reduced by using superconducting materials, dielectric losses are unavoidable at GHz frequencies. Proper thermal management will require efficient driving via resonant structures (posing engineering and experimental challenges to match the bandwidth of the structures with the qubit frequency across many devices) and/or thermal decoupling of the RF control train from the coldest stage of the cryostat, e.g. via a flip-chip design. While the cooling power of a few watt at the 4 K stage of commercial cryostats is significantly higher in current systems than at the coldest stage, this still requires careful thermal management when increasing the number of SnVs.



#### CONTROL SOFTWARE

Our current laboratory experiments are run in an software environment that has been developed with the help of dedicated software engineers, ensuring proper code quality and robustness, clear interfaces with layers of abstraction and version control. Without this level of control, it would not be possible to reproducibly conduct the experiments reported in this thesis, even less to build on top of them. Still, the control of a large quantum network node will require even more control, including time-efficient automated calibration routines and system checks as well as sophisticated scheduling logic and layers of abstraction to allow user-interfaces without understanding the exact operational

[2] This resonant laser might need to cover a large dynamic power range depending on the entanglement protocol to cover different operations like low-power readout and high-power single photon generation, so it might be split into multiple paths for pulse shaping and recombined afterwards.

structure of the node. A first demonstration of a quantum nodes operating system [16] addresses this need of multiplexed logic and scheduling. Further work on more efficient control of the hardware components as well as the experiment will be needed to change the nature of quantum network nodes from experimental setups to communication devices.

## 6.3. EPILOGUE

The research efforts leading to this thesis with the goal of building an efficient quantum network node show both the promising perspectives of the tin-vacancy center as well as the required engineering challenges to truly make this platform scalable. While near-term proof-of-concept experiments still will expand on the size and complexity of the experimental setup, more attention is and will be directed to decreasing these metrics. More capabilities will undergo miniaturization - from optical elements to RF control. Scaling a technology up actually means scaling its components down.

## REFERENCES


[1] J. M. Brevoord *et al.*, *Large-range tuning and stabilization of the optical transition of diamond tin-vacancy centers by in situ strain control,* Applied Physics Letters **126** (2025), 10.1063/5.0251211.

[2] C. M. Knaut *et al.*, *Entanglement of nanophotonic quantum memory nodes in a telecom network,* Nature **629**, 573 (2024).

[3] J. M. Brevoord *et al.*, *Quantum Frequency Conversion of Single Photons from a Tin-Vacancy Center in Diamond,* (2025), arXiv:2509.01661 [quant-ph] .

[4] I. Karapatzakis *et al.*, *Microwave Control of the Tin-Vacancy Spin Qubit in Diamond with a Superconducting Waveguide,* Physical Review X **14**, 031036 (2024).

[5] X. Guo *et al.*, *Microwave-Based Quantum Control and Coherence Protection of Tin-Vacancy Spin Qubits in a Strain-Tuned Diamond-Membrane Heterostructure,* Physical Review X **13**, 041037 (2023).

[6] B. Hensen *et al.*, *Loophole-free Bell inequality violation using electron spins separated by 1.3 kilometres,* Nature **526**, 682 (2015).

[7] J. Fischer *et al.*, *Spin-Photon Correlations from a Purcell-enhanced Diamond Nitrogen-Vacancy Center Coupled to an Open Microcavity,* (2025), arXiv:2506.20722 [quant-ph] .

[8] A. E. Rugar *et al.*, *Generation of Tin-Vacancy Centers in Diamond via Shallow Ion Implantation and Subsequent Diamond Overgrowth,* Nano Letters **20**, 1614 (2020).

[9] X. Guo *et al.*, *Tunable and Transferable Diamond Membranes for Integrated Quantum Technologies,* Nano Letters **21**, 10392 (2021).

[10] X. Guo *et al.*, *Direct-bonded diamond membranes for heterogeneous quantum and electronic technologies,* (2023), arXiv:2306.04408 [physics, physics:quant-ph] .

[11] P. C. Humphreys *et al.*, *Deterministic delivery of remote entanglement on a quantum network,* Nature **558**, 268 (2018).

[12] W. Pfaff *et al.*, *Unconditional quantum teleportation between distant solid-state quantum bits,* Science **345**, 532 (2014).

[13] N. Kalb *et al.*, *Entanglement distillation between solid-state quantum network nodes,* Science **356**, 928 (2017).

[14] A. W. Elshaari, W. Pernice, K. Srinivasan, O. Benson and V. Zwiller, *Hybrid integrated quantum photonic circuits,* Nature Photonics **14**, 285 (2020).

[15] N. H. Wan *et al.*, *Large-scale integration of artificial atoms in hybrid photonic circuits,* Nature **583**, 226 (2020).

[16] C. Delle Donne *et al.*, *An operating system for executing applications on quantum network nodes,* Nature **639**, 321 (2025).

# ACKNOWLEDGMENTS

Doing a PhD was not only a job, it was a long and exciting journey. There are many people that accompanied me these past years and to whom I want to show my appreciation and extend my heartfelt thanks.

**Ronald**, your guidance throughout these past years has been invaluable to me. You left me the space to grow and explore while providing support and nudges into the right directions. No matter whether it was work-related or personal topics, I always felt like I could come to you, discuss openly with you and leave the meeting feeling enlightened and motivated. Your way of leading not from a high supervising position, but deeply involved and close to your team is inspiring. Thanks for giving me the opportunity to work on such big and complex projects from ground up, I could not have imagined a PhD trajectory that suits me better. I wish you all the best for your joint academic and business future, I'm eager to see your coming milestones for the quantum network future. **Tim**, I enjoyed our closer collaboration on the DDRF differences between the NV and SnV. Thanks for your extensive feedback on my propositions, it improved them a lot!

**Stephanie Wehner, Andreas Reiserer, David Lucas, Francisco Machado** and **Toeno van der Sar**, thanks for taking the time and effort evaluating my thesis and being on my committee! **Andreas**, thank you also for giving the great Quantum Technologies lecture at TUM, that got me hooked onto quantum networks!

During my past four years, I was surrounded by many talented researchers and amazing people - I'm not talking about two different groups but actually friends and colleagues that combine these two attributes! First and foremost, I want to thank the two tall Penguins standing on my side today.

**Hans**, the other OG "Pingu"-guy, you were assigned as my "buddy" on my first day in the Hanson Lab, so you had to face the challenge of training a person without optics experiences in the lab and show me the ropes. You could have not done a better job. Your passion for physics and engineering, but also any other discussable topic spark a flame in any interaction with you. Thanks to your dedication to your proposition number 10, I learning from you was a bliss and your influence on the way I approach challenges in the lab (and in real life) cannot be understated. It happens more often than I'd like to admit, that I think in difficult situations: How would Hans tackle this? Building a lab together and getting more and more cool results over time was a truly awesome experience that I wouldn't wanna miss for anything. I'm glad to see that you, **Sophie** and **Hannah** enjoy life in Switzerland and I'm looking forward to visiting you there!

**Timo**, you joined the "Pingu"-family as a Master student in a time, when we completely had to rebuild the setup and started with a very ambitious project. I still remember when I talked to Hans after our first meeting and just told him with a smile:

"That guy's gonna do great!". Despite our high expectations, it was still impressive to see how incredibly well you found your place on a big project among two experienced PhDs and you managed to surprise us with your skills and wit at least once per week. I sincerely enjoyed working with you, you bring a cheerful and warming attitude to the lab (even when you usually doubt every word that comes out of my mouth). I'm immensely happy (and proud) that you decided to continue your PhD in the Pingu-family, thanks for pushing these past months along-side me like a maniac! I am excited to see what you will achieve in the next years.

**Alex**, you complete the Pingu-family. The audacity to join us after scooping our MW project... - I'm very glad you did! You bring calmness to the team, and your dedication from deriving theoretical models to aligning painful optical setups is inspiring. I still cannot fathom what drives you for these crazy bike races (until you sent me the tracking link for the first one you told me about, I really thought you are messing with me), and I'm glad that we could spend time together enjoying other pleasures of life like some beers and good food. Good luck with the TSW-project, and on your next biking adventures, maybe one route passes through Munich!

**Matteo**, you set the foundation for the tin project, but most importantly for me, you were a huge part of my social life here. Jamming together was a lot of fun, and your unbelievable musical skills are matched by your cooking skills. The Via Ferrata and Sailing trip with **Hans** and **Will** are two of my core memories here, thanks for pushing us through the mountains (despite not thinking we could do it!). I'm glad you are enjoying life in Barcelona and am excited to see what will come next! **Nina**, your expertise in the cleanroom is unmatched. It was always impressive to see the evolution from a bare diamond to these elegant devices. In the dark times of burnt diamonds, I'm grateful for the collaboration we had in getting the process back under control, which ultimately lead to us designing and you creating the precious FBF15! Thanks for all the great times with dinners, drinks, and supplying me with medicine when I was stuck at home with Covid. **Lorenzo**, you were the most "all-rounder" Postdoc I've ever seen. You helped on every project and setup, and I really enjoyed the serious, but still mischievous vibe you brought into the lab. **Julia**, it was great to see you tackle many different projects, thanks for teaming up on the challenge of navigating the procurement jungle for a new fridge with me. **Tim**, you're relaxed character is soothing in stressful times, it's always nice to have a quick chat with you. I was stocked for you when you finally saw cavity-coupled tins, and I'm excited to see what you'll be able to do with them in Pingu's brother Macaroni **Dani**, the same holds for you, and thanks for always bringing a fun vibe to the group and for writing a song for me! **Niv**, joining an experimental group as a theorist is quite a big step, and transitioning to the lab yourself an even bigger one! Good luck with this new side of the PhD. **Leo**, the CEO of the cleanroom, you're dedication to Team Diamond is unmatched. I'm a fan of your sample designs (and their names!). All the best to bringing them from design to real life. **Marta**, it was nice having you around for the past few months, good luck with your next steps. **Slava**, while our joint tin-meetings came to an end early in my PhD, I thoroughly appreciate the input you provided on many physics questions I had and the dicussions in your office!
**Julius**, the directness and simplicity with which you tackle any challenge - whether at

work or sports - is unmatched. Whether it's playing volleyball indoors, on the sand or just going out together, you make every occasion more fun and bring an energy to it that is captivating. I always enjoyed discussing lab issues with you as you managed to make them sound smaller than they were in my head. I'm glad that we had to ride our bikes to Kratos quite far and had a lot of time to chat always, something I'll miss about leaving Delft. **Yanik**, you're the best office- and lab-mate one could with for, you're representing German organization to the highest degree. Thanks for fun time in Switzerland, Milano (I still believe our sticker survided) and for introducing me to the best German-Italo Schlagerband I ever listened to. Also a big thanks for the countless Friday evenings with **MG**, **Julius** and many others, I hold those dearly. **Matteo Sr.**, our overlap was very short, but you're presence is still felt throughout the lab infrastructure and code. It was nice meeting you and **Grace** occasionally throughout the world, I hope this keeps on happening. **Sophie**, it is astonishing to think about that we still shared an office during your PhD and now you are already back here as a PI. Good luck with building your group and growing your family. **Arian**, you've been the fountain of wisdom throughout my whole PhD, thanks for always knowing the most random piece of technics or physics that solved the issues at hand. I always enjoyed the discussions at lunches or dinners with you, good luck to you and **Vincy** in Singapore. **Kian**, watching you present was always a bliss, and it's great to hear that Canada is treating you well. **Marie-Christine**, thanks for your relentless positivity! You're brilliant as scientist and as a person, it was great meeting up with you and **Josh** in Vienna again. All the best for you and your growing family. **Alejandro**, thanks for always making any event or conversation memorbale with your wit and boldness, good luck at HSBC. **Christian**, being basically your own team within a research group is a huge challenge, and it's impressive to see how you pull it off. Thanks to **Chantal**, **Esther** and **Sara** for always solving all our non-physics related challenges super quickly and efficiently, and thanks **Rebecca** for getting big companies to work with us on our terms!
Throughout my PhD, I saw many students come and go, thanks to all of you for always providing a nice fresh wind to the group and congrats to your degrees! **Zarije**, you managing to get the first PL on Pingu marked basically its birthday, thanks for achieving this with us. It was always a pleasure working in the lab and chatting with you in my own dialect too, and getting surprised by the one or other unknown Austrian expression. Thanks for joining us in the band with the violin for a gig, and I'm thrilled to hear you sing there now as well! Good luck with your PhD. **Stijn**, whenever I have to touch the splicer now, I don't feel worthy. Thanks for whispering to our fibers, and good luck in Eindhoven. **Noé**, your curiosity and software-skills were a pleasure to have in the lab and I wish you all the best for your future combining software and quantum. **Colin**, you are a pleasure to have around, always lightening the mood. It's impressive how you combine your research and political activity.
My project was part of a big collaboration with Fujitsu. I would like to thank **Sato-san** and **Kawaguchi-san** and their team for the nice exchanges about our projects and for hosting me and Mariagrazia at your facility in Tokyo, it was a great experience. Arigato gozaimasu!

Team Diamond would not be Team Diamond, if it wasn't for the TimTams. **Nic**,

jamming and chatting with you has always been a great way to get my mind off work, I really enjoyed our long conversations about life at Matteo's or Klooster's. Good luck with wrapping up your thesis. **Conor**, you're defense was the first one I attended and I remember being in awe with how brilliant you performed. It's been great to have you back around and I wish you much success with Delft Networks! **Sjoerd**, I will miss batteling it out at the Diamond Cup with you! You're a great sportsman and you're ambition and enthusiasm in the lab is matching that. All the best for your future. **Laurens**, it's been fun shooting for TUDelftTV together. I'm confident that you'll be able to inspire many people with your way of communicating! **Gerben**, good luck building your own zoo of devices. **Tobi**, thanks for showing MG and me around Tokyo's nightlife, I'll never forget the awesome bar you brought us to! All the best to you, **Laurens**, **Gerben** and **Jasper** with the SiC project! **Kilian**, it's been great to have you around on Friday evenings a lot lately, good luck with your next chapters! **Margriet**, the number-one address when it comes to understanding infidelities and GST. I enjoy how you combine directness with openness in conversations! It's been great to share an office with you and **Christina**. **Christina**, you're kindness is inspiring, and thanks for hosting one of the rare "German"-evenings! It's impressive to see what you get out of all these nuclear spins together with **Madhu** and **Dan**. **Ben**, thanks for the very valuable discussions on DDRF and good luck with the last bits of the PhD! **Hans**, also to you thanks for making me understand DD control, and the weekly Sunday meetings at AH XL! **Jiwon**, whenever we talked and you told me that you're sticking around longer, I felt relieved as having you and your enthusiasm in Team Diamond is very enjoyable. Good luck with your next steps. **Kai**, thanks for the nice volleyball sessions! **Guido**, thanks for always bringing an intriguing twist to any conversation, good luck in Stanford. **Anta**, you're genuine positivity is refreshing, enjoy life in Barcelona.

I'm excited to see what the future holds for the new extension to Team Diamond in form of the **Carlos** Lab. **Carlos**, thanks for the many lunch conversations and for the discussions on life and work at BQIT. I'm excited to see what you will achieve in the next years. **Jan**, Carlos couldn't be luckier to have such a dedicated and hands-on first PhD student. It was great having you around for the past year(s), all the best for the rest of your PhD. **Lin**, your enthusiasm is great, I enjoyed the many chats we had! **Elena** and **Matteo**, good luck with your PhDs!

I also want to thank the Uitje committee of 2022, **Figen, Liza, Mariagrazia, Maxim** and **Siddharth** for the fun times planning and managing the Uitje, I'm very proud of what we achieved as a team!

One of the great things about QuTech is the amount of supports on various fields of expertise you can get! Our software engineers **Pieter**, **Henri**, **Ravi** and **Peter**, thanks for managing and improving the code base on a daily basis and helping me with any issues that come up. **Pieter**, your skills in coding combined with your impressive understanding of quantum experiments is inspiring, thanks for introducing me to the world of FPGAs. **Henri**, the chief of DiamondOS (or diamandos?), thanks for all the hours of hands-on implementing drivers and debugging together in the lab, I always

enjoyed the atmosphere you brought in. **Ravi**, you're a powerhouse both in coding and in sports, thanks for always having a cheerful attitude!

Building a lab, I ran into many, many hardware challenges, where I was glad to have support from a bunch of talented engineers and technicians. **Raymond**, **Raymond**, **Berend** and **Roy**, whenever I stepped into your office, I immediately had an open ear to my challenges, no matter how mandane they might have seemed for you. And everytime I left, I felt like I learned something and know now 3 solutions for my issue. Thanks a lot for this! **Olaf**, **Jason**, **Tom** and **Erik**, thanks for all your help regarding cryostats, copper, heating, pumps, 3D printers and more. **Olaf**, special thanks for lending us your nose when we thought our setup smelling funny! **Roy**, **Siebe**, **Vinod** and **Jelle**, whatever task was at hand, no matter how short-noticed it popped up, you were always there to help. Thanks for not only solving issues that we found, but also your pro-activeness in improving our labs. **Nico** and **Tim**, thanks for machining all the inner parts of Pingu, and for providing so many quick-fixes and improvements to whatever caused me headaches. **Hitham** and **Regis**, thanks for your great approach of making the labs safe together rather than just pushing policies onto the labs, I enjoyed collaborating with you! **Yannick** and the DEMO team, thanks for adapting our PCBs throughout the years and being super helpful in all regards. And thanks for taking the burden of connectorizing two more of these massive Fischer-connectors for us with a laugh!

During the majority of my time at QuTech, I was part of the amazing Q2! Thanks to all fellow musicians who made the workplace also a fun-place outside workhours: **Anne-Marije, Bart, Conor, Desa, Floor, Gustavo, Hanifa, Hans, Julia, Laurens, Maja, Matteo, Matteo, Nic, Pablo, Sander, Timon, Tzula** and **Will**.

Thanks to all the people around QuTech who always were up for a chat in the hallway or some fun at the social activities: **Brennan, Davide, Fenglei, GJ, Hanifa, Irene, Liza, Maxim, Mohammed, Nico, Pablo, Sasha, Scarlett, Shannon, Slava, Stephan** and **Vicky**.

I'm grateful for the friends that I made throughout my time in Delft. **Will**, our overlap was only a few months, but you made me feel home in Delft with the nice cooking and gaming evenings, jam sessions and bar visits. I was stocked to witness you and **Kaja** getting married, all the best for your future! **Gustavo**, you're not only the backbone of the band, but also an awesome person and I always enjoyed hanging out with you a lot. **Adrian**, we met when playing volleyball and I immediately could tell that you were a great guy. Thanks for all the beach volleyball sessions, the occasional drinks and drifting off into the world of gaming, architecture and music.

Ik maakte ook deel uit van het herenteam 7 bij Kratos met **Alexander, Amin, Bram, Cas, Ioannis, Joost, Julius, Maarten, Martijn, Michiel, Tristan** en **Xin**. Jullie waren mijn constante dosis Nederlands (in taal en cultuur) en ik heb vanaf de eerste training genoten van de sfeer in het team. Bedankt dat jullie me hebben overgehaald om met jullie wedstrijden te spelen! Ook een grote dank aan onze trainers **Jens, Leandra, Myrthe** en **Vera**. Aruba!

Apart from playing in a team, I also played some fun games of indoor and beachvolleyball, thanks to all the great people form VolleyBolley, in particular **Adrian, Amin Camila, Camila, Girish, Jip, Kiran** and **Stefano**.

Volleyball ist wirklich ein großer Teil meines Lebens, mein 3. Volleyball-Shoutout geht an BeachBang2, mein Heimatteam mit **Alex, Felix, Hendrik, Katja, Laura, Matthias, Simon** and **Steffi**. Ich freue mich darauf, wieder öfter mit euch zu spielen!

Einige Freunde aus der Heimat haben mich aus der Ferne durch die letzten Jahre begleitet, vielen Dank an **Chrissi, Dennis, Felix, Luca, Ralf, Susi** und **Viki**. Ihr wart mir immer eine mentale Stütze und ich freue mich jedes Mal, wenn ich die Möglichkeit habe mit euch in alten Zeiten zu schwelgen.

Ich freue mich wahnsinnig darauf, meine Münchnern wieder mehr zu sehen und nicht nur immer neidisch die tollen Aktivitäten in den Chatgruppen mitzuerleben. Danke, dass ihr das Studium, aber auch die letzten Jahre mit eurer Freundschaft so bereichert habt: **Andre, Caspar, Flo, Hanni, Laura, Michi, Passi, Simon, Steffi, Vasco** und **Vroni**. Zwei weitere tolle Menschen, die ich gedanklich auch immer München zuordne: **Daniel**, sowohl die Zeit am WMI, als auch die Lockdown Skypetelefonate und kürzlich das Treffen in Kopenhagen sind mir immer eine Freude gewesen. **Sophie**, eine Freundschaft in kurzer Zeit in Kanada geformt, die seither große Distanzen überdauert, ist etwas sehr besonderes, und ich bin wahnsinn froh darüber und stolz darauf. Es war toll, deiner Hochzeit mit **Conny** beizuwohnen und ich wünsche euch viel Erfolg mit dem Hausbau und eurer Zukunft!

Klein, aber fein: So würde ich meine Familie beschreiben. **Mama** und **Papa**, es gibt kein Attribut vor dem Wort "Dank", dass meine Gefühle für eure Unterstützung und Hingabe genügend beschreibet. Ihr habt mir alles ermöglicht, von meiner Kindheit an bis tief ins Studium, und habt mich die Person werden lassen, die ich jetzt bin. Ich könnte mir keine besseren Eltern vorstellen, danke für Alles.

Finally, my deepest thank you to **Mariagrazia**, my biggest believer and the color in my life. With you, everything seems possible, you help me see things more clearly than I could on my own. Maybe it was destiny that we met, maybe it was chance, but I'll always be grateful we got to go through this chapter side by side. I always say that I never regretted coming to Delft for a single second, and the reason for this is you. I'm so excited for our future together. Ti amo.

# LIST OF PUBLICATIONS

5. Method for Annealing a Diamond Substrate that comprises a Color Centre
   N. Codreanu, R. Hanson, **C. Waas**; *Patent ID WO2025230422A1 (2025)*

4. Large-Range Tuning and Stabilization of the Optical Transition of Diamond Tin-Vacancy Centers by In-Situ Strain Control
   J. M. Brevoord, L. G. C. Wienhoven, N. Codreanu, T. Ishiguro, E. van Leeuwen, M. Iuliano, L. De Santis, **C. Waas**, H. K. C. Beukers, T. Turan, C. Errando-Herranz, K. Kawaguchi, R. Hanson; *Appl. Phys. Lett.* 126, 174001 (2025)

3. Control of Solid-State Nuclear Spin Qubits Using an Electron Spin-1/2
   H. K. C. Beukers*, **C. Waas***, M. Pasini, H. B. van Ommen, Z. Ademi, M. Iuliano, N. Codreanu, J. M. Brevoord, T. Turan, T. H. Taminiau, and R. Hanson; *Physical Review X*, 15, 021011, 2025

2. Nonlinear Quantum Photonics with a Tin-Vacancy Center Coupled to a One-Dimensional Diamond Waveguide
   M. Pasini, N. Codreanu, T. Turan, A. Riera Moral, C. F. Primavera, L. De Santis, H. K. C. Beukers, J. M. Brevoord, **C. Waas**, J. Borregaard, and R. Hanson; *Physical Review Letters*, 133, 023603, 2024

1. Heralded initialization of charge state and optical-transition frequency of diamond tin-vacancy centers
   J. M. Brevoord*, L. De Santis*, T. Yamamoto, M. Pasini, N. Codreanu, T. Turan, H. K. C. Beukers, **C. Waas**, and R. Hanson; *Physical Review Applied*, 21, 054047, 2024

*Equally contributing authors

# CURRICULUM VITEA

**Christopher WAAS**
July 8th, 1997, Landau a.d. Isar, Germany

| | |
|---|---|
| 2021 - 2026 | PhD in Physics<br>Delft University of Technology, Delft, The Netherlands<br>Thesis: *"The Tin-Vacancy Center in Diamond as a Quantum Network Node"*<br>Promotor: Prof. Ronald Hanson<br>Copromotor: Dr. Tim H. Taminiau |
| 2018 - 2021 | Master of Science in Physics, *with high distinction*<br>Technical University of Munich, Munich, Germany<br>Thesis: *"Development of Scalable On-Chip Circuit Quantum Acousto-dynamics"*<br>Supervisor: Prof. Dr. Hans Hübl |
| 2015 - 2018 | Bachelor of Science in Physics, *with high distinction*<br>Technical University of Munich, Munich, Germany<br>Thesis: *"Set-up and Analysis of a Two-Dimensional Translation Stage for Integrated Optics Experiments"*<br>Supervisor: Prof. Dr. Menno Poot |
| 2007 - 2015 | Secondary school<br>Gymnasium Landau a.d. Isar, Landau a.d. Isar, Germany |

ISBN: 978-94-6518-253-7